Tomographie à partir de corrélations de bruit de fond sismique

L. Stehly

UNIVERSITE JOSEPH FOURIER - GRENOBLE I

OBSERVATOIRE DES SCIENCES DE L'UNIVERS DE GRENOBLE

LABORATOIRE DE GEOPHYSIQUE INTERNE ET TECTONOPHYSIQUE

THÈSE

Tomographie à partir de corrélations de bruit de fond sismique

présentée par

Laurent Stehly

pour obtenir le titre de Docteur de

L'UNIVERSITÉ JOSEPH FOURIER - GRENOBLE I

Spécialité : **Sciences de la Terre, de l'Univers et de l'Environnement**

Composition du Jury :

Jean Paul Montagner	Pr. à l'IPG Paris	Rapporteur
Domenico Giardini	Pr. à l'ETH Zürich	Rapporteur
Luis Rivera	Pr. à l'EOST Strasbourg	Examinateur
Anne Paul	Dir. de Rech. au LGIT Grenoble	Examinateur
Nikolai Shapiro	Dir. de Rech. à l'IPG Paris	Examinateur
Yves Colin de Verdière	Pr. à institut Fourier de Grenoble	Invité
Jocelyn Guilbert	Ingénieur-Chercheur LDG-CEA, Paris	Co-directeur de thèse
Michel Campillo	Pr. Univ. Joseph Fourier, LGIT	Directeur de thèse

Date de soutenance : le 5 novembre 2007

Table des matières

Table des figures

Liste des tableaux

Chapitre 1

Introduction

Sommaire

Imager la terre à l'aide d'enregistrements de séismes

L'un des objectifs de la sismologie et plus généralement de la géophysique est de déterminer la structure de la terre avec le plus de précision possible. En donnant une image détaillée de la structure actuelle de la terre, la géophysique est complémentaire de la géochimie et de la géologie qui étudient des processus intégrés dans le temps permettant de retracer l'histoire de la terre, mais avec une résolution spatiale limitée. La sismologie permet de connaître la vitesse des ondes P et S au sein de la terre. Celle-ci dépend des paramètres élastiques et de la densité, qui eux-mêmes sont fonction de la minéralogie et des conditions thermodynamiques (pression, température).

Une première étape a été de déterminer la structure radiale moyenne de la terre. Cela a été permis par l'observation des temps d'arrivée d'ondes générées par des séismes de forte magnitude et réfléchies au sein de la terre, en fonction de la distance épicentrale (figure 1.1). Ces études ont montré qu'au premier ordre les variations latérales de vitesse des ondes P et S au sein de la terre étaient faibles devant les variations de la vitesse en fonction de la profondeur. Il est donc légitime d'approximer la terre par un modèle radial composé de différentes couches concentriques : croûte terrestre, manteau supérieur puis inférieur, noyau externe et interne. Le modèle de ce type le plus connu est le modèle PREM (*Dziewonski and Anderson* (1981)) présenté sur la figure 1.2.

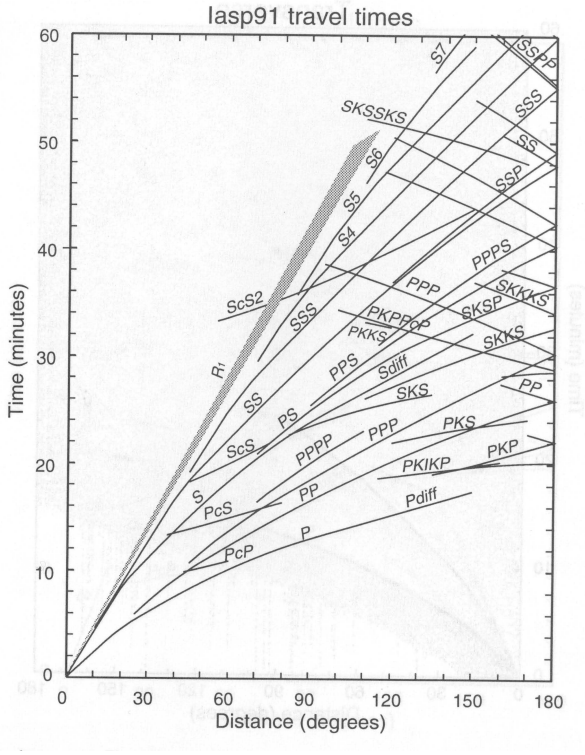

FIG. 1.1: Temps d'arrivée moyens de différents types d'ondes en fonction de la distance épicentrale

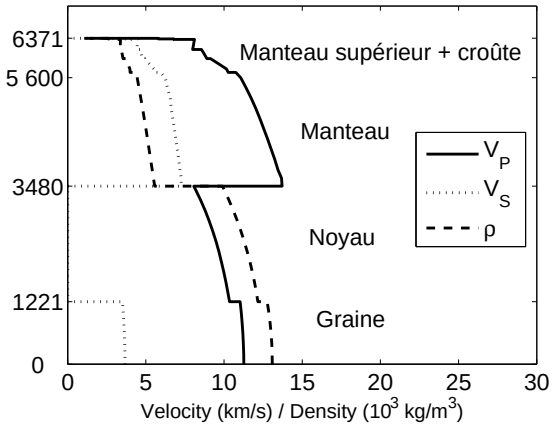

FIG. 1.2: Modèle radial de terre PREM (Preliminary Earth Model, par *Dziewonski and Anderson* (1981)), présentant les vitesses de propagation des ondes P et S ainsi que la densité en fonction de la profondeur.

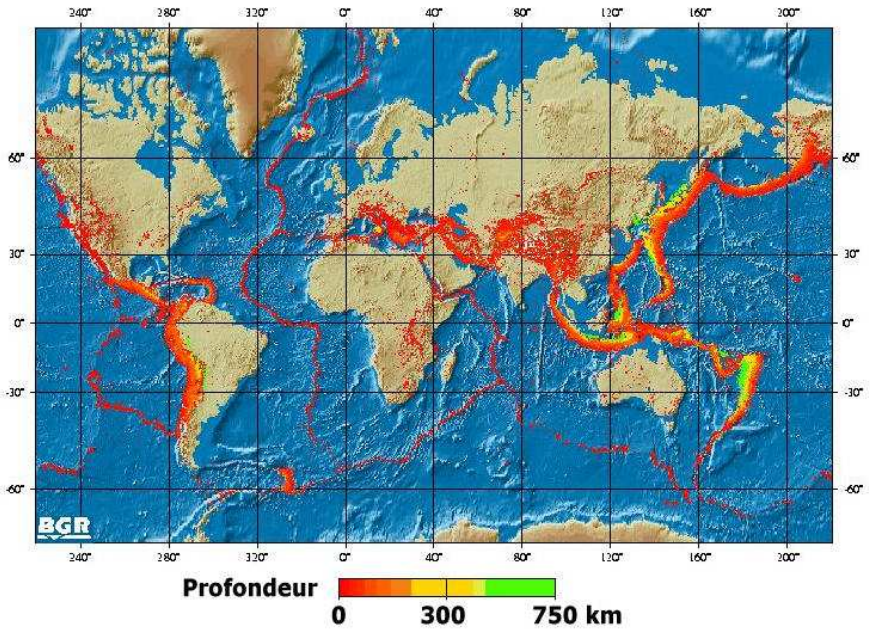

FIG. 1.3: Sismicité mondiale cumulée pendant 10 ans.

La connaissance du modèle moyen de la terre, bien qu'importante, n'est toutefois pas suffisante pour avoir une compréhension profonde de la dynamique terrestre. Pour aller plus loin il est nécessaire d'obtenir une véritable image 3D du globe qui seule peut révéler toute la complexité de la croûte terrestre, la géométrie de la lithosphère ou encore mettre en évidence des phénomènes liés à la convection mantellique tels que les points chauds.

Les méthodes employées pour déterminer la structure sismique de la terre reposent sur un principe simple : il s'agit de mesurer la vitesse de propagation des ondes sismiques entre un grand nombre de séismes et de stations, et de chercher ensuite un modèle de terre permettant d'expliquer au mieux l'ensemble de ces mesures. La résolution du modèle ainsi obtenu dépend directement du nombre de trajets pour lesquels on a pu mesurer des vitesses de propagation et donc du nombre de séismes enregistrés. De là découlent les principales limitations de ces méthodes : de larges zones sur terre sont asismiques (figure 1.3) et faute de sources d'ondes nous ne pouvons les étudier avec une bonne résolution. Dans les régions sismogènes, les tremblements de terre tendent à provenir toujours des mêmes zones de failles, ce qui limite la diversité des trajets. L'absorption rapide des ondes de surface de période inférieure à 20 s, rend difficile l'étude détaillée de la croûte terrestre. La faible occurrence des séismes, quant à elle, interdit l'étude des déformations induites par la tectonique au voisinage des failles ou encore au sein d'un édifice volcanique.

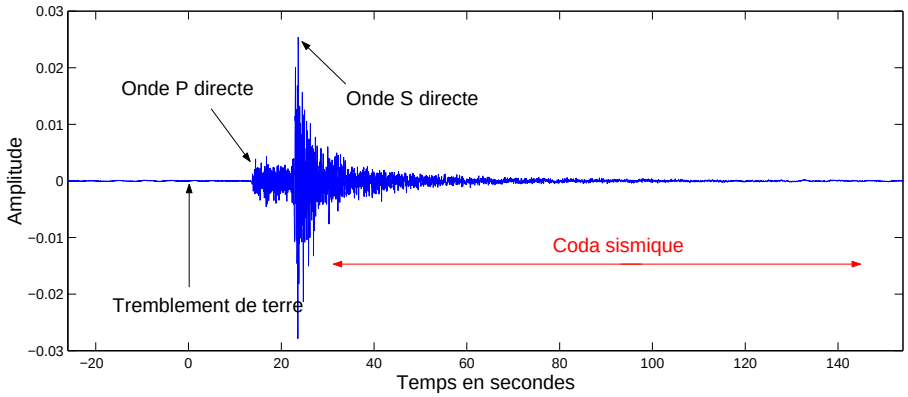

FIG. 1.4: Enregistrement d'un séisme situé à 90 km de la station, filtré entre 1 et 10 Hz. On distingue tout d'abord les ondes P, suivies des ondes S. La coda est constituée des dernières arrivées et présente une longue décroissance exponentielle.

Afin d'aller au-delà de ces limitations, nous souhaitons voir dans quelle mesure il est possible de faire de la tomographie en se servant uniquement du bruit de fond sismique. L'avantage du bruit par rapport aux séismes, est qu'il est disponible partout et à tout moment. Ainsi, on espère pouvoir étudier la croûte terrestre avec une meilleure résolution spatiale, et être capable de détecter d'éventuels changements se produisant au sein du milieu de propagation.

Des ondes directes aux champs diffus

Étudier la terre à l'aide de bruit de fond sismique plutôt qu'avec des enregistrements de séismes représente un changement conceptuel important. Lorsque l'on étudie la propagation d'ondes générées par des tremblements de terre, on suppose que celles-ci ont une trajectoire déterministe qu'il est possible d'écrire explicitement. Cette approche est pertinente pour des milieux simples, tel que des milieux homogènes, ou stratifiés horizontalement. Elle n'est toutefois pas suffisante dans le cas d'un milieu diffusant et ne peut rendre compte de toute la complexité d'un sismogramme : elle permet d'expliquer l'arrivée des ondes P, S et des ondes surface, mais pas les arrivées tardives constituant la coda sismique (figure 1.4).

En effet, la coda résulte de la diffusion des ondes par les hétérogénéités présentes au sein de la croûte terrestre (*Aki and Chouet* (1975); *Aki and Richards* (1980); *Sato and Fehler* (1998)). Cette diffusion multiple implique une grande complexité, si bien que le champ d'ondes ne peut être écrit explicitement. Il est difficile de modéliser la forme d'onde de la coda connaissant le milieu (problème direct) et impossible de déterminer le milieu à l'aide des ondes de la coda qui le traversent (problème inverse).

C'est paradoxalement cette complexité qui permet d'aboutir à des propriétés simples :

la coda tardive ayant été diffusée un grand nombre de fois peut être vue comme un champ aléatoire, constitué d'ondes se propageant dans toutes les directions avec une phase quelconque. Un tel champ d'ondes excite tous les modes propres du milieu, on parle alors d'équipartition. Ce phénomène a été mis en évidence pour la coda par *Hennino et al.* (2001). Une fois l'équipartition établie, on peut démontrer que la corrélation du champ d'ondes enregistré en deux points est la fonction de Green[1] complète du milieu comprenant tous les modes de propagation. Cette idée a été mise en pratique par *Campillo and Paul* (2003), qui en corrélant des enregistrements de coda issus de 101 séismes ont pu reconstruire la fonction de Green entre plusieurs couples de stations séparées par des distances de l'ordre d'une centaine de kilomètres.

Est-il possible de faire de même avec le bruit de fond sismique ? L'idée sous-jacente est que la nature aléatoire des sources de bruit va jouer le même rôle que la diffusion pour la coda. En effet si les sources de bruit sont réparties de façon homogène sur la terre avec une densité suffisante, elles vont également générer un champ d'ondes diffus, où tous les modes seront excités avec un même niveau d'énergie. Ainsi en corrélant des enregistrements de bruit on doit pouvoir retrouver la fonction de Green et donc connaître la vitesse de propagation des ondes entre n'importe quel points de la surface. Par la suite ces données pourront être inversées pour déterminer un modèle de terre.

La pierre angulaire de cette approche est le caractère aléatoire du bruit de fond sismique. En réalité le bruit sismique en dessous de 1 Hz est essentiellement constitué d'ondes de surface (*Friedrich et al.* (1998); *Ekström* (2001)) générées par les océans. On ne s'attend donc pas à ce qu'il soit complètement isotrope et homogène comme on l'aurait souhaité, certains azimuts (orientés vers la côte) risquant d'être privilégiés par rapport à d'autres.

Plan du manuscrit

La directivité du bruit sismique pose d'emblée la question suivante qui constitue la trame du présent manuscrit : le bruit de fond sismique peut-il être utilisé pour faire de la tomographie ? Autrement dit, est-il possible de reconstruire la fonction de Green entre deux points de la terre, en corrélant simplement le bruit de fond qu'on y enregistre, ou au contraire, la répartition inhomogène des sources de bruit rend elle cette approche impossible ?

Afin de répondre à ces questions, nous commençons par étudier sous quelles conditions les corrélations de bruit convergent vers la fonction de Green du milieu. Dans le chapitre 2, nous évoquons brièvement l'historique des corrélations et présentons des

[1]La fonction de Green entre deux points A et B, est l'enregistrement qu'on obtiendrait en B si une source impulsionelle (un Dirac) était placé en A. Ainsi, connaître la fonction de Green du milieu revient à connaître la vitesse des diverses ondes pouvant se propager entre A et B.

approches théoriques simples. Dans les chapitres 3 et 4, nous présentons les travaux de *Colin de Verdière* (2006a) qui permettent d'établir le lien entre corrélation et fonction de Green dans un contexte très général dépassant le cadre de la sismologie.

La seconde étape (chapitre 5) est de voir si le bruit de fond respecte ou non les exigences de la théorie. Nous étudions ainsi l'origine du bruit de fond entre 5 et 40 s de période, à l'aide de réseaux situés en divers points du globe (Californie, côte Est des USA, Europe et Tanzanie). Nous montrons que le bruit entre 5 et 10 s étant généré localement le long des côtes est fortement directif. Au contraire, au delà de 10 s de période, le bruit est global et provient de l'hémisphère nord en hiver, et de l'hémisphère Sud en été. Moyenné sur un an, il n'est pas à complètement isotrope, mais sa directivité est faible.

Ceci pose la question de la qualité des fonctions de Green obtenues à partir des corrélations. Le chapitre 6 est consacré à ce problème. En analysant 11 ans de données continues, nous montrons que les corrélations sont stables au cours du temps, et qu'elles permettent des mesures de vitesse suffisamment précises pour détecter et corriger des erreurs d'horloge interne de stations de l'ordre du dixième de seconde. Cette précision est suffisante pour faire de la tomographie à partir de corrélations.

Nous présentons donc au chapitre 7 des cartes de vitesse de groupe des ondes de Rayleigh entre 5 et 20 s de période de la Californie du Sud, obtenues en corrélant un mois d'enregistrements sur 62 stations. Suite à cette première étude, dans le chapitre 8, nous appliquons cette méthode à l'Europe de l'Ouest, en nous focalisant plus particulièrement sur les Alpes. Cette étude se veut plus ambitieuse que la précédente, nous y exploitons un an d'enregistrement à 150 stations. Disposant de stations 3 composantes, nous présentons des cartes de vitesse de groupe des ondes de Rayleigh et de Love, entre 5 et 80 s de période. Les courbes de dispersion extraites de ces cartes sont ensuite inversées pour retrouver, en chaque point du modèle, la vitesse des ondes S en fonction de la profondeur. Ceci nous permet de présenter un modèle du Moho sous les Alpes.

Cette étude a mis en évidence que la directivité du bruit de fond rendait difficile la reconstruction de la fonction de Green pour certains azimuts. Dans le chapitre 9, nous montrons que la coda de la fonction de Green est reconstruite par les corrélations de bruit. Elle peut être mise à profit pour mesurer des vitesses sur des trajets où les corrélations de bruit ont échoué.

Première partie

Théorie

Chapitre 2

Introduction aux corrélations de bruit de fond

Sommaire

2.1 Aperçu historique

La fonction de Green d'un milieu entre deux points A et B est l'enregistrement que l'on obtiendrait en A si une source impulsive (un Dirac) était placée en B. Connaître la fonction de Green entre deux points revient à connaître, à chaque fréquence, la vitesse et l'atténuation des différentes ondes se propageant de A à B, ce qui nous renseigne sur les caractéristiques du milieu.

Dans de nombreux domaines il est intéressant de pouvoir mesurer les caractéristiques d'un milieu (la fonction de Green), sans utiliser de source pour l'éclairer, mais en se servant uniquement d'ondes générées par le bruit ambiant. On parle alors d'imagerie passive. Par "bruit ambiant" nous entendons toutes les fluctuations aléatoires d'un milieu se produisant sans qu'on y mette volontairement une source. En sismologie, il s'agit de toutes les ondes générées par les activités humaines, les ondes océaniques, la pluie... en acoustique à très haute fréquence il pourrait s'agir de l'agitation thermique.

L'imagerie passive laisse entrevoir des applications aussi bien en sismologie (imagerie de la croûte terrestre dans des régions asismiques), qu'en acoustique (contrôle non destructif de structures) ou encore en acoustique sous-marine. Ceci explique que des travaux sur les corrélations de bruit ont été menés par des équipes s'intéressant à des applications variées menant à une grande diversité d'approches tant théoriques qu'expérimentales.

D'un point de vue historique, c'est en héliosismologie que les corrélations de bruit ont été utilisées pour la première fois. En corrélant l'intensité des fluctuations aléatoires de la position de la surface du soleil, *Duvall et al.* (1993) ont pu mesurer le temps de propagation des ondes P en fonction de la distance. Cette méthode a permis par la suite d'étudier l'écoulement de matière en surface entre l'équateur et les pôles du soleil (*Gilles et al.* (1997)).

Weaver and Lobkis (2001) ont montré que l'auto corrélation de bruit thermique enregistré à la surface d'un bloc d'aluminium correspondait à la fonction de Green entre ce point et lui même. Un résultat similaire est obtenu en corrélant les champs enregistrés par deux récepteurs distincts, le bruit étant généré par une unique source située au sein d'une cavité réverbérante (*Lobkis and Weaver* (2001a)) ce qui permet d'obtenir un champ d'ondes aléatoire à partir d'une source unique.

Suite à ces résultats expérimentaux, différentes approches théoriques ont été développées, formalisant le lien entre corrélation de bruit et fonction de Green. Elles diffèrent les unes des autres par les concepts employés, leurs domaines de validité (milieu ouvert ou fermé, homogène ou non, avec ou sans atténuation...), et leurs descriptions du bruit (sources aléatoires, sources ayant une distribution connue, source unique dans un milieu diffusant...).

Weaver and Lobkis (2001) suppose que le bruit est tel qu'il excite tous les modes propres du milieu avec un même niveau d'énergie, et une phase aléatoire (on parle alors d'équipartition des modes). Ces hypothèses impliquent directement que la corrélation du bruit entre deux points est la fonction de Green du milieu entre ces deux mêmes points. Cette démonstration suppose un milieu sans atténuation, avec une distribution discrète de modes (milieu fermé). Elle n'est donc pas transposable au cas d'un milieu ouvert ayant une distribution continue de modes, ni à un milieu absorbant.

Derode et al. (2003a,b) interprètent la reconstruction de la fonction de Green en se servant d'une analogie entre corrélation et expérience de retournement temporel. Cette approche permet d'étudier spécifiquement le cas d'un milieu ouvert. Ils montrent ainsi que si des sources entourent continûment deux récepteurs A et B, alors la corrélation des enregistrements en A et B correspond à la fonction de Green entre ces deux points. Le résultat est toujours valable si la distribution de sources est imparfaite, dans la mesure où le milieu est hétérogène. Les hétérogénéités du milieu, en diffusant les ondes, agissent alors comme des sources de bruit secondaires. Il est noter qu'en

sismologie *Larmat et al.* (2006) ont étudié la rupture du fameux séisme de Sumatra du 26 décembre 2004 en se servant du retournement temporel. *Snieder* (2004); *Roux et al.* (2005b) explique la reconstruction de la fonction de Green par les corrélations en se servant du théorème de la phase stationnaire : seule les sources alignées avec les stations contribuent à la corrélation, les autres sources interférant de façon destructives. *Wapenaar* (2004) utilise le théorème de réciprocité pour étudier (entre autre) le cas d'un milieu ayant une surface libre. *Weaver and Lobkis* (2001, 2003); *van Tiggelen* (2003); *Godin* (2007) quant à eux invoquent le théorème de fluctuation dissipation. Le cas particulier de milieux non réciproques où la propagation entre A-B et B-A n'est pas la même (c'est le cas en présence d'un écoulement fluide par exemple) a été étudié par *Wapenaar et al.* (2006); *Godin* (2007).

Parallèlement à ces travaux théoriques, les corrélations de bruit ambiant ont été utilisées avec succès dans divers domaine, notamment :
1) En héliosismologie, le temps de parcours d'ondes P entre divers point de la surface du soleil a pu être mesuré par *Duvall et al.* (1993); *Gilles et al.* (1997)
2) En acoustique (*Lobkis and Weaver* (2001a); *Weaver and Lobkis* (2001); *Larose et al.* (2004b))
3) En sismologie *Campillo and Paul* (2003) ont montré que la corrélation de coda issues de différents séismes enregistrés par deux stations contenait la fonction de Green du milieu. Nous reviendrons sur l'utilisation de corrélation en sismologie dans la section suivante.
4) En océanographie *Roux and Kuperman* (2004); *Sabra et al.* (2005e) ont montré que les ondes directes et réfléchies peuvent être retrouvées en corrélant du bruit ambiant.

2.1.1 Corrélation de bruit de fond sismique

D'un point de vue théorique la sismologie diffère des autres domaines : le milieu étant élastique, il existe différents type d'ondes (P,S, ondes de surface) par opposition à l'acoustique ou à l'héliosismologie où on ne considère que des ondes scalaires. Dans le cas élastique, la corrélation de bruit converge vers la fonction de Green du milieu à condition que les différentes composantes du champ d'ondes respectent la condition d'équipartition (*Sánchez-Sesma et al.* (2006a,b)). Ceci est en pratique réalisé lorsque des sources de bruit aléatoire sont distribuées dans l'ensemble du milieu, ou lorsque des sources ayant une répartition discrète éclairent un milieu diffusant. Ce dernier cas correspond à la coda sismique.

Dès les années 50, *Aki* (1957) a proposé d'étudier la subsurface en se servant du bruit sismique pour mesurer la dispersion des ondes de surface. *Shapiro and Campillo* (2004) ont montré pour la première fois, que les ondes de surface étaient visibles sur des corrélations de bruit sismique entre des stations séparées par des distances allant de la centaine au millier de kilomètres. Ils ont ainsi pu mesurer des courbes de

dispersion sur une gamme de périodes comprises entre 5 et 150 s, les résultats obtenus étant en bon accord avec les modèles de terre globale.

Cette étude a permis d'envisager d'utiliser des corrélations de bruit pour faire de la tomographie à l'échelle régionale. La première application a été en Californie où *Shapiro et al.* (2005); *Sabra et al.* (2005c) ont pu obtenir des cartes vitesse de groupe dont la résolution spatiale est nettement meilleure que celle obtenue avec des méthodes actives. A une plus petite échelle, *Brenguier et al.* (2007b) ont pu étudier le volcan du Piton de la Fournaise sur l'île de la Réunion, et imager son conduit d'alimentation. Par la suite *Brenguier et al.* (2007a) ont mis en évidence des déformations survenant au sein du volcan avant et après une éruption, franchissant ainsi une étape vers la prédiction de ces éruptions.

En marge de ces applications terrestres, *Larose et al.* (2005), en utilisant des enregistrements issus de la mission Apollo 17, ont pu montrer que des corrélations de bruit enregistré sur la Lune permettaient de mesurer la vitesse de propagation des ondes de surface sur de petites distances. Le "bruit sismique" est dans ce cas dû à l'activation de fractures sous l'effet du fort contraste de température entre le jour et la nuit. Cette étude laisse entrevoir la possibilité de faire de la sismologie sur des planètes où il n'y a ni séisme, ni océan ou atmosphère générant du bruit.

2.2 Approches théoriques

Dans cette partie, nous présentons deux approches théoriques simples, le but étant principalement de comprendre intuitivement pourquoi les corrélations de bruit convergent vers la fonction de Green du milieu : la première est basée sur une analogie entre corrélation et expérience de retournement temporel, la seconde utilise la décomposition modale des signaux enregistrés. Une approche plus générale est présentée dans les chapitres 3 et 4.

2.2.1 Équivalence entre corrélation de bruit et expérience de retournement temporel

Dans cette partie nous considérons un milieu ouvert. A la différence de la section précédente celui-ci peut-être homogène ou non. Notre objectif est de démontrer que la corrélation du bruit enregistré entre deux points A et B est la fonction de Green du milieu. Nous procédons en deux étapes : dans un premier temps nous montrons que corrélation et expérience de retournement temporel sont identiques. Nous en déduisons ensuite que la corrélation converge vers la fonction de Green.

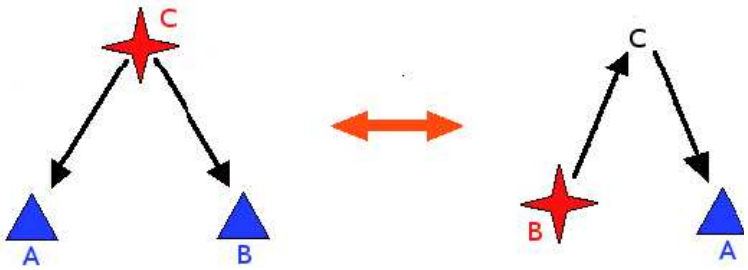

FIG. 2.1: Les deux expériences suivantes sont équivalentes : a) On corrèle les bruit de fond émis en C et enregistré en A et B. b) B émet un signal, C le retourne et le renvoie vers A.

On considère une source émettant un signal $e(t)$ au point C. Le signal enregistré en A est $e(t) \otimes h_{AC}(t)$, où $\otimes$ est la convolution, et $h_{AC}(t)$ désigne la réponse impulsionnelle entre A et C. De même en B on enregistre $e(t) \otimes h_{BC}(t)$. En sachant que $C_{xy} = x(t) \otimes y(-t)$, la corrélation du champ enregistré en A et B s'écrit :

$$C_{AB} = e(t) \otimes h_{AC}(t) \otimes e(-t) \otimes h_{BC}(-t) \quad (2.1)$$
$$= h_{AC}(t) \otimes h_{BC}(-t) \otimes f(t) \quad (2.2)$$

où $f(t) = e(t) \otimes e(-t)$. Considérons à présent l'expérience de pensée suivante (figure 2.2) : B émet un pulse, C enregistre la réponse impulsionnelle $h_{CB}(t)$, retourne ce signal et renvoie $h_{CB}(-t)$. A enregistre alors : $h_{CB}(-t) \otimes h_{AC}(t)$. Nous reconnaissons l'expression précédente de $C_{AB}(t)$. Les deux expériences sont donc équivalentes !

Allons plus loin et imaginons qu'au lieu d'avoir un seul point C nous en ayons un ensemble continu entourant les stations A et B. Dans un premier temps A envoie un Dirac qui se propage dans toutes les directions. Il est enregistré en chaque point C. Parmi tous les trajets suivis il en existe qui passent par B, si bien que B enregistre $h_{AB}(t)$ soit la fonction de Green que l'on recherche. Dans un second temps, les points C retournent le signal $h_{AC}(-t)$. La propagation des ondes étant réciproque, toutes les ondes émises par les points C vont se refocaliser en A, et B enregistre cette fois $h_{AB}(-t)$.

D'après ce qui précède, ceci revient à corréler des enregistrements de bruit de fond entre A et B, les sources C entourant continûment les deux récepteurs. On conclut qu'il est possible de reconstituer la fonction de Green entre deux points A et B en corrélant des enregistrements de bruit de fond à condition que celui-ci soit généré continûment autour de A et B. *Derode et al.* (2003a,b) ont en outre montré que ce résultat reste valable si les sources n'entourent pas continûment les stations, mais que le milieu est suffisamment hétérogène.

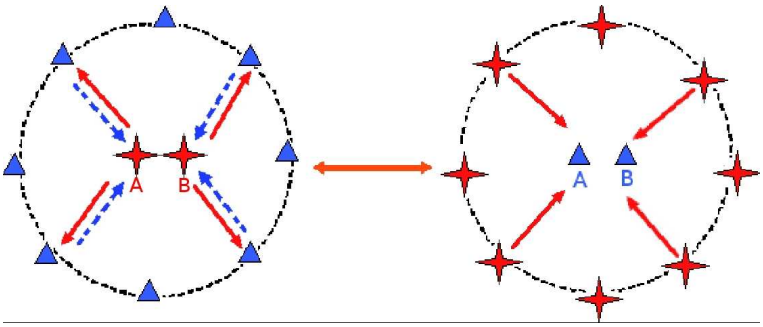

FIG. 2.2: Les deux expériences suivantes sont equivalentes : a) A émet un signal. Celui ci est enregistré par un ensemble de récepteurs qui le retournent et le réemettent. On enregistre en B. b) On corrèle les enregistrements en A et B de bruit émis par un ensemble de sources disposées continûment autour de A et B.

2.2.2 Interprétation modale (*Lobkis and Weaver*, 2001b)

Dans l'approche modale on suppose que le champ d'ondes est tel que tous les modes du milieu sont excités avec un même niveau d'énergie et une phase aléatoire. Aucune hypothèse n'est faite sur le milieu de propagation. Soient $s_A(t)$ et $s_B(t)$ les enregistrements du champ en deux points A et B. Dans l'hypothèse où il y a équipartition de l'énergie entre les différents modes propres de propagation, ces signaux peuvent s'écrire

$$\begin{aligned} s_A(t) &= \Re \sum_k a_k \, \psi_k(A) \, e^{i\omega_k t}, \\ s_B(t) &= \Re \sum_l a_l \, \psi_l(B) \, e^{i\omega_l t}, \end{aligned}$$

où les coefficients a_k représentent les amplitudes modales complexes et les $\psi_k(X)$ les formes des modes au point X, ω_k étant la pulsation de ces modes.

La corrélation entre ces deux signaux s'écrit alors

$$\begin{aligned} C_{s_A s_B}(\tau) &= \int_\infty s_A(t) \, s_b(t-\tau) \, dt, \\ &= \int_\infty \Re \left[\sum_k a_k \, \psi_k(A) \, e^{i\omega_k t} \right] \Re \left[\sum_l a_l \, \psi_l(B) \, e^{i\omega_l (t-\tau)} \right] dt, \\ &= \frac{1}{2} \Re \sum_k \langle \, a_k \, a_k^* \rangle \, \psi_k(A) \, \psi_k(B) \, e^{i\omega_k \tau}. \end{aligned}$$

La fonction de Green correspondant à un déplacement enregistré en B du à une force

appliquée en A s'écrit

$$G_{AB}(t) = \sum_k \psi_k(A)\,\psi_k(B)\,\frac{\sin(\omega_k t)}{\omega_k}.$$

Nous en déduisons que

$$2\frac{d}{dt}\left(C_{s_A s_B}(\tau)\right) = G_{AB}.$$

L'opération de dérivation introduite ici dépend de la fonction de Green considérée. En effet, on peut définir la fonction de Green de plusieurs façons en fonction des grandeurs physiques qu'elle relie. L'expression donnée plus haut correspond à une fonction de Green reliant une force à un déplacement. Si au contraire on enregistre un champ de vitesse, l'opération de dérivation n'est plus nécessaire

$$G_{AB}^{f\to v} = \frac{d}{dt}\,G_{AB}^{f\to d} = C_{s_A s_B}(\tau).$$

Ce résultat signifie que si l'équipartition est réalisée, si tous les modes du milieu sont excités avec un même niveau d'énergie et une phase aléatoire, alors la corrélation du champ en deux points est la fonction de Green du milieu. La démonstration donnée ici suppose une distribution discrète de modes qui n'est valable qu'en milieu fermé.

Chapitre 3

Cas d'une distribution volumique de source

Sommaire

3.1 Introduction

Dans le chapitre précédent nous avons vu que la corrélation de bruit convergeait vers la fonction de Green, en se servant de l'analogie entre corrélation et expérience de retournement temporel. Si cette approche à l'avantage d'être abordable et permet de "démystifier" les corrélations, elle a toutefois l'inconvénient d'être peu générale. Elle nécessite de supposer une disposition particulière de sources, et n'est valable qu'en acoustique (car nous avons supposer des ondes scalaires). Nous souhaitons obtenir un résultat beaucoup plus général, valable pour un milieu quelconque, et pouvant s'appliquer quelque soit la physique régissant la propagation des ondes.

Les travaux présentés dans ce chapitre et le suivant font suite à une série de séminaires de mathématique donnée par Yves Colin de Verdière au LGIT pendant plus d'un an. Ces séminaires ont été l'occasion d'aborder les problèmes posés par les corrélations de bruit, et ont permis de formuler une théorie plus générale. Ces travaux ont

d'abord été publiés à destination de mathématiciens (*Colin de Verdière* (2006a,b)), avant d'être repris dans l'article de review de *Gouédard et al.* (2007) en annexe du présent manuscrit. Tout en suivant la même démarche que *Gouédard et al.* (2007), nous présentons ici les principaux résultats, en donnant plus de détail.

3.2 Hypothèses

Nous souhaitons montrer que la corrélation du bruit de fond enregistré en deux points A et B d'un milieu contient la fonction de Green complète entre ces deux points dans le cas le plus général possible. Dans cette partie nous nous intéressons spécifiquement au cas où les sources de bruit sont réparties de façons homogène dans l'ensemble du milieu. Aucune hypothèse n'est formulée concernant le milieu de propagation, si ce n'est qu'il doit être atténuant. Il peut-être homogène ou non, avec ou sans diffuseurs.

Soit X un milieu quelconque. Nous supposons que les ondes se propagent au sein de X suivant l'équation

$$\frac{\partial^2 u}{\partial t^2} + 2a\frac{\partial u}{\partial t} - Lu = f, \tag{3.1}$$

$a(\vec{r}) > 0$ étant l'atténuation du milieu. Le second membre de l'équation, $f(\vec{r},t)$, représente les sources de bruit du milieu, et $u(\vec{r},t)$ le champ de déplacement. Tout l'intêret de cette partie réside dans le terme L qui désigne un opérateur auto-adjoint elliptique différentiel quelconque, c'est à dire un opérateur tel que la propagation des ondes respecte la conservation de l'énergie. Il peut s'agir du laplacien $c^2(\vec{r})\Delta$ auquel cas nous reconnaissons l'équation d'onde habituelle, mais L pourrait être également l'opérateur de Schrödinger ou autre. C'est ce qui confère une grande généralité à cette approche, celle-ci n'étant pas limitée à la sismologie.

Dans un premier temps nous montrons que la transformée de Fourier de la fonction de Green entre deux points quelconque du milieu X est liée au noyau intégral de l'opérateur L. En exprimant ensuite le champ de déplacement en A et B à l'aide des fonction de Green et des sources f, nous montrons que la dérivée de la corrélation du bruit enregistré en deux points est la fonction de Green recherchée.

3.3 Définition de la fonction de Green dans le domaine fréquentiel

3.3.1 Noyau intégral d'un opérateur

En algèbre linéaire, il est connu que toute forme linéaire P sur un espace vectoriel $\mathbb{E}$ peut se mettre sous une forme matricielle. Les coefficients de la matrice P_{ij} sont l'image des vecteurs e_i formant une base de $\mathbb{E}$ par l'opérateur P. Une fois définie, la matrice P_{ij} permet de calculer l'image d'un vecteur quelconque u par P selon la relation

$$\forall u : X \longmapsto \mathbb{R}^3,\ \big(P\,u\big)_i = \sum_j P_{ij}\,u_j. \tag{3.2}$$

De la même manière, un opérateur P ayant un spectre continu[1] peut se mettre sous la forme d'une "matrice continue" que l'on appelle noyau intégral de l'opérateur et que l'on note $[\![P]\!](x,y)$. L'image d'un vecteur u par P s'écrit alors au moyen d'une intégrale au lieu d'une somme :

$$\forall u : X \longmapsto \mathbb{R}^3,\ \big(P\,u\big)(x) = \int_X [\![P]\!](x,y)\,u(y)\,dy. \tag{3.3}$$

Tout opérateur de spectre continu peut se mettre sous la forme d'un noyau intégral. Celui-ci caractérise complètement l'opérateur.

3.3.2 Fonction de Green dans le domaine fréquentiel

Par souci de simplicité, nous commençons par considérer le cas où le milieu X n'a pas d'atténuation : $a = 0$. La fonction de Green entre deux points $\vec{r}$ et $\vec{r}_s$ représente l'enregistrement qu'on obtiendrait en $\vec{r}$ si une source impulsionelle était placé en $\vec{r_s}$. En d'autres termes, la fonction de Green dans le domaine temporel $G(t,\vec{r},\vec{r_s})$ est la solution de l'équation d'onde 3.1 lorsque la source f est un Dirac $\delta(t,\vec{r}-\vec{r_s})$

$$\frac{\partial^2 G}{\partial t^2}(t,\vec{r},\vec{r}_s) - L\,G(t,\vec{r},\vec{r}_s) = \delta(t)\,\delta(\vec{r}-\vec{r}_s). \tag{3.4}$$

Nous souhaitons montrer que la fonction de Green dans le domaine fréquentiel peut-être définie comme étant l'opposée du noyau intégral de $((\omega+i\epsilon)^2+L)^{-1}$, soit

$$\hat{G}(\omega+i\epsilon,\vec{r},\vec{r}_s) = -\big[\!\big[\big((\omega+i\epsilon)^2+L\big)^{-1}\big]\!\big](\vec{r},\vec{r}_s), \tag{3.5}$$

[1] Le spectre d'un opérateur est l'ensemble de ses valeurs propres

et que cette définition est équivalente à la précédente. Dans cette expression, la notation $\hat{.}$ indique que la fonction est prise dans l'espace des fréquences, et ϵ est un nombre positif infinitésimal. Lorsque $\epsilon \to 0$ nous pouvons écrire

$$\begin{aligned}
\hat{G}(\omega + i\epsilon, \vec{r}, \vec{r}_s), &= -\left[\!\left[\left((\omega + i0)^2 + L\right)^{-1}\right]\!\right](\vec{r}, \vec{r}_s), \\
&= -\int_X \left[\!\left[\left((\omega + i0)^2 + L\right)^{-1}\right]\!\right](\vec{r}, \vec{r}')\, \delta(\vec{r}' - \vec{r}_s)\, d\vec{r}', \\
&= -\left((\omega + i0)^2 + L\right)^{-1} \delta(\vec{r} - \vec{r}_s).
\end{aligned}$$

Ceci mène à

$$-\left((\omega + i0)^2 + L\right) \hat{G}(\omega + i0, \vec{r}, \vec{r}_s) = \delta(\vec{r} - \vec{r}_s).$$

Nous reconnaissons dans cette dernière expression la transformée de Fourier de la relation 3.4 définissant la fonction de Green dans le domaine temporel. La fonction de Green tel que nous l'avons définie dans le domaine fréquentiel dans 3.5 est donc bien solution de l'équation d'onde lorsque la source est un Dirac.

Nous pouvons calculer la transformée de Fourier inverse de $\hat{G}(\omega + i\epsilon, x, y)$, en utilisant la méthode des résidus :

$$G(t, \vec{r}, \vec{r}_s) = Y(t) \left[\!\left[\frac{\sin t\sqrt{-L}}{\sqrt{-L}} \right]\!\right](\vec{r}, \vec{r}_s). \tag{3.6}$$

Cette relation indique que la fonction de Green d'un milieu dépend du noyau intégral de l'opérateur L controllant la propagation. La notation $\sqrt{-L}$ désigne l'opérateur dont les valeurs propres sont les images des valeurs propes de L par la fonction $x \to \sqrt{(-x)}$. Il en va de même pour la fonction sinus. $Y(t)$ est la fonction de Heaviside valant 0 pour les temps négatifs et 1 pour les temps positifs. Elle assurre que la solution est bien causale.

Nous considérons à présent le cas plus général où le milieu est atténuant. La fonction de Green $\hat{G}(\omega, \vec{r}, \vec{r_s})$ est définie comme le noyau intégral de $(\omega^2 + 2ia\omega + L)^{-1}$ et non plus de $((\omega + i\epsilon)^2 + L)^{-1}$, soit

$$\hat{G}(\omega + i\epsilon, \vec{r}, \vec{r}_s) = -\left[\!\left[\left((\omega + i\epsilon)^2 + L\right)^{-1}\right]\!\right](\vec{r}, \vec{r}_s), \tag{3.7}$$

3.4 Corrélation de bruit de fond

Nous définissons la corrélation du champ de déplacement en deux point A et B par

$$C(\tau, \vec{r}_A, \vec{r}_B) = \lim_{T \to +\infty} \frac{1}{T} \int_0^T u(t, \vec{r}_A)\, \overline{u(t+\tau, \vec{r}_B)}\, dt. \tag{3.8}$$

Le déplacement $u(t,\vec{r})$ peut être exprimé à partir de la fonction de Green G et des sources f

$$u(t,\vec{r}) = \int_0^\infty dt' \int_X G_a(t',\vec{r},\vec{r}_s)\, f(t-t',\vec{r}_s)\, d\vec{r}_s. \tag{3.9}$$

Nous supposons que f est un bruit blanc distribué de façon homogène dans l'ensemble du milieu X. Un bruit blanc a un spectre plat contenant toute les fréquences avec un même niveau d'énergie, la phase étant aléatoire. Dans le domaine temporel, l'autocorrélation d'un bruit blanc enregistré en un point est un Dirac. La corrélation de bruit blanc en deux points différent est nulle.

En exprimant $u(t,\vec{r})$ en fonction de G, comme dans l'équation 3.9, la corrélation du champ de déplacement en deux points A et B s'écrit

$$\begin{aligned} C(\tau,\vec{r}_A,\vec{r}_B) &= \lim_{T\to+\infty} \frac{1}{T}\int_0^T u(t,\vec{r}_A)\,\overline{u(t+\tau,\vec{r}_B)}\,dt, &(3.10)\\ &= \lim_{T\to+\infty} \frac{1}{T}\int_0^T dt \int_0^\infty ds \int_X d\vec{r}_s\, G_a(s,\vec{r}_A,\vec{r}_s)\, f(t-s,\vec{r}_s) \\ &\qquad \times \int_0^\infty ds' \int_X d\vec{r}_s{}'\, \overline{G_a(s',\vec{r}_B,\vec{r}_s{}')\, f(t+\tau-s',\vec{r}_s{}')}. &(3.11)\end{aligned}$$

En utilisant la "loi des grands nombres", la limite lorsque $T\to\infty$ peut être remplacée par l'espérance $\mathbb{E}$

$$\lim_{T\to+\infty} \frac{1}{T}\int_0^T f(t-s,\vec{r}_s)\, f(t+\tau-s',\vec{r}_s{}')\,dt \;=\; \mathbb{E}\big[f(t-s,\vec{r}_s)\, f(t+\tau-s',\vec{r}_s{}')\big].$$

En utilisant le fait que f est un bruit blanc nous avons

$$\mathbb{E}\big[f(t-s,\vec{r}_s)\, f(t+\tau-s',\vec{r}_s{}')\big] = \sigma^2\,\delta(\tau+s-s')\,\delta(\vec{r}_s-\vec{r}_s{}'),$$

où σ est la variance du bruit blanc. En utilisant ce résultat, l'équation 3.10 devient

$$C(\tau,\vec{r}_A,\vec{r}_B) = \sigma^2 \int_0^\infty ds \int_X d\vec{r}_s\, G_a(s,\vec{r}_A,\vec{r}_s)\,\overline{G_a(s+\tau,\vec{r}_B,\vec{r}_s)}. \tag{3.12}$$

Nous pouvons à présent remplacer G_a par son expression vue dans l'equation 3.7

$$\begin{aligned} C(\tau,\vec{r}_A,\vec{r}_B) &= \sigma^2 \int_0^\infty ds \int_X d\vec{r}_s\, Y(s)\, Y(s+\tau)\, e^{-a\,s}\, e^{-a\,(s+\tau)} \\ &\qquad \left[\!\!\left[\frac{\sin s\sqrt{-L-a^2}}{\sqrt{-L-a^2}} \right]\!\!\right](\vec{r}_A,\vec{r}_s)\, \overline{\left[\!\!\left[\frac{\sin (s+\tau)\sqrt{-L-a^2}}{\sqrt{-L-a^2}} \right]\!\!\right](\vec{r}_B,\vec{r}_s)}. \end{aligned}$$

Nous sommes ici obligés de supposer le milieu atténuant, c'est à dire $a > 0$, sans quoi l'intégrale diverge. En utilisant les deux propriétés suivantes des noyaux intégrals

$$\begin{aligned} \overline{[\![P]\!](x,y)} &= [\![\overline{P}]\!](x,y) = [\![P]\!](y,x), \\ \int_X [\![P_1]\!](x,z)\ [\![P_2]\!](z,y)\,dz &= [\![P_1 \cdot P_2]\!](x,y), \end{aligned}$$

nous pouvons exprimer la corrélation de la façon suivante

$$\begin{aligned} C(\tau,\vec{r}_A,\vec{r}_B) &= \sigma^2 \int_0^\infty ds\, Y(s+\tau)\ e^{-a\,(2\,s+\tau)} \\ &\qquad \left[\!\!\left[\frac{\sin s\sqrt{-L-a^2}}{\sqrt{-L-a^2}}\ \frac{\sin\,(s+\tau)\sqrt{-L-a^2}}{\sqrt{-L-a^2}} \right]\!\!\right](\vec{r}_A,\vec{r}_B). \end{aligned}$$

Cette expression se simplifie en utilisant les relations trigonométriques : $\sin\alpha\,\sin\beta = 1/2\,\big(\cos(\alpha-\beta)-\cos(\alpha+\beta)\big)$ ce qui nous permet de calculer l'intégrale selon ds

$$C(\tau,\vec{r}_A,\vec{r}_B) = \frac{\sigma^2\,e^{-a\,|\tau|}}{4\,a} \left[\!\!\left[(-L)^{-1}\ \left(\cos\tau\sqrt{-L-a^2} + a\,\frac{\sin|\tau|\sqrt{-L-a^2}}{\sqrt{-L-a^2}} \right) \right]\!\!\right](\vec{r}_A,\vec{r}_B).$$

La dérivée par rapport au temps de cette dernière équation fait apparaitre la fonction de Green du milieu (*Colin de Verdière* (2006a)) :

$$\frac{d}{d\tau}\,C(\tau,\vec{r}_A,\vec{r}_B) = \frac{-\sigma^2}{4\,a}\big(G_a(\tau,\vec{r}_A,\vec{r}_B) - G_a(-\tau,\vec{r}_A,\vec{r}_B)\big) \tag{3.13}$$

Ce résultat signifie que la dérivée de la corrélation du champ de déplacement entre deux points A et B est la fonction de Green complète du milieu entre A et B, contenant tous les modes de propagation.

Pour parvenir à ce résultat, aucune hypothèse sur le milieu de propagation n'a besoin d'être formulée. Celui-ci peut-être quelconque, la seule contrainte étant que l'atténuation soit non nulle. L'intêret de cette démarche réside en outre dans le fait que nous n'avons pas besoin d'écrire explicitement l'opérateur L controllant la propagation des ondes, celui-ci doit simplement respecter la conservation de l'énergie. Le lien entre corrélation et fonction de Green n'est donc pas spécifique à la sismologie ou à l'acoustique, c'est au contraire une relation très générale en physique.

Si aucune hypothèse n'a besoin d'être formulée quant au milieu de propagation, nous avons supposé que les sources de bruit étaient réparties dans tout le milieu. Ce n'est pas le cas en sismologie : le bruit en dessous de 1 Hz provient essentiellement des océans alors que les stations sont situées sur les continents. Il est donc nécessaire de formuler une approche plus générale se passant de cette hypothèse. Ceci est l'objet du chapitre suivant.

Chapitre 4

Cas où l'équipartition est réalisée sur les bords du milieu

Sommaire

4.1 Introduction

Dans le chapitre précédent nous avons vu que la dérivée de la corrélation entre deux points A et B d'un bruit blanc généré dans l'ensemble d'un milieu était la fonction de Green entre A et B. Ce résultat est à la fois très général - aucune hypothèse concernant le milieu n'ayant été formulée - et très limité car suppose une distribution homogène des sources. Nous étendons ici ce résultat dans le cas où l'équipartition est réalisée uniquement en périphérie du milieu étudié.

Tout comme au chapitre précédent, nous considérons un milieu X quelconque au sein duquel les ondes se propagent selon l'équation

$$\frac{\partial^2 u}{\partial t^2} + 2a\frac{\partial u}{\partial t} - Lu = f. \tag{4.1}$$

Dans un premier temps nous montrons que la corrélation du bruit enregistré en deux points peut s'écrire en fonction du projecteur spectral de l'opérateur L. La seconde étape de la démonstration consiste à écrire la fonction de Green entre deux points quelconques en fonction du noyau intégral de ce même projecteur. Nous en déduisons ensuite que la corrélation de bruit est proportionnelle à la partie imaginaire de la transformée de Fourier de la fonction de Green du milieu, ce qui est le résultat recherché. Tout comme au chapitre précédent, nous présentons les points essentiels de la démonstration suivant la démarche de *Gouédard et al.* (2007), plus de détails pouvant être trouvés dans *Colin de Verdière* (2006a,b).

4.2 Définitions préalables

4.2.1 Modes propres d'un milieu diffusant

Les modes propres d'un milieu homogène infini sont l'ensemble des ondes planes $e_0(\vec{r},\vec{k}) = e^{i\vec{k}.\vec{r}}$. Pour un milieu complexe, comportant des hétérogénéités dans une région finie tout en étant homogène à l'infini, les modes propres sont la somme des modes propres du milieu homogène et des ondes diffusées (*Ramm* (1986); *Reed and Simon* (1978))

$$e(\vec{r},\vec{k}) \quad = \quad e_0(\vec{r},\vec{k}) + e_s(\vec{r},\vec{k}), \tag{4.2}$$

e_s sont les ondes diffusées par les hétérogénéités du milieu. Leurs amplitudes tend vers zéro lorsque $\vec{r}$ tend vers l'infini (condition de *Sommerfeld*). Cette décomposition est valable en tout points du milieu, y compris à proximité des diffuseurs.

Ce résultat implique que si l'équipartition est réalisée sur les bords du milieu elle l'est également au sein du milieu. Ceci constitue la pierre angulaire de la démonstration.

4.2.2 Projecteur Spectral

Soit I un intervalle de $\mathbb{R}_+$. Nous introduisons le projecteur spectral P_I, projetant sur les modes propres $e(\vec{r},\vec{k})$ de l'opérateur L associés aux valeurs propres λ_k de l'intervalle I par son noyau intégral

$$[\![P_I]\!](\vec{r}_1,\vec{r}_2) = (2\,\pi)^{-d} \int_{\lambda_k \in I} e(\vec{r}_1,\vec{k})\,\overline{e(\vec{r}_2,\vec{k})}\,|d^d\vec{k}|, \tag{4.3}$$

où d est la dimension de l'espace (typiquement $d = 3$).

4.3 Lien entre la corrélation et le projecteur spectral de l'opérateur L

Soit I un intervalle centré autour de la pulsation ω^2, $I = [\omega_-^2, \omega_+^2]$. Nous souhaitons écrire explicitement le projecteur spectral P_I projetant sur I. L'intégrale de l'équation 4.3 se fait autour d'un volume de dimension d. Pour pouvoir calculer cette intégrale, nous la décomposons en deux intégrales, l'une selon un volume de dimension $d-1$ tel que $c^2|\vec{k}|^2 = \omega^2$, l'autre selon $|\vec{k}|$

$$[\![P_I]\!](\vec{r}_1, \vec{r}_2) = (2\,\pi)^{-d} \int_{c^2|\vec{k}|^2 \in I} \int_{c^2|\vec{k}|^2=\omega^2} e(\vec{r}_1, \vec{k})\, \overline{e(\vec{r}_2, \vec{k})}\, |d^{d-1}\sigma|\, |\vec{k}|^{d-1}\, d|\vec{k}|. \qquad (4.4)$$

Dans le cas où le milieu est de dimension 3, $d^{d-1}\sigma = d^2\sigma$ est l'angle solide. En dérivant cette expression par rapport à ω_+, nous obtenons

$$\frac{d}{d\omega_+}[\![P_I]\!](\vec{r}_1, \vec{r}_2) = \frac{(2\,\pi)^{-d}}{c} \left(\frac{\omega}{c}\right)^{d-1} \int_{c^2|\vec{k}|^2=\omega^2} e(\vec{r}_1, \vec{k})\, \overline{e(\vec{r}_2, \vec{k})}\, |d^{d-1}\sigma|. \qquad (4.5)$$

Comme nous avons supposé l'équipartition sur les bords du milieu, les ondes planes $e(\vec{r}, \vec{k}) = e_0(\vec{r}, \vec{k}) + e_s(\vec{r}, \vec{k})$ sont précisément les modes propres du milieu (cf section 4.2.1). Cette expression est en outre similaire à la transformée de Fourier de la corrélation du champ d'ondes enregistré en $\vec{r}_1$ et $\vec{r}_2$

$$\hat{C}(\omega, \vec{r}_1, \vec{r}_2) \;=\; \frac{1}{\sigma_{d-1}} \int_{c^2|\vec{k}|^2=\omega^2} e(\vec{r}_1, \vec{k})\, \overline{e(\vec{r}_2, \vec{k})}\, |d\sigma|, \qquad (4.6)$$

σ_{d-1} correspond au volume d'une sphère de dimension $d-1$ de rayon 1 : $\sigma_0 = 2$, $\sigma_1 = 2\,\pi$, $\sigma_2 = 4\,\pi$, ... En combinant les équations 4.5 et 4.6, nous obtenons la relation

$$\frac{d}{d\omega}[\![P_I]\!](\vec{r}_1, \vec{r}_2) = \frac{\sigma_{d-1}}{(2\,\pi)^d}\, \frac{1}{c} \left(\frac{\omega}{c}\right)^{d-1} C_\omega(\vec{r}_1, \vec{r}_2). \qquad (4.7)$$

Cette relation formalise le lien entre l'opérateur L, dont dépend la propagation des ondes, et la corrélation du champ d'ondes, en montrant que la corrélation du champ entre deux points $\vec{r_1}$ et $\vec{r_2}$ peut s'écrire en fonction du noyau intégral du projecteur spectral P_I de l'opérateur L.

4.4 Lien entre le projecteur spectral de l'opérateur L et la fonction de Green du milieu

Le projecteur spectral P_I défini précédemment peut également s'écrire en fonction de l'opérateur L à l'aide de la formule de Cauchy

$$P_I = \frac{1}{2\,i\,\pi} \int_{\gamma_I} \big(L+\lambda\big)^{-1}\, d\lambda, \tag{4.8}$$

γ_I est un contour dans le plan complexe dont la partie réelle est l'intervalle I.

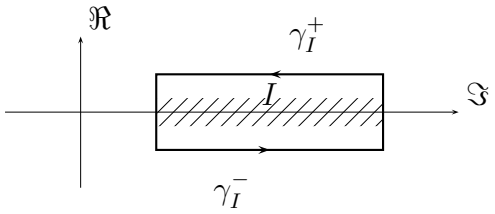

FIG. 4.1: γ_I peut-être décomposé en deux contours γ_I^+ and γ_I^- qui sont complexe conjugués et correspondent à des directions opposées.

Le contour γ_I peut être décomposé en deux contours définis par $\gamma_I^+ = \big\{\lambda \in \gamma_I | \Im(\lambda) \geq 0\big\}$ et $\gamma_I^- = \big\{\lambda \in \gamma_I | \Im(\lambda) < 0\big\}$ ($\Im$ correspond à la partie imaginaire) comme l'indique la figure Fig. 4.1. Comme γ_I^+ et γ_I^- sont complexe conjugués, nous obtenons

$$\begin{aligned} P_I &= \frac{1}{2\,i\,\pi} \int_{\gamma_I^+} \Big[\big(L+\lambda\big)^{-1} - \big(L+\overline{\lambda}\big)^{-1}\Big]\, d\lambda, \\ &= \frac{1}{\pi} \int_{\gamma_I^+} \Im\big(L+\lambda\big)^{-1}\, d\lambda. \end{aligned}$$

En prenant le noyau intégral de cette expression nous obtenons

$$\begin{aligned} [\![P_I]\!] &= \frac{1}{\pi} \int_{\gamma_\varepsilon^+} \Im[\![\big(L+\lambda\big)^{-1}]\!]\, d\lambda, \\ &= -\frac{1}{\pi} \int_{\omega_-}^{\omega_+} \Im[\![\big(L+(\omega+i0)^2\big)^{-1}]\!]\, 2\,\omega\, d\omega. \end{aligned}$$

Ceci mène à la formule de Stone, en utilisant la définition de $\hat{G}$:

$$[\![P_I]\!](\vec{r}_1,\vec{r}_2) = -\frac{2}{\pi} \int_{\omega_-}^{\omega_+} \omega\, \Im\hat{G}(\omega,\vec{r}_1,\vec{r}_2)\, d\omega.$$

En dérivant cette dernière expression par rapport à ω_+, nous avons

$$\frac{d}{d\omega_+}[\![P_I]\!](\vec{r}_1,\vec{r}_2) = -\frac{2\,\omega}{\pi}\, \Im\hat{G}(\omega,\vec{r}_1,\vec{r}_2). \tag{4.9}$$

En combinant les équations 4.7 et 4.9 nous obtenons finalement

$$\hat{C}(\omega, \vec{r}_1, \vec{r}_2) = - \frac{2^{d+1}\,\pi^{d-1}}{\sigma_{d-1}} \frac{c^d}{\omega^{d-2}} \Im\hat{G}(\omega, \vec{r}_1, \vec{r}_2). \tag{4.10}$$

Ceci signifie que la corrélation du bruit enregistré en $\vec{r}_1$ et $\vec{r}_2$ est la partie imaginaire de la transformée de Fourier de la fonction de Green du milieu entre $\vec{r}_1$ et $\vec{r}_2$. Il est à noter que le facteur $1/\omega^{d-2}$ dans le membre de gauche de l'équation 4.10 correspond à une intégration dans le domaine de Fourier. Ceci implique qu'en dimension 2, c'est bien la corrélation qui est proportionnelle à la fonction de Green, tandis qu'en dimension 3 il s'agit de la dérivée de la corrélation (tout comme dans le cas d'une distribution volumique de sources étudiée au chapitre précédent).

La relation 4.10 est une généralisation de l'équation 3.13. Nous ne supposons plus que le milieu est atténuant, ni une distribution volumique des sources. Nous supposons simplement que le bruit est équipartitionné (tout les modes sont excités avec un même niveau d'énergie et une phase aléatoire) en bordure de la zone étudiée. Cela suffit à garantir que la corrélation converge la fonction de Green du milieu, quelque soit le champ d'ondes au sein du milieu.

Deuxième partie

Origine du bruit de fond sismique

Chapitre 5

A Study of the seismic noise from its long range correlation properties

L. Stehly, M. Campillo, N.M. Shapiro
Article publié dans *Journal of Geophysical Research* (2006)

Sommaire

5.1 Introduction à l'article

La surface de la terre vibre en permanence, sans relâche jour et nuit, été comme hiver. Le spectre de ces vibrations continues contient des hautes fréquences $> 1Hz$, et s'étend jusqu'à des périodes de plusieurs centaines de secondes, excitant ainsi les modes propres de la terre. Ce "bruit de fond" n'est pas du à l'activité sismique,

dont l'intensité n'est pas suffisante pour expliquer son amplitude (*Tanimoto and Um* (1999)). De même l'amplitude du bruit change selon les saisons, si bien qu'il ne peut être lié à la tectonique (*Tanimoto and Um* (1999)). Quelque soit la bande de fréquence considérée, le bruit est dominé par les ondes de surface (*Friedrich et al.* (1998), *Ekström* (2001), *Nishida* (2002)). Cela implique qu'il est généré à la surface de la terre.

Nous avons vu dans la partie précédente que ce "bruit" pourrait être utile pour imager la terre : il est possible de reconstruire la fonction de Green complète d'un milieu entre n'importe quelle paire de stations, en corrélant simplement le bruit ambiant enregistré par ces stations. Cela laisse entrevoir la possibilité de faire de la tomographie sismique "sans source", c'est-à-dire sans séisme ni explosion.

Toutefois pour que cela soit possible, d'un point de vue théorique, le bruit doit être équipartitionné en bordure de la zone étudiée (tous les modes propres doivent être excités avec un même niveau d'énergie). Afin de voir dans quelle mesure le bruit réel respecte cette condition, il est nécessaire d'étudier son origine, de localiser ses sources. Nous commençons tout d'abord par faire le point brièvement sur ce qui est connu concernant l'origine du bruit sismique puis nous présentons notre propre étude.

Bruit Microsismique

Entre 5 et 20s de période, le bruit est appelé "bruit microsismique" bien qu'il ne soit nullement lié à la sismicité. La figure 5.1 montre le spectre d'une journée de bruit enregistré en Allemagne par la station BFO. Celui-ci est dominé par deux pics, l'un très marqué à 7s, l'autre plus modéré à 14s. Ceci n'est pas spécifique à l'Europe, les mêmes observations peuvent être réalisées sur n'importe quel continent.

Le premier pic a une période de 14s, ce qui correspond également à la période dominante des vagues. Il est probablement généré directement par les variations de pression induites par les vagues au niveau du plancher océanique. Le second a une période de 7s, sa fréquence est donc exactement le double du premier. On pense qu'il est généré par l'interaction non linéaire de vagues ayant une même fréquence mais se propageant dans des sens opposés. Selon *Longuet-Higgins* (1950) ceci donne naissance à une variation de pression au sein de la colonne d'eau indépendante de la profondeur, et dont la fréquence est le double de celles des vagues interagissant (soit typiquement 5-10s). Cette fluctuation de pression n'est associée à aucun mouvement de particule. Lorsque la profondeur du plancher océanique est adéquate, elle peut entrer en résonance avec le sol, donnant naissance à des ondes sismiques de même période (5-10s). Cette interaction non linéaire nécessite que des vagues se propageant dans des sens opposées se rencontrent. Elle pourrait avoir lieu par exemple, le long des côtes, celles-ci réfléchissant les ondes incidentes.

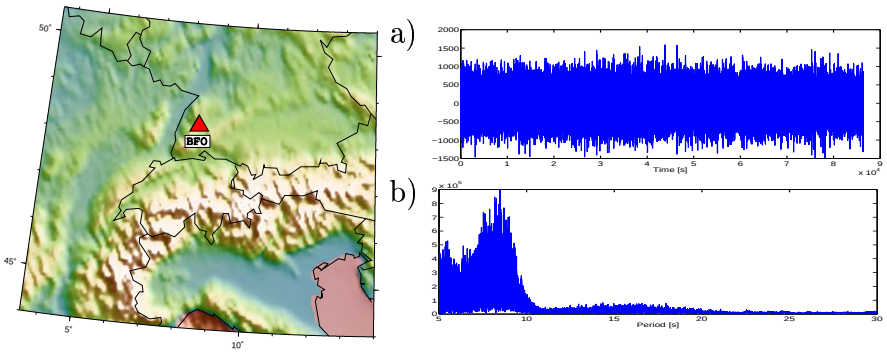

FIG. 5.1: a) Enregistrement de bruit de fond sismique par la station BFO (Allemagne) le 15 janvier 2005. b) Transformée de Fourier de ce même enregistrement. Le pic de 7s domine le spectre, le pic de 14s plus modéré est également visible.

Diverses tentatives ont été réalisées afin de localiser les régions dont provient le bruit microsismique. *Friedrich et al.* (1998) ont montré que le bruit microsismique enregistré en Allemagne durant l'hiver 95-96 provient de zones précises, indépendamment des conditions météo, situées dans la mer Norvégienne, l'océan atlantique et peut-être dans la Méditerranée. En étudiant le bruit de la côte Ouest des États-Unis *Schulte-Pelkum et al.* (2004) parviennent une conclusion proche : le bruit microsismique est stable, et provient constamment de la même direction.

Bruit à très longues périodes : le "Hum'

Dans les très longues périodes (100-500s) le bruit que l'on appelle alors souvent le "hum" excite les modes propres de la terre (*Nawa et al.* (1998); *Suda et al.* (1998); *Tanimoto et al.* (1998); *Roult and Crawford* (2000); *Kobayashi and Nishida* (1998); *Nishida et al.* (2000)). Les sources qui le génèrent changent avec les saisons : le "hum" provient de l'hémisphère nord en hiver, et de l'hémisphère sud en été (*Rhie and Romanowicz* (2004)). Ce comportement est bien corrélé avec les variations saisonnières de l'amplitude des vagues. Ceci suggère que le hum est généré par un couplage entre l'atmosphère, l'océan et la terre.

Les observations à des stations sismiques sous marines en Californie révèlent que l'amplitude des ondes infragravitaires est liée localement à l'énergie des vagues de plus courtes périodes (10-20s). Ceci laisse penser que les ondes infragravitaires de longues périodes sont générées localement à partir des vagues (swell) par un mécanisme non linéaire (*Dolenc et al.* (2005)). Les travaux de *Rhie and Romanowicz* (2006) vont dans le même sens, suggérant que les ondes courtes périodes générées par des tempêtes interagissent non linéairement pour produire des ondes infragravitaires longues périodes près des côtes. Une fois générée ces ondes se propagent dans l'océan profond, ou interagissent avec le plancher océanique près des côtes produisant ainsi des ondes

de Rayleigh.

Par ailleurs, *Rhie and Romanowicz* (2006) observe que le pic microsismiqe à 7s est corrélé avec le hum en hiver, mais pas pendant l'été. Ils ont alors émis l'hypothèse qu'en Californie, le bruit à 7s est toujours généré localement est qu'il est plus faible en été qu'en hiver.

Etudier l'origine du bruit de fond à partir de corrélations

Afin de cerner en pratique dans quelle mesure les corrélations de bruit sismique convergent effectivement vers la fonction de Green du milieu, il est nécessaire de localiser les régions d'où il provient.

Les enregistrements de bruit sismique entre 5 et 50s de période, sont dominés par des tempêtes brèves et énergiques. Notre objectif étant qu'un maximum de sources différentes contribuent aux corrélations afin que la fonction de Green puisse émerger, nous normalisons l'amplitude des signaux avant la corrélation en les recodant sur 1 bit (*Larose et al.* (2004b)). Ceci consiste à filtrer les enregistrements sur une bande de période relativement étroite (5-10s ou 10-20s dans notre cas) puis de diviser les signaux par leurs valeurs absolues de façon à ce qu'ils ne puissent prendre que deux valeurs : -1 ou +1. De cette manière nous donnons moins de poids aux évènements forts (tempête), et laissons les sources de faibles énergie contribuer aux corrélations. Cette normalisation permet en pratique d'améliorer la convergence des corrélations vers la fonction de Green du milieu.

Ainsi lorsque nous étudions l'origine du bruit de fond, nous devons tenir compte de cette normalisation : nous ne souhaitons pas étudier l'origine du bruit de fond "réel", mais l'origine du bruit de fond dont l'amplitude a été normalisé. Pour ce faire le meilleur moyen est de se servir des corrélations elles mêmes. En effet l'amplitude de la corrélation entre 2 stations aux temps d'arrivée des ondes de surface, dépend de l'énergie du bruit se propageant entre les deux stations. En étudiant l'amplitude des corrélations en fonction de l'azimut nous pouvons donc déterminer de quelles directions provient le bruit sismique.

Dans le présent article, nous testons cette méthode tout d'abord en Californie. En corrélant un an d'enregistrements semaine par semaine entre 253 couples de stations, nous montrons qu'entre 5 et 10s, le bruit provient de la côte tout au long de l'année. Au contraire entre 10 et 20s, des variations saisonnières ont lieu : en été le bruit provient du Sud-Ouest, tandis qu'en hiver il vient du Nord-Ouest et du Nord-Est.

En appliquant la même méthode en Europe, sur la côte Est et Ouest des Etats-Unis ainsi qu'en Tanzanie, nous montrons qu'au premier ordre entre 10 et 20s tous les réseaux enregistrent du bruit provenant des mêmes sources, et perçoivent les mêmes

variations saisonnières. Le bruit sismique provient des océans de l'hémisphère nord en hiver, et de l'océan Indien et du Pacifique Sud en été. Cette variation saisonnière est corrélée avec les changements saisonniers de la hauteur moyenne des vagues.

5.2 abstract

We study the origin of the background seismic noise averaged over long time by cross-correlating of the vertical component of motion, which were first normalized by 1-bit coding. We use one year of recording at several stations of networks located in North-America, western Europe and Tanzania. We measure normalized amplitudes of Rayleigh waves reconstructed from correlation for all available station to station paths within the networks for positive and negative correlation times to determine the seasonally averaged azimuthal distribution of normalized background energy flow (NBEF) through the networks. We perform the analysis for the two spectral bands corresponding to the primary (10-20s) and secondary (5-10s) microseism and also for the 20-40s band. The direction of the NBEF for the strongest spectral peak between 5 and 10 s is found to be very stable in time with signal mostly coming from the coastline, confirming that the secondary microseism is generated by the non-linear interaction of the ocean swell with the coast. At the same time, the NBEF in the band of the primary microseism (10-20 s) has a very clear seasonal variability very similar to the behavior of the long-period (20-40 s) noise. This suggests that, contrary to the secondary microseism, the primary microseism is not produced by a direct effect of the swell incident on coastlines but rather by the same process that generates the longer period noise. By simultaneously analyzing networks in California, Eastern US, Europe, and Tanzania we are able to identify main source regions of the 10-20 s noise. They are located in the northern Atlantic and in the northern Pacific during the winter and in the Indian ocean and in southern Pacific during the summer. These distribution of sources share a great similarity with the map of average ocean wave height map obtained by TOPEX-POSEIDON. This suggests that the seismic noise for periods larger than 10 s is clearly related to ocean wave activity in deep water. The mechanism of its generation is likely to be similar to the one proposed for larger periods, namely infragravity ocean waves.

5.3 Introduction

It has been recently demonstrated that the time cross-correlation function of random seismic wavefields such as seismic coda (*Campillo and Paul* (2003)) or seismic noise (*Shapiro and Campillo* (2004)) computed between a pair of distant stations contains, at least partially, the actual Green function between the two stations (*Cam-*

pillo (2006)). This provides us with a possibility to retrieve the propagation properties of deterministic seismic waves along long paths by analysing microseisms only. The emergence of the Green function is effective only after a sufficient averaging. In the case of diffuse coda waves, the averaging is performed over a set of earthquakes (*Campillo and Paul* (2003), *Paul et al.* (2005)). With the seismic noise (in the following, we use the term noise for the microseism which actually have no relation with instrumental noise), it is assumed that the averaging is provided by randomization of the noise sources when considering long time series (*Shapiro and Campillo* (2004); *Sabra et al.* (2005c)). Another important process contributing to the randomization is the scattering of seismic waves on heterogeneities within the Earth that is significantly strong at periods less than 40 s. Reconstruction of Rayleigh waves from the seismic noise is sufficiently efficient and accurate to lead to high resolution imaging at the regional scale (*Shapiro et al.* (2005); *Sabra et al.* (2005a)). Further optimization of seismic imaging based on noise correlation requires better understanding of the origin of the seismic noise and of the spatial and temporal distribution of its sources (*Pedersen et al.* (2006), *Schulte-Pelkum et al.* (2004)). In particular, it is important to establish conditions under which the noise can be considered as well randomized. To be more precise, a perfect randomization is not necessary but at least a distribution of sources covering a sufficiently large surface is required when integrating over time.

Ambient seismic noise is mostly made of surface waves (e.g. *Friedrich et al.* (1998), *Ekström* (2001)). Therefore, its sources are likely close to the Earth's surface. Observed noise amplitudes cannot be explained by the background seismicity (*Tanimoto and Um* (1999)) and main noise sources are believed to be loads caused by pressure perturbations in the atmosphere and the ocean. Moreover, the mechanisms of generation of seismic noise are not the same in different period bands. At relatively short periods (< 20 s), the two strongest peaks of the seismic noise, i.e. the primary and the secondary microseisms, are believed to be related to the interaction of the sea waves with the coast (*Gutenberg* (1951)). The primary microseism has periods similar to the main swell (10-20 s), while the secondary microseism that is the strongest peak in the noise spectrum originates from the non-linear interaction between direct and reflected swell waves that results in half period (5-10 s) pressure variations (*Longuet-Higgins* (1950)). This interaction results in variations of pressure at the sea bottom that do not exhibit the rapid exponential decay with depth expected for primary gravity waves.

The long period noise or "the hum" has been shown to exhibit a spectra corresponding to the normal modes of the Earth (*Nawa et al.* (1998); *Suda et al.* (1998); *Tanimoto et al.* (1998); *Roult and Crawford* (2000); *Kobayashi and Nishida* (1998); *Nishida et al.* (2000)). The origin of the long periods has been attributed to the so called infragravity waves, a ocean wave mode that exists at long period and which has been studied for its role in sediment transport in coastal zone. According to *Webb et al.* (1991) infragravity waves propagate in free waters, and result in long period pressure fluctuations at the ocean bottom. For long period noise, *Tanimoto* (2005) ruled out the

effect of atmospheric pressure variations since it was observed by *Watada et al.* (2001) to be much smaller than pressure at the ocean bottom for periods larger than 70s. *Rhie and Romanowicz* (2004) and *Tanimoto* (2005) proposed the infragravity waves as the source of the long period noise. Observations at an ocean bottom broadband station (*Dolenc et al.* (2005)) show a strong link between infragravity waves and the local level of excitation of shorter period ocean waves. This suggests a local generation of the long period infragravity waves from the primary ocean swell. *Dolenc et al.* (2005) also observed a correlation of the amplitude of the infragravity waves with tides, a point that could be related to the interaction of waves and currents (see *Longuet-Higgings and Stewart* (1964), *Kobayashi and Nishida* (1998), *Nishida et al.* (2000)). Noise excitation also exhibits strong seasonal variations. Using array analysis, *Rhie and Romanowicz* (2004) have shown that sources of the long period (150-500s) seismic noise are dominantly located in the Northern hemisphere oceans during the northern winter and migrate to the southern ocean during the southern winter. This behavior is well correlated with the seasonal variation of the amplitudes of ocean waves suggesting that the "hum" is produced by some sort of atmosphere-ocean-seafloor coupling.

In the present paper, we study the origin and the seasonal variability of the relatively short period noise (between 5 and 40s) with a particular emphasis on the primary microseism (10-20 s band). One of our main motivations is that a better understanding of the distribution of noise source in space in time is needed for optimization of the noise-based seismic tomography. Using several networks in North America, Africa, and Europe, we determine the direction of the average azimuthal distribution of normalized background energy flow (NBEF) across each array by measuring the degree of symmetry of time cross-correlations computed between pairs of stations and locate the apparent noise sources.

Results of our analysis show that while the sources of the secondary microseism remain stable in time, the sources of the primary microseism exhibit strong variability very similar to long period noise (hum) and well correlated with sea wave conditions.

5.4 Asymmetry of Cross Correlation

The idea of using random noise to reconstruct the Green function has already been applied successfully in various fields of physics such as helioseismology (e.g. *Duvall et al.* (1993); *Gilles et al.* (1997)), acoustics (*Weaver and Lobkis* (2001)), or oceanography (*Roux and Kuperman* (2004)). In seismology, *Aki* (1957) already proposed to use the noise to retrieve the dispersion properties of the subsoil. *Shapiro and Campillo* (2004) reconstructed the surface wave part of the Green function by correlating seismic noise at stations separated by distance of hundreds to thousands of kilometers, and measured their dispersion curves at periods ranging from 5 to about 150 seconds. Later this method has been used for seismic imaging in California (*Shapiro*

et al. (2005)). In the case of a spatially homogeneous distribution of noise sources, the cross-correlation is expected to be nearly symmetric in amplitude and in arrival time with its positive and negative parts corresponding to the Green function of the medium and its anticausal counterpart, respectively (e.g. *Lobkis and Weaver* (2001a) ; *van Tiggelen* (2003) ; *Snieder* (2004) ; *Sánchez-Sesma and Campillo* (2006)). In practice, as we will see below, the causal and anticausal parts of the cross-correlation may strongly differ in amplitude. This amplitude factor depends directly on the energy flux of the waves traveling from one station to the other (van *van Tiggelen* (2003), *Paul et al.* (2005)). In others words, in the case of a perfectly isotropic distribution of sources, the energy flux between two stations is the same in both directions and the resulting cross-correlation between these stations is symmetric (Figure 5.2a). On the other hand, if the density of sources is larger on one side than on the other, the amounts of energy propagating in both directions are different. In this case, the resulting cross-correlation is not symmetric anymore in amplitude (although the arrival time remains the same) (Figure 5.2b). An important consequence is that the asymmetry of the cross correlation computed between several pairs of stations of a network can be used to measure the main direction of the energy flux across the array. Making such measurements at different arrays will allow us to determine the location of main sources of the seismic noise.

5.5 Origin of Seismic Noise Observed in California

We firstly consider one pair of stations in California (MLAC and PHL, fig :5.3a). We analyze one year (2003) of continuous vertical records. Before computing cross-correlations, records are corrected from the instrumental response and bandpassed within different bandwidths. To reduce the contribution of the most energetic arrivals, we disregard completely the amplitude and consider 1-bit signals only (*Derode et al.* (1999) ; *Campillo and Paul* (2003) ; *Shapiro and Campillo* (2004)). Figure 5.3 shows the cross-correlations of different months of records bandpassed between 5 and 10 s, i.e. around the secondary microseism. Positive time delay indicates waves propagating from MLAC to PHL, whereas negative time indicates waves propagating from PHL to MLAC. In this period range, the form of cross-correlations is very stable in time and very asymmetric. The amplitude of the anticausal part of the cross-correlations is much larger than the one of the causal part. The main arrival is the fundamental Rayleigh wave. The Green function is poorly reconstructed in the causal part. This indicates that most of the noise is propagating from PHL to MLAC, i.e. from the coastline to the continent. This confirms that at periods between 5 and 10s most of the noise is dominated by waves generated by nonlinear interaction between the swell and the coast line.

The behavior is very different when considering periods between 10 and 20s (Figure

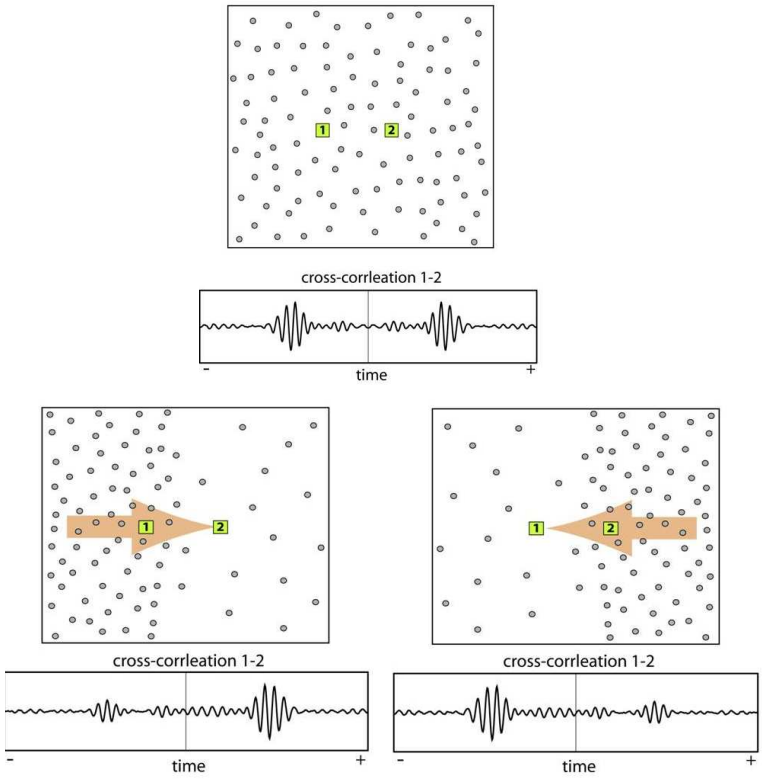

FIG. 5.2: Schematic illustration of the effect of inhomogeneous noise sources distribution on the degree of symmetry of cross-correlation. a) If the sources of noise are evenly distributed, the cross-correlation of 1 and 2 is symmetric. b) In the case of a non-isotropic distribution of sources, the cross-correlation between 1 and 2 is not symmetric in amplitude anymore, though it is in arrival time.

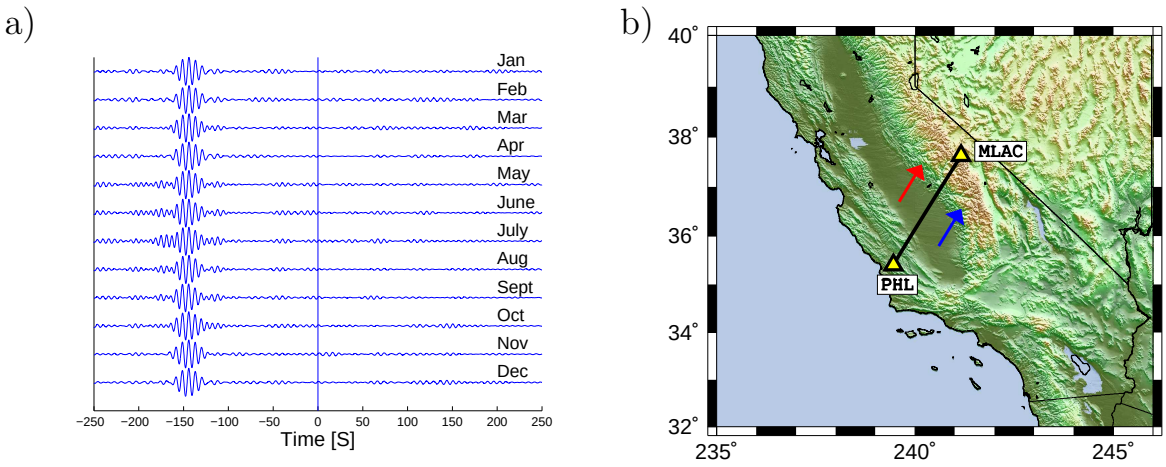

FIG. 5.3: (a) Cross correlation between 5 and 10 seconds of one year (2002) of noise recorded on MLAC and PHL and stacked month per month. The interstation distance is 290 km. (b) Map showing locations of the two stations. Apparent directions of the NBEF during winter and summer are shown with black and white arrows, respectively.

5.4). The cross-correlations in this band exhibit a clear seasonal variation. During the northern winter (October to March), the amplitude of the causal part of the correlation is larger than the amplitude of the anticausal part. This indicates that most of the Rayleigh wave energy propagates from MLAC to PHL (NE to SW). During the northern summer (May-September), the opposite is observed : the noise is dominated by waves propagating from PHL to MLAC (SW to NE). Moreover, during the whole year, the Rayleigh waves are visible both at positive and negative times. All this shows that, in the period band of the primary microseism, an important contribution of the noise observed in California is coming from the east, having likely its source in the Atlantic Ocean. The waveforms observed at positive and negative times are not exactly identical because of the differences in the spectrum of the noise coming from east or west.

To determine the main direction of the normalized background energy flow (NBEF) we used 23 stations located in Southern California separated by distances of a few hundreds kilometers (Figure 5.5) . We kept only paths longer than 120 km (two wavelengths at 20 s) and shorter than 450 Km. This resulted in 136 paths or 272 azimuths when using both the causal and the anticausal parts.

Using the procedure described above, we computed cross-correlations of continuous vertical records for each of the 136 paths during the year 2003. We considered three period bands : 5-10s, 10-20s, and 20-40s. For the first two period bands, cross correlations were stacked in a moving window of 15 days. For each stack, amplitudes of the causal and anticausal parts were determined by taking the maximum of their envelopes in a time window corresponding to the Rayleigh wave group velocity. We

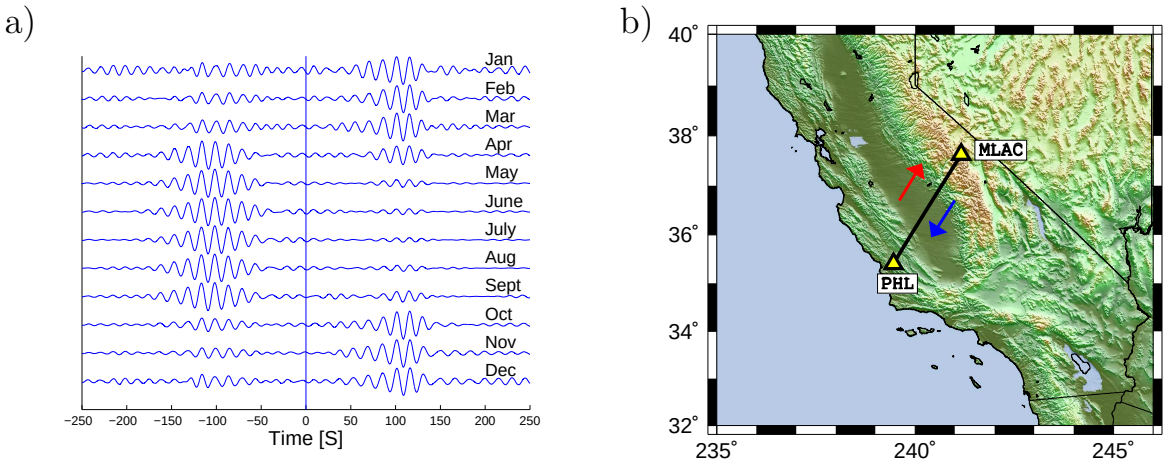

FIG. 5.4: Same as Figure 2 but for the period range between 10 and 20 s.

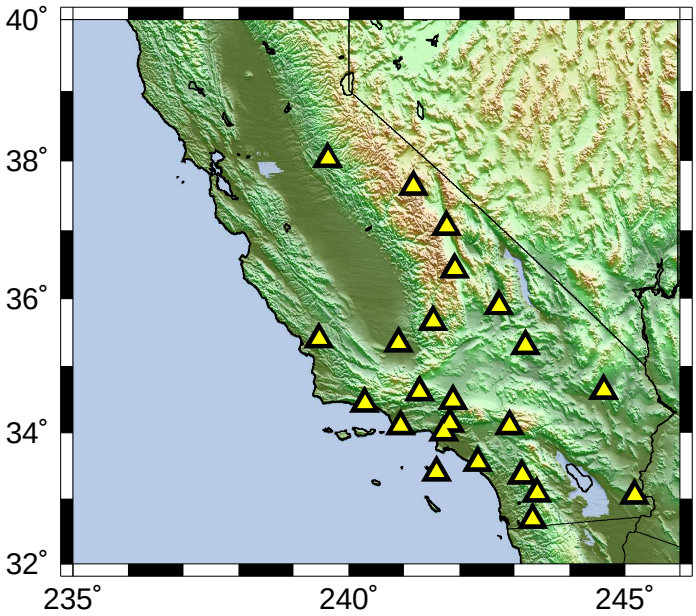

FIG. 5.5: Location of seismic stations used in the network analysis in California.

correct our measurement from the geometrical attenuation of the Rayleigh wave with distance, by multiplying the amplitude by the square root of the inter-station distance. This way, we measured normalized amplitudes of seismic noise for two azimuths from each cross-correlation. Combining measurements from all stations pairs we obtain the distribution of the normalized amplitude with respect to azimuth.

Maxima of this distribution indicate main directions of NBEF across the array. Seasonal variation of the normalized amplitude and the direction of the NBEF during the year 2003 are illustrated in Figure 5.6a-b. Amplitudes were normalized between 0 and 1 for the entire set of azimuths. One must remark that these azimuthal distributions were computed after 1-bit normalization. This means that high amplitude events, likely associated with the strongest storms are down weighted by our processing. The plots of Figure 5 are not directly characteristic of the actual absolute noise energy but of the time averaged normalized energy. Note that it is the relevant measure for anlysing the noise in the context of Green function reconstruction using the procedure initiated by Shapiro and Campillo (2004). This procedure can be applied to networks with spatial distribution of station which are not suitable for F-K analysis.

Between 5 and 10s, the main direction of the NBEF remains constant over the whole year similar to the observation made for the path MLAC-PHL. Most of the noise is coming from a range of azimuth going from 200° to 225° (SW) confirming that, in this period band, most of the seismic noise is caused by the secondary microseism locally generated by ocean waves along the coastline.

The noise behavior is very different in the period range of the primary microseism (10-20 s) where the NBEF exhibits a very strong and sharp seasonal variation (Figure 5.6 c-d). Its main direction remains around 220° 225° (S-SW) during the summer. However during the winter, most of the noise is coming from the north with two clear preferential directions : 315° and 45°. The change between these two main regimes is very rapid and takes place in March and October.

This difference between the directions of NBEF of the primary and secondary microseisms is surprising because it indicates that the two main spectral noise peaks observed locally do not have the same region of origin. This could be the result of the attenuation of the seismic waves which is stronger for shorter periods and cancels the contributions of distant sources in the 5-10s period band. Another explanation could be that the actual regions of generation of the seismic noise is different in the different period bands. This hypothesis is supported by the observation that the azimuthal distribution is dominated in winter by a flux from azimuths between 180 and 225° for the period band 5-10 s while there is no significant contribution from this directions for the period band 10 to 20 s. Before exploring further the origin of noise in the primary microseism band (10-20s), let us consider longer period, i.e. the 20-40s period band.

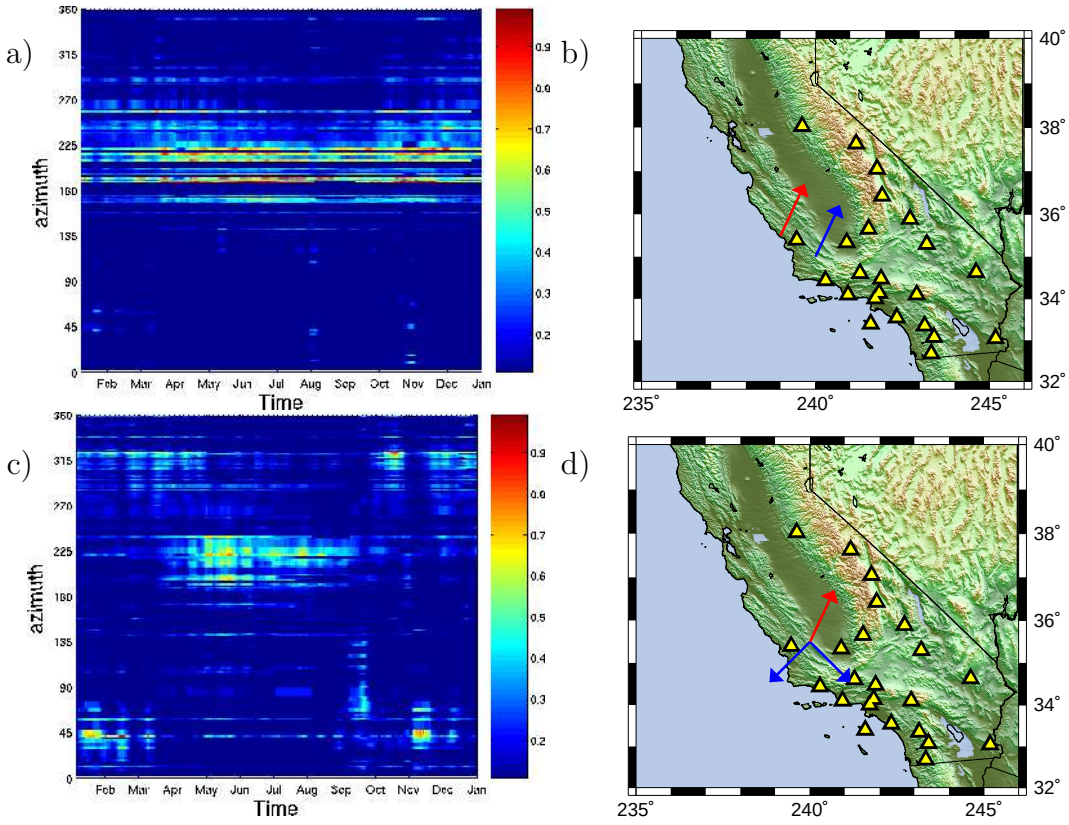

FIG. 5.6: (a) Normalized amplitude of the cross-correlation of seismic noise at periods between 5 and 10 s as a function of time and azimuth determined from the network analysis in California. (b) Location map of the used stations. Main directions of the NBEF during winter and summer are shown with black and white arrows, respectively. (c) and (d) Same as (a) and (b) at periods between 10 and 20 s.

At longer periods, there is less scattering and we expect the ambient seismic noise to be less diffuse. Therefore, the reconstruction of Green functions requires averaging over longer time series. For this reason, we do not consider anymore 15 days moving windows but analyze longer time series by cross-correlating noise recorded either during the winter (October to March) or the summer (April to September). For these two periods, we measure normalized amplitudes of the Rayleigh wave part of the Green function for the set of station pairs. Figure 5.7 shows the azimuthal distribution of the normalized amplitude of the correlation versus azimuth for the three different period bands (5-10s, 10-20s, 20-40s) during the winter (left column) and the summer (right column) of 2003.

While at periods between 5 and 10 s most of the noise is coming from the coast during the whole year, the noise provenance has a clear seasonal variability at longer periods. Moreover, the normalized amplitude vs azimuth diagrams for the 10-20s and 20-40s period bands exhibit main features which are similar, although not completely identical. Most of the background noise energy is coming from the North-East (possibly North Atlantic) during the winter and the main direction switches to the South-West during the summer. This similarity suggests that the average primary microseism may originate from the same regions as the longer period noise, which has been considered to be excited by the infragravity ocean waves propagating away from the coast (*Webb et al.* (1991), *Rhie and Romanowicz* (2004), *Tanimoto* (2005)). We will investigate further the origin of the noise in the band of the primary microseism by considering simultaneously several networks.

5.6 Origin of the 10-20 s Noise

Using the method described in the previous section, we analyzed the noise in several others regions of the world : East coast of USA, Western Europe, and Tanzania (Figure 5.8). Similar to the Californian network, our analysis is based on the amplitudes of the reconstructed causal and anticausal Rayleigh waves. The data for the northern hemisphere are from 2003 and the Tanzanian data are from 1994-1995, the period of the 97-005 Passcal experiment (*Owens et al.* (1997)). For each of these networks we estimated the normalized noise amplitudes as functions of azimuth during the winter (October to March) and the summer (April to September) for the period bands of the primary and the secondary microseisms. Similar to the observations in California, the NBEF of the 5-10 s noise remains stable over the whole year at all networks. This observation is compatible with the idea that the generation of the secondary microseism is mostly controlled by the bathymetry and the geometry of the coastlines. The noise in this period is dominated by the activity in a region close to the station since the absorption limits the contribution of distant source zones. It explains the stability of the distribution during the year.

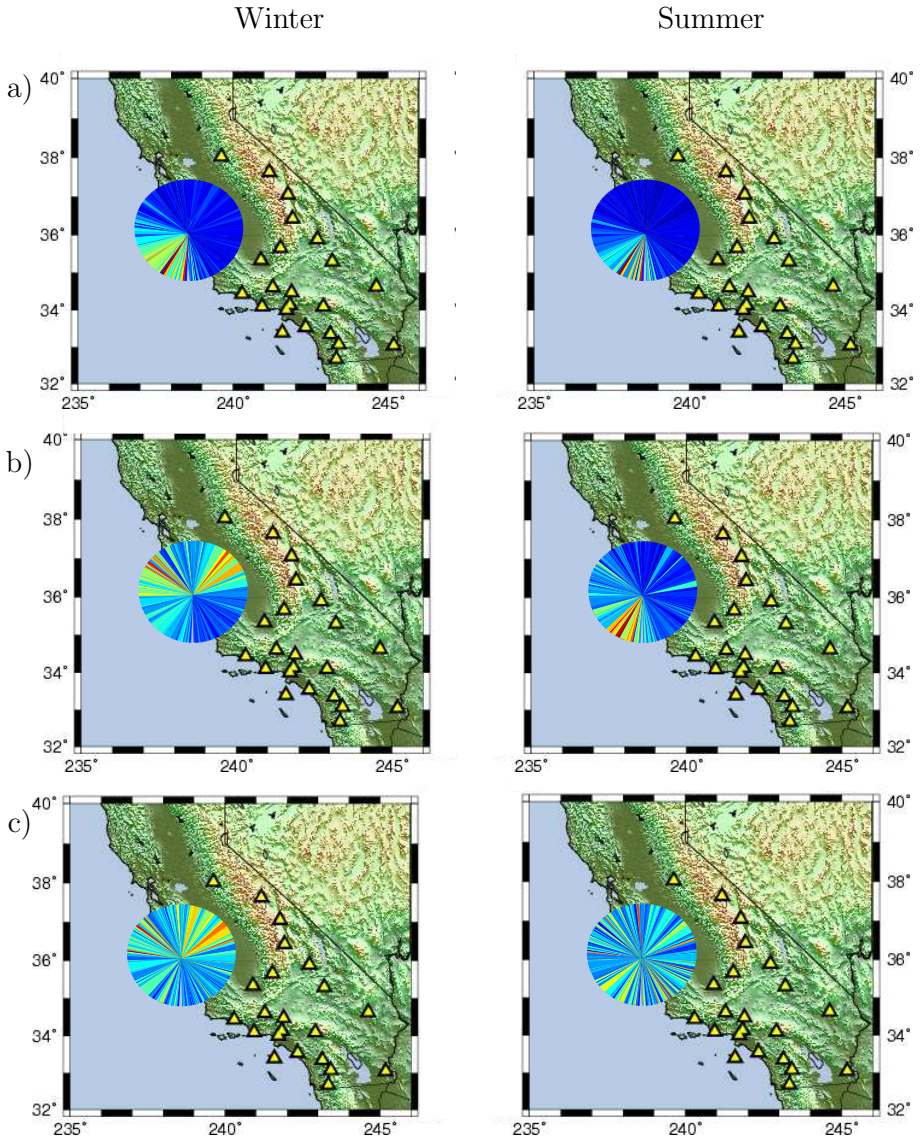

FIG. 5.7: Normalized amplitude of the cross correlation averaged during the winter (left column) and the summer (right column) versus azimuth for various frequency bands a) 5-10s b) 10-20s c) 20-40s. The color scale is the same as on Figure 5.6

.

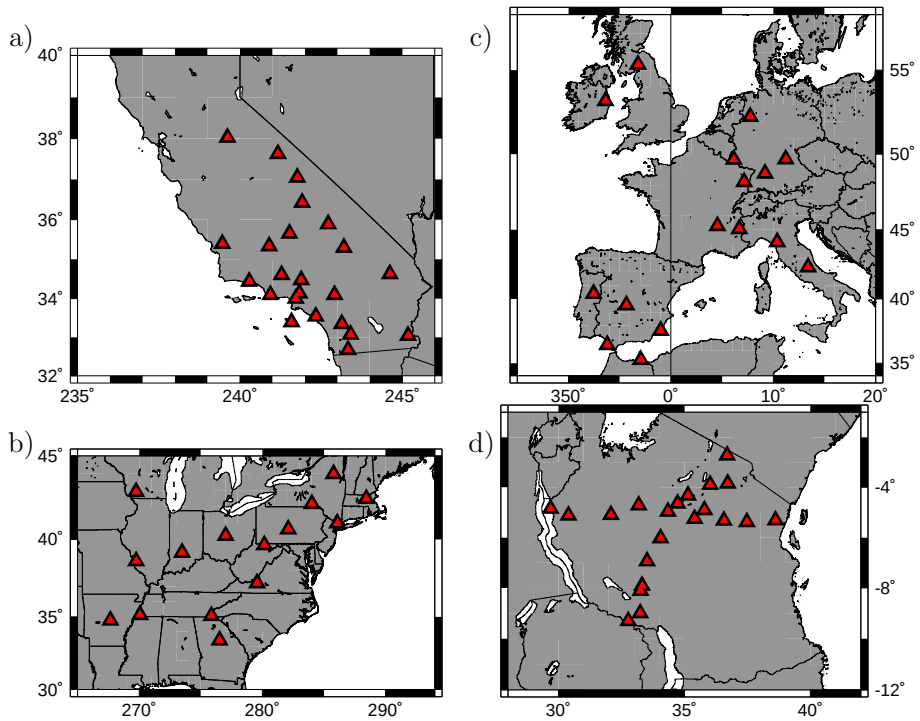

FIG. 5.8: Networks of broadband stations used a) in California (2003), b) in the east coast of USA (2003), c) Western EU (2003), d) Tanzania (1994-1995). All the data are available from the IRIS data center.

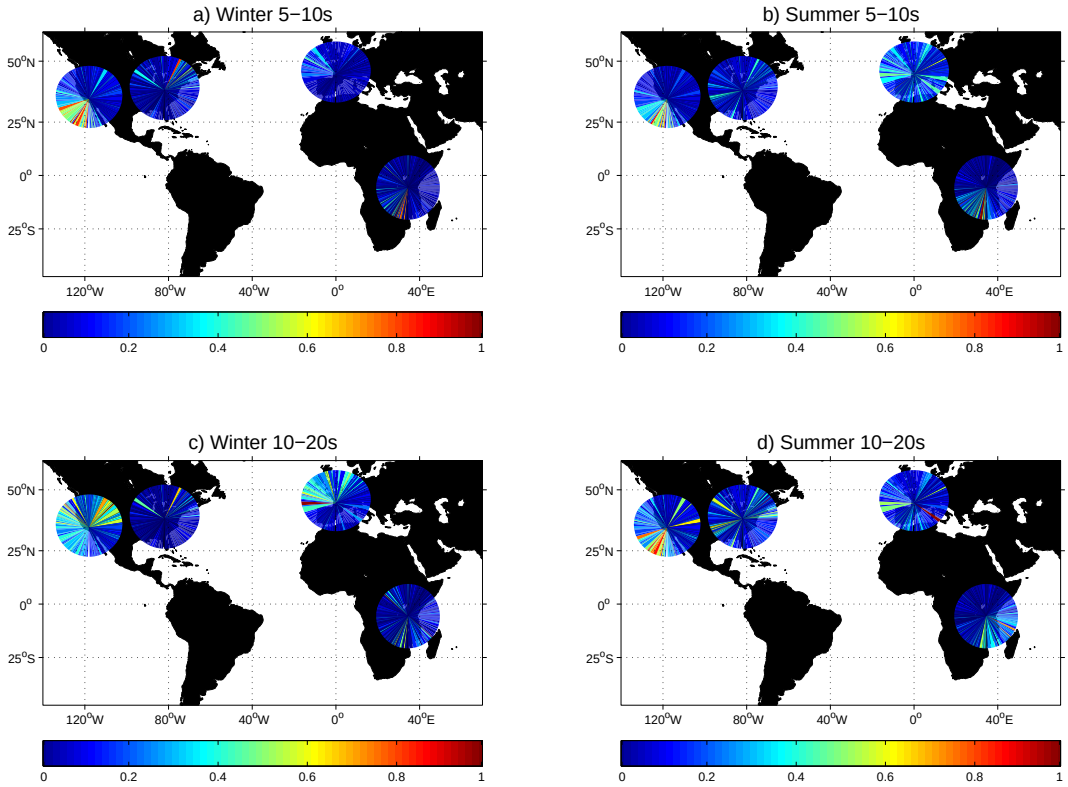

FIG. 5.9: Average normalized amplitude of cross-correlations of noise versus azimuth, for various network a) During winter between 5-10 s b) Summer 5-10s c) Winter 10-20s d) Summer 10-20s.

The behavior of the 10-20 s noise is very different. Indeed the effect of attenuation is weaker for longer periods and sources at the global scale are contributing. In this period band, the regions where the noise is originating are different during the summer and the winter. A first order observation from Figure 5.9 is that the major part of the noise seems to come from the North during winter, and from the South during the summer.

In spite of their limited number, the considered networks illuminate a large part of the Earth surface. In the following, we use them for a rough identification of the source regions that generate the 10-20 s noise consistently recorded by the four networks. We use a simple back projection procedure. For every considered pair of stations of a given network, we trace the great circle connecting the stations and divide it in two equal parts corresponding to two opposite directions of wave propagation between the stations. Normalized amplitudes measured from positive and negative parts of the cross-correlation computed between these stations are attributed to the corresponding half great circle. This is an approximation since in the 10-20s period band the path followed by Rayleigh waves is not exactly a great circle because of the lateral heterogenity of the crust and the mantle. We then define a $2° \times 2°$ grid on the

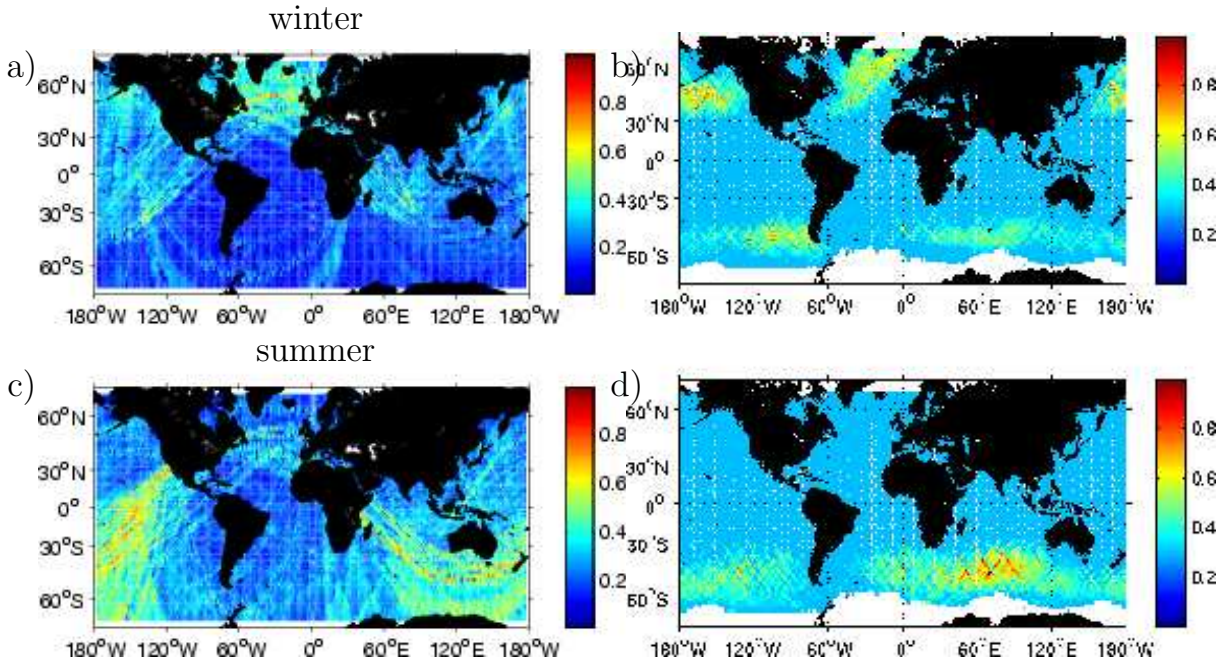

FIG. 5.10: Comparison between seasonal variations of the location of sesimic noise sources and significant wave height. (a) and (c) : geographical distribution of the mean back-projected normalized amplitude of the 10-20 s noise cross-correlations (see text for detailed explanation of the back-projection) during the winter and the summer. (b) and (d) : Global distribution of the square of wave height measured by TOPEX/Poseidon during the winter and the summer.

surface of the Earth and take the mean value of the normalized correlation amplitude associated with all great circles crossing every cell. To be able to use all four networks simultaneously, we assume that the seasonal noise variability is stable over different years and combine the 2003 data from the northern hemisphere with the 1994 data from Tanzania (results for individual networks are given in Appendix).

The results for the four networks in the 10-20 s band are presented in Figure 5.10. During the northern hemisphere winter, the observed average noise is apparently dominated by a source zone in the northern Atlantic ocean. Two weaker sources are visible in the northern Pacific, one close to Alaska and the other close to Japan. During the northern hemisphere summer, most of the noise originates from the southern Indian ocean and the southern Pacific. It has to be noted that the resolution of these patterns is limited by the small number of networks. An example is the band in the Pacific Ocean which is due to the fact that the source zone, the California, eastern US and western Europe networks are on the same great circle. In spite of the limited resolution, these results clearly show that, contrary to the secondary microseism, the 10-20 s noise is not generated locally but is excited by sources acting at the global scale and having a clear seasonal variability. An attempt to locate

these sources suggests they have to be searched in the central parts of the oceans, although with our limited resolution we cannot exclude that a part is generated on the coast or in shallow water areas. Specifically, with the form of normalization and averaging used here, we do not contradict the observation that the arrival of strong storms along the coasts is associated with high amplitude microseisms. The hypothesis that the average background noise energy originates in the zones of storm activity is confirmed by strong similarities between the maps of the apparent sources of the 10-20 s seismic noise and the global wave height maps obtained from the radar altimeter data collected by the satellite TOPEX-POSEIDON (Figure 5.10). Both maps show clear seasonal variations with maxima located in deep oceans in the southern and the northern hemispheres during the summer and the winter, respectively. A similar seasonal variability was recently reported for the very long period (> 150 s) Earth hum (*Rhie and Romanowicz* (2004)).

5.7 Conclusions

Our results clearly demonstrate that the origins of the primary and the secondary microseisms are different. Sources of the secondary microseism are stable in time and likely associated with coastlines, confirming that this part of the seismic noise is generated by the nonlinear interaction of the ocean swell with the coast. In the same time, the primary microseism exhibits a very clear seasonal variability very similar to the behavior of the long-period noise suggesting that the seismic noise for periods larger than 10 s is produced by a single mechanism not directly related to the action of the swell on the coast. This hypothesis is also favored by the good correlation between the distributions of the seismic noise sources determined from the network analysis with the maps of average ocean wave height map obtained by TOPEX-POSEIDON.

This seasonal variation also means that the quality of the Green function reconstruction by cross-correlation can be different with noise recorded during the summer and during the winter. Using simultanelously data recorded during the winter and the summer would be a way to increase the number of high-quality measurements and to improve the resolution of seismic imaging based on noise cross-correlation.

The long period seismic noise is likely produced by the infragravity waves (*Webb et al.* (1991), *Rhie and Romanowicz* (2004), *Tanimoto* (2005)). According to *Webb et al.* (1991), long period gravity waves propagate freely away from the coast lines. Recent observations indicate that the spectrum of this class of waves can be extended to relatively short periods ($\sim$20 s) (*Dolenc et al.* (2005)). Following *Longuet-Higgins* (1950), bottom pressure fluctuations arise from the interaction of swells propagating in opposite directions. Although the most commonly considered configuration to encounter such a system of waves involves the reflection of the swell from the coast, it can also be generated in the area of strong storm activity even in deep oceans.

Others sources of pressure fluctuations in deep water can be associated with the interaction of propagating swell of slightly different frequencies with high amplitude currents (*Longuet-Higgings and Stewart* (1964)). These kinds of mechanisms of generation are compatible with the location of background noise source regions in the zones of highest sea waves.

5.8 Appendix

Figures 5.11 and 5.12 show the apparent origin of the background noise seen by the different networks in winter and summer respectively. The California network is the denser and is therefore the most favorable for the reconstruction of the Rayleigh waves. In order to test the importance of the California network in the maps of Figure 5.10, we present the same map computed without including it. The resulting maps (Figure 5.8) indicate that the maps built with or without the California network share the

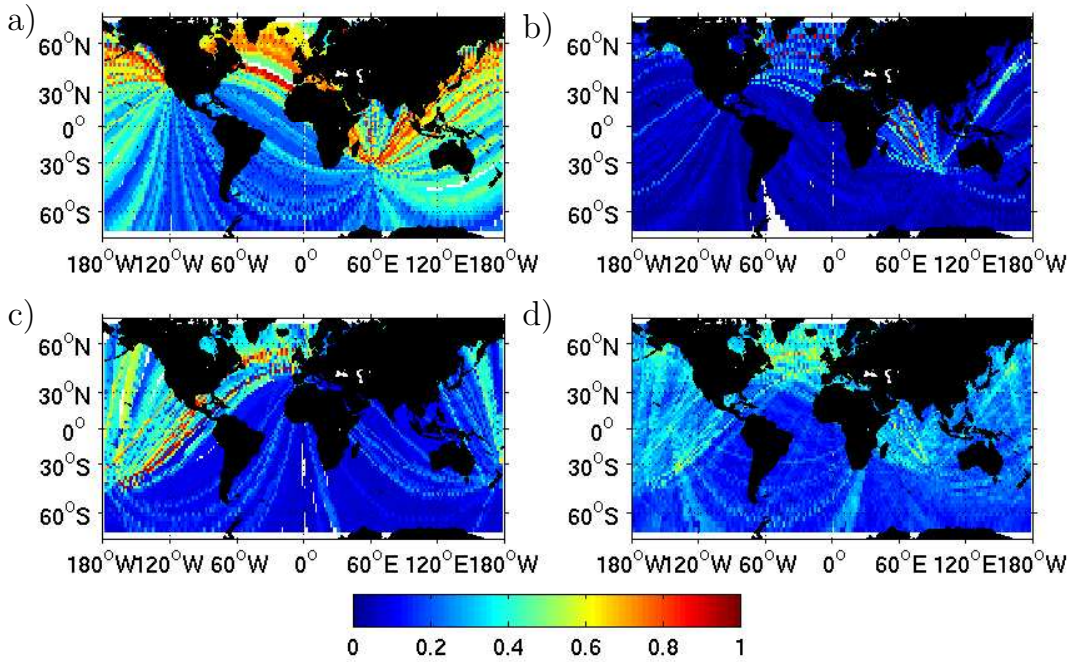

FIG. 5.11: Origin of the background noise at 10-20 seconds sensed during the winter by the different networks a) California b) East coast of the USA c) Western Europe d) Tanzania

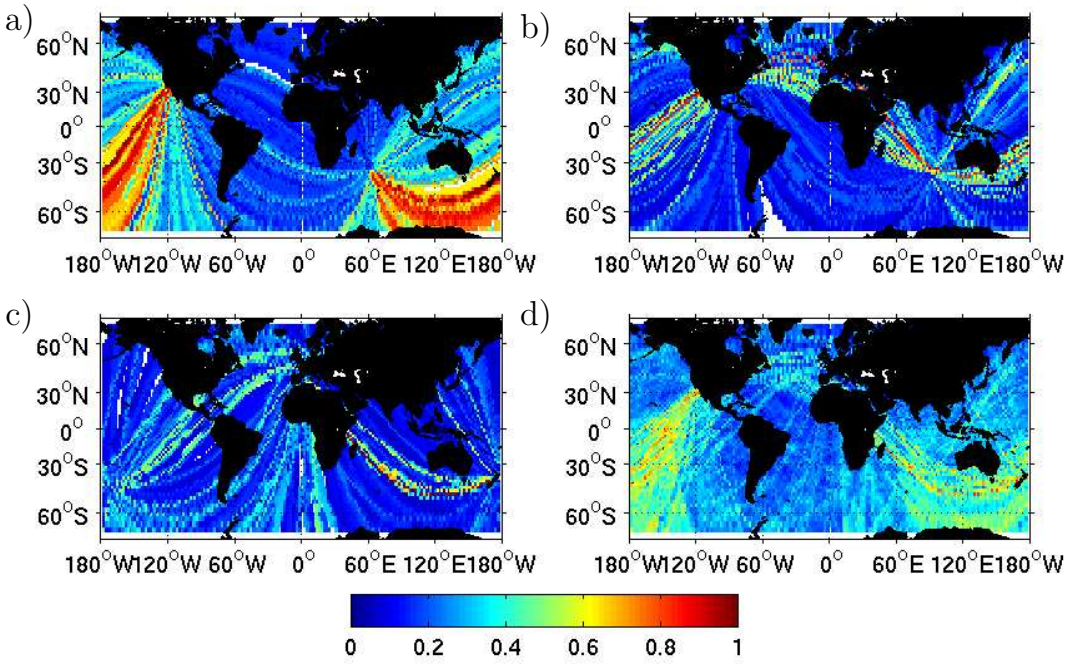

FIG. 5.12: Origin of the background noise at 10-20 seconds sensed during the summer by the different networks a) California b) East coast of the USA c) Western Europe d) Tanzania

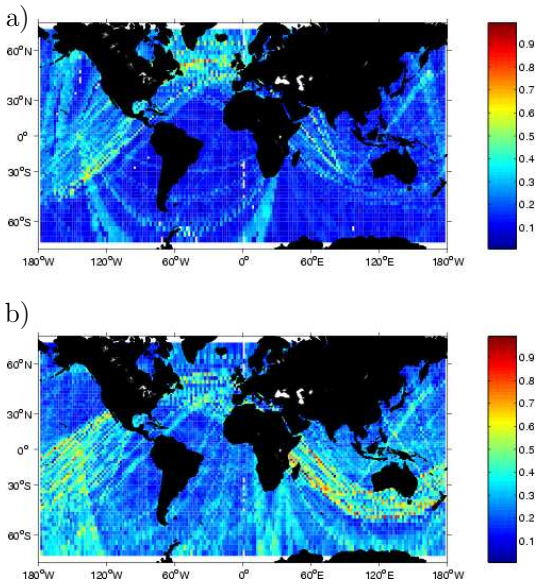

FIG. 5.13: Localization of the background noise origin at 10-20s without using the californian network a) during the winter b) during the summer.

5.9 acknowledgments

All the seismic data used in this study have been obtained at the IRIS DMC (http ://www.iris.edu/) and include GSN, GEOSCOPE, GEOFON, Southern California Seismic Network, Berkeley Digital Seismic Network, and Tanzania PASSCAL seismic experiment. We are grateful to all scientists and technical staff who provided the data. The ocean wave height map were obtained from the Physical Oceanography Distributed Active Archive Center (PO.DAAC, http ://podaac.jpl.nasa.gov/). This research has been supported by contract DE-FC52-05NA26607 from the National Nuclear Security Administration, by the National Science Foundation grant EAR0450082, by CNRS/Institut National des Sciences de l'Univers (program DyETI), and by the Commissariat à l'Energie Atomique.

Troisième partie

Stabilité des fonctions de Green reconstruites par corrélation de bruit de fond

Chapitre 6

Travel time measurements from noise correlation : stability and detection of instrumental time shifts

L. Stehly, M. Campillo, N.M. Shapiro
Publié dans *Geophysical Journal International* (2007)

Sommaire

6.1 Résumé

Dans le chapitre précédent nous avons étudié l'origine du bruit de fond microsismique. Le but était de savoir si la distribution des sources garantissait ou non que les corrélations de bruit convergeaient vers la fonction de Green du milieu. Le résultat est que nous sommes dans une situation "intermédiaire", ni parfaite ni désespérée : au sein d'un même réseau le flux d'énergie n'est pas isotrope comme on l'aurait souhaité, certaines directions sont privilégiées. Ceci est particulièrement vrai entre 5 et 10s de période où l'essentiel du bruit enregistré en Californie provient de la côte le long de l'océan pacifique. Entre 10 et 20s la situation est intéressante. Le bruit est généré dans l'hémisphère nord en hiver, et dans l'hémisphère sud en été. Ainsi moyenné sur un an, le bruit provient d'une large gamme d'azimuts sans qu'il soit complètement isotrope. Si la distribution des sources n'est pas idéale, elle n'est pas non plus trop éloignée des exigences de la théorie.

Il est donc nécessaire d'étudier la précision des mesures de vitesse des ondes de surface effectuées grâce aux corrélations de bruit. Deux questions sont ici posées : 1) Les mesures de vitesse sont-elles suffisamment fiables pour que les corrélations puissent être utilisées pour faire de la tomographie ? 2) Est-il possible d'utiliser les corrélations pour étudier des variations physiques du milieu ? Cette question est particulièrement importante pour l'étude des changements pouvant intervenir sur des volcans avant une éruption, ou au niveau de failles sismiques à la suite d'un séisme par exemple.

Pour répondre à ces questions, nous nous servons de 3 stations - GSC, PAS et PFO - situées en Californie du Sud pour lesquelles nous disposons de 11 ans d'enregistrements continus de bruit répartis entre 1991 et 2005. La disposition des stations nous permet d'avoir à la fois des trajets "favorables" orientés perpendiculairement à la côte (GSC-PAS), et au contraire des trajets parallèles à la côte pour lesquels on s'attend à avoir des mesures de moins bonnes qualités (GSC-PFO). L'idée est de voir si la vitesse de propagation des ondes de surface que nous mesurons grâce aux corrélations change au cours du temps ou pas. Pour chacun des trajets, et pour les bandes de période 5-10s et 10-20s, nous définissons une fonction de Green de référence en corrélant 5 ans de données. Nous corrélons ensuite nos enregistrements mois par mois, et nous comparons la "fonction de Green du mois" avec la fonction de Green de référence.

Si nous mesurons la vitesse réelle du milieu, la mesure doit être stable au cours du temps. Si au contraire nos mesures fluctuent, nous pouvons identifier l'origine des fluctuations en nous servant de la symétrie des corrélations :

- Les fonctions de Green reconstruites dans les temps positifs et négatifs des corrélations sont sensibles à des sources de bruit situées dans des zones différentes, localisées de part et d'autre des stations. Ainsi des changements de position des sources se répercuteront indépendamment sur les temps positifs et négatifs des corrélations.

- Au contraire si le milieu de propagation change (au voisinage d'une faille à cause de la tectonique par exemple), les temps positifs et négatifs seront affectés simultanément : on mesurera des temps de propagation plus bref ou plus long à la fois sur les temps positifs et négatifs des corrélations.
- Des erreurs instrumentales telles que des problèmes d'horloge sur les stations auront un effet opposé sur les temps positifs et négatifs : les ondes "ralentiront" d'un coté de la corrélation, et "accélèreront" de l'autre.

Nos résultats laissent apparaître deux périodes de temps distinctes : entre 1999 et 2005 nous identifions ni erreur d'horloge, ni changement au sein du milieu. Les variations des temps d'arrivée des ondes de surface mesurées ont une périodicité de un an. Ce sont donc les variations saisonnières des sources du bruit que nous avons mis en évidence au chapitre précédent qui contribuent le plus aux changements de vitesse apparente que nous mesurons. Ces fluctuations ont toutefois une amplitude faible, toujours inférieure à 0.5s représentant moins de 0.3% du temps de propagation. Leurs variance est de l'ordre de 0.01s. Cette précision montre que les corrélations de bruit ont une précision largement suffisante pour faire de la tomographie.

Au contraire entre 1991 et 1996, de larges fluctuations sont présentes dans les données. Nous montrons qu'elles sont dues à des erreurs d'horloge interne des stations. Ces erreurs sont pour nous une bénédiction, elles nous permettent d'évaluer la précision avec laquelle nous pourrions identifier des variations physiques des temps d'arrivée des ondes de surface. Ainsi nous constatons que nous sommes capables de distinguer des erreurs d'horloge brèves dans le temps d'une amplitude d'une demi seconde, ou des décalages de l'ordre du dixième de seconde se produisant sur plusieurs années. Ce résultat est d'une très grande importance, car il indique également quelles sont les variations physiques du milieu que nous pourrions mettre en évidence en l'absence d'erreur d'horloge.

6.2 Abstract

We test the feasibility of using Green functions extracted from records of ambient seismic noise to monitor temporal changes in the Earth crust properties by repeated measurements at regional distances. We use about 11 years of continuous recordings to extract surface waves between three pairs of stations in California. The correlations are computed in a moving one-month window and we analyze the temporal evolution of measured inter-station travel times. The comparison of the arrival times in the positive and negative correlation time of Rayleigh and Love waves allows us to separate time shifts associated with any form of physical change in the medium, those resulting from clock drift or other instrumental errors, and those due to change in the localization of the noise sources. This separation is based on the principle of time symmetry. When

possible, we perform our analysis in two different period bands : 5-10 s and 10-20 s. The results indicate that significant instrumental time errors (0.5 s) are present in the data. These time shifts can be measured and tested by closure relation and finally corrected independantly of any velocity model. The travel time series show a periodic oscillation that we interpret as the signature of the seasonal variation of the region of origin of the seismic noise. Between 1999 and 2005, the final arrival time fluctuations have a variance of the order of 0.01s. This allows us to measure inter-station travel times with errors smaller than 0.3% of the inter-station travel time and smaller than 1% of the used wave period. This level of accuracy was not sufficient to detect clear physical variation of crustal velocity during the considered 11 years between the three stations in California. Such changes may be more easily detectable when considering pairs of stations more closely located to each other and in the vicinity of tectonically active faults or volcanoes.

6.3 Introduction

It has been recently shown that the time cross-correlation function of seismic ambient noise *Shapiro and Campillo* (2004) computed between a pair of distant stations contains, at least partially, the actual Green function between the two stations (see *Campillo* (2006), *Larose et al.* (2006b) and references therein). The emergence of the Green function is effective only after a sufficient averaging that is provided by random spatial distribution of the noise sources when considering long time series as well as the scattering of seismic waves on heterogeneities within the Earth crust (*Shapiro and Campillo* (2004), *Sabra et al.* (2005c)).

Travel time measurements of Rayleigh waves reconstructed from the seismic noise has been used to produce high resolution regional scale images of the crustal structure in California (*Shapiro et al.* (2005), *Sabra et al.* (2005a)). This region is characterized by strong contrasts in seismic velocities within the crust and, therefore, was a relatively easy task for the seismic imaging because the existing anomalies could be well imaged even when using relatively rough travel time measurements. However, further applications require a more careful analysis of the measurement errors. For example, Green functions extracted from records of ambient seismic noise can be used for monitoring temporal changes in the Earth crust properties by repeated measurements at regional distances. In this case, the noise-based measurements should be accurate enough to allow us to detect relatively small time shifts associated with the structural changes. Our goal here is to assess the accuracy of the Green function reconstructed by cross-correlation of ambient seismic noise and to determine to what extents the noise-based travel time measurements can be used to detect and to quantify station instrumental errors and to monitor changes in the physical properties of the medium.

High precision measurements of changes of medium properties are possible using re-

peated analysis of seismic records (e.g *Poupinet et al.* (1984), *Snieder* (2006)), or noise auto-correlation (*Wegler and Sens-Schonfelder* (2007)), but this technique cannot be used to detect phase shift associated with instrumental dysfunction.

We use 11 years of continuous records to extract the surface waves part of the Green function between 3 pairs of stations in California by computing cross correlations of ambient seismic noise in a moving one month window in the two period bands : 5-10 s and 10-20 s. We evaluate the apparent travel time fluctuations of the surface waves for both positive and negative cross-correlation times. The comparison of the travel times estimated from positive and negative time surface waves allows us to distinguish the fluctuations due to any form of physical change in the medium from time shifts resulting from clock drift or other instrumental errors and finally to estimate time errors caused by variations in the distribution of the noise sources.

After presenting data and methods in section 2, we present results of our analysis in section 3. First, we analyze travel time fluctuations measured during a period when no obvious instrumental problem occurred. Then, we consider a different time interval to determine what part of the observed time fluctuation is due to instrumental errors and, finally, we correct the data from the measured instrumental errors.

6.4 Data and methods

Our goal is to study the evolution of travel times of both Rayleigh and Love waves measured by cross-correlating ambient seismic noise for a given path and period band. In an ideal case when noise sources are distributed homogeneously over the medium, for a pair of stations A and B (Figure 6.1) the surface wave arrival time should be identical on the positive (corresponding to wave going from the station A to the station B) and negative correlation time (corresponding to wave going in the opposite direction) as discussed in *Lobkis and Weaver* (2001a), *van Tiggelen* (2003), *Snieder* (2004), *Sánchez-Sesma and Campillo* (2006) and should not change with time. However, three main factors can leads to fluctuations :

- A physical change in the medium would result in either a faster or slower travel time measured in both positive and negative cross-correlation time.
- A clock error in one of the two stations would produce a time shift of the whole cross-correlation resulting in a larger travel time in the positive time and a smaller apparent travel time in the negative time or vice-versa . A change in the phase of the response of one of the sensors would have the same effect.
- A change in the spatial distribution of the source of the noise should affect the positive and negative correlation time independantly, since the positive and negative time are sensitive to noise sources located in different regions (Figure 6.1)

The travel time variation $\delta\tau$ of surface waves reconstructed by cross-correlation of seismic noise with respect to a 'reference travel time', for a given path and period

band can be written :

$$\delta\tau_{ij}(t) \quad = \quad D(t) + \varphi(t) + \varepsilon(t)_{ij} \tag{6.1}$$

In this equation $\delta\tau(t)$ denotes the variation of surface-wave travel time measured either on the positive or on the negative part of the cross-correlation. ij is the couple of components of the noise records which are correlated (either Z,R or T). For example, $\delta\tau_{ZR}(t)$ represents the variation of the arrival time of surface waves measured on the the cross-correlation computed between vertical and radial components. D is the time delay caused by a relative drift of the two station clocks (or a phase shift of the sensor response). φ is the time shift due to a change in the medium. D is an even function where as φ is an odd function : a relative drift of the two station clocks would result in shorter arrival time in the negative time of the cross-correlation, and larger arrival time in the positive time or vice-versa. This property was used in marine acoustics *Sabra et al.* (2005b). On the other hand a change in the medium would result in either shorter or larger arrival time in both negative and positive time. ε_{ij} is the time shift due to a change in the spatial distribution of the source. This last term is expected to decrease when increasing the length of the correlated time series because of the better spatial homogenization of the distribution of noise sources.

By taking the even and odd part of the equation 6.1, we obtain :

$$\frac{\delta\tau_{ij}(t) + \delta\tau_{ij}(-t)}{2} \quad = \quad D(t) + \frac{\varepsilon_{ij}(t) + \varepsilon_{ij}(-t)}{2} \tag{6.2}$$

$$\frac{\delta\tau_{ij}(t) - \delta\tau_{ij}(-t)}{2} \quad = \quad \varphi(t) + \frac{\varepsilon_{ij}(t) - \varepsilon_{ij}(t)}{2} \tag{6.3}$$

These two equations would enable us to evaluate surface wave travel time variations due to a change in the medium φ and to the relative drift of the station clock D, under the assumption that D and φ are large compared to $\frac{\varepsilon_{ij}(\tau)\overset{+}{-}\varepsilon_{ij}(-\tau)}{2}$

Two strategies can be used to evaluate D and φ :
- By using cross-correlation of 'small' time window (one month) one can evaluate the drift with an accurate time resolution. But with such a time window we expect that the term ε to be quite large, so only large instrumental errors can be evaluated.
- By using cross-correlation of a larger time windows, we degrade the time resolution, but we expect the term ε to be smaller. Therefore smaller long term instrumental drifts or physical changes of the medium can be identified more easily.

6.4.1 Data used

We analyze the fluctuations of the apparent travel time of Rayleigh and Loves waves reconstructed by cross correlating seismic ambient noise, by using 11 years (1991-1996 and 1999-2005) of continuous records on three components at three Californian stations : GSC, PFO and PAS (see Figure. 8.1). Before computing the cross-correlations,

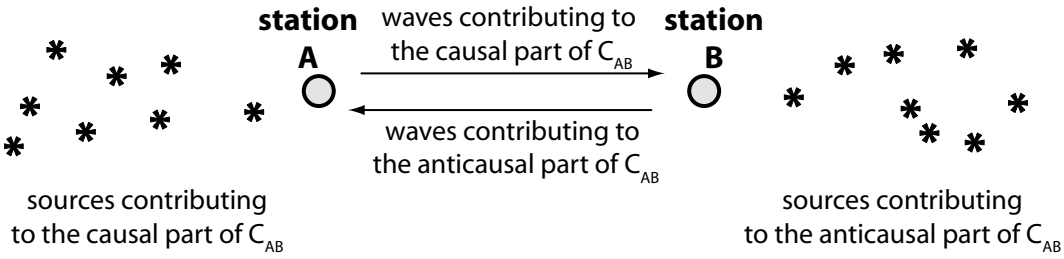

FIG. 6.1: Schematic representation of reconstruction of the causal and the anticausal parts of Green function from the noise.

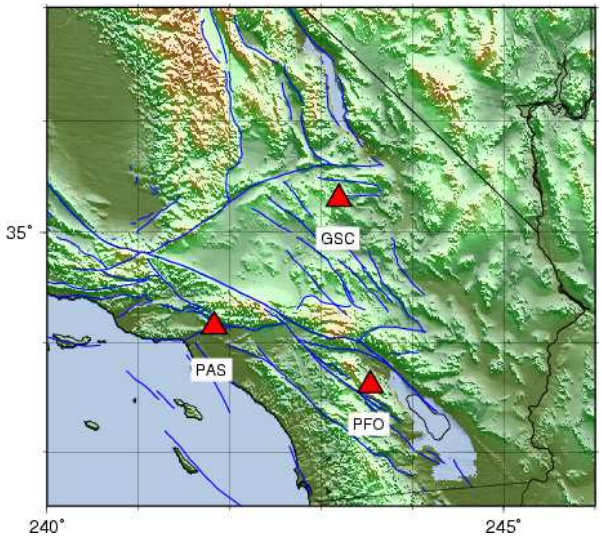

FIG. 6.2: Map of Southern California showing the location of the 3 broadband stations used for this study.

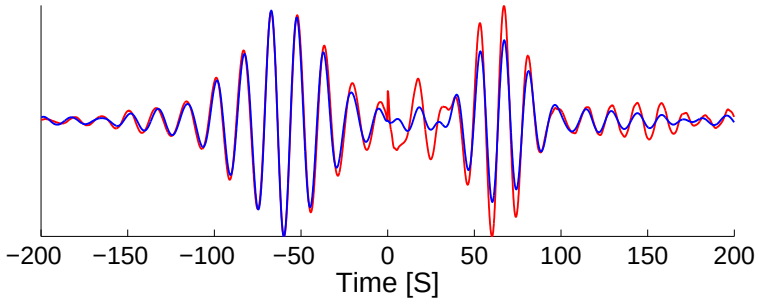

FIG. 6.3: Reference Z-Z cross-correlation for GSC-PAS filtered between 10 and 20 s (blue) and cross-correlation of May 2000 (red). Amplitude are normalized to 1.

records were corrected from the instrumental response and bandpassed either between 5 and 10 s or between 10and 20 s. To reduce the contribution of the most energetic arrivals, we disregarded completely the amplitude and considered one-bit signals only (*Campillo and Paul* (2003) ; *Shapiro and Campillo* (2004)). Horizontal components records were rotated to radial and transverse directions assuming the propagation along the inter-station great circle. We correlated the signal recorded on the components that correspond to non-zero term of the Green Function (ZZ,TT,ZR,RZ and RR). Correlations of one-day records are then stacked month per month or 6 months per 6 months.

6.4.2 Measurement of the time delay

First, we define a 'reference Green function' (RGF) for every path in two period bands (5-10 s and 10-20 s) and for all components (ZZ,TT,ZR,RZ and RR) by computing the one-bit cross-correlations of 6 years (1999-2005) of continuous records of seismic noise. This period was used because we found that no major instrumental errors occurred during these years for any of the three stations considered. The ZZ component of RGF for the path GSC-PAS in the 10-20 s period band is shown on Figure 6.3. This waveform is not perfectly symmetric : the amplitude of the Rayleigh waves is larger for the anticausal part than for the causal part of the cross-correlation. This means than in average, between 1999 and 2005, more energy propagates from PAS to GSC than from GSC to PAS (*van Tiggelen* (2003), *Paul et al.* (2005), *Pedersen et al.* (2006), *Stehly et al.* (2006)). We can also notice that the shapes of the causal and the anticausal signals are quite differents because the spectrum of the noise travelling from GSC to PAS and from PAS to GSC differs as well. We however checked that the two wavetrains are associated with the same dispersion curve. Once the RGFs are defined for all paths, bandwidths, and components, we computed cross-correlations for all 30 days periods during 11 years (1991-1996 and 1999-2005). For every window, we compare the arrival time of the surface wave of the current month, with the reference

for both the causal and anticausal parts. The variation of travel time are measured from the phase of the cross-spectrum computed between the RGF and the Green function estimated in the current window.

To obtain more robust travel-time measurements, we limit our analysis to period bands close to two main microseismic peaks at 7s and 14s that dominate the noise spectrum. At these periods, the sensitivity of Rayleigh waves to the medium maximizes at approximate depths of 6 km and 12 km, respectively. To determine what part of the frequency band is usable, we divide our original frequency band in several narrow-bands (8 for the cross-correlations computed between 10-20 s, and 16 between 5 and 10 s). In every narrow frequency band, we compute the spectral phase difference between the RGF and the current Green function as a function of frequency and use a linear regression to evaluate the apparent time delay. We consider that a measurement is valid if the variance is smaller than a given threshold. This threshold corresponds to 0.003s when processing data in the 5-10 s period band, and 0.01s when considering data in the 10-20 s period band. In the following we take in account only those narrow frequency-bands where this requirement is fulfilled for the entire 11 years of data. The measurement on each of these sub-bands is then averaged to obtain the final apparent delay for the 5-10 s and 10-20 s period bands. Note that the phase differences are always measured at the same frequencies. Therefore, measured travel time variations are not affected by changes in the spectrum of the noise. We average the time delay measured with ZZ, ZR, RZ and RR correlations that we consider to be consisting mostly of Rayleigh waves. We also compute a time delay associated with Loves wave by considering TT correlations.

In average, when considering a single component, 33% of the period band correlated is actually used to measure the time delay. However, when we average the measured time delay over the components, we use 70% of the period band correlated because the measurement is not performed exactly on same periods for the ZZ, ZR, RZ, RR, and TT correlation.

6.5 Results

Figure 6.4a shows the variation of the arrival time of Rayleigh (left panel) and Love (right panel) waves for GSC-PAS in the 5-10 s period band. Measurements performed in the positive time of the correlation are in blue, and those performed in the negative time are in red on the same scale . The positive part of the correlation corresponds to waves travelling from GSC to PAS while the negative time corresponds to waves travelling from PAS to GSC. Two main periods can be distinguished. Between 1991 and 1996, the apparent arrival times exhibit large fluctuations that can be up to 2 seconds. We remark that the same main features of the time delay can be seen for the averaged Rayleigh and Love waves measurements. Between 1999 and 2005, arrival

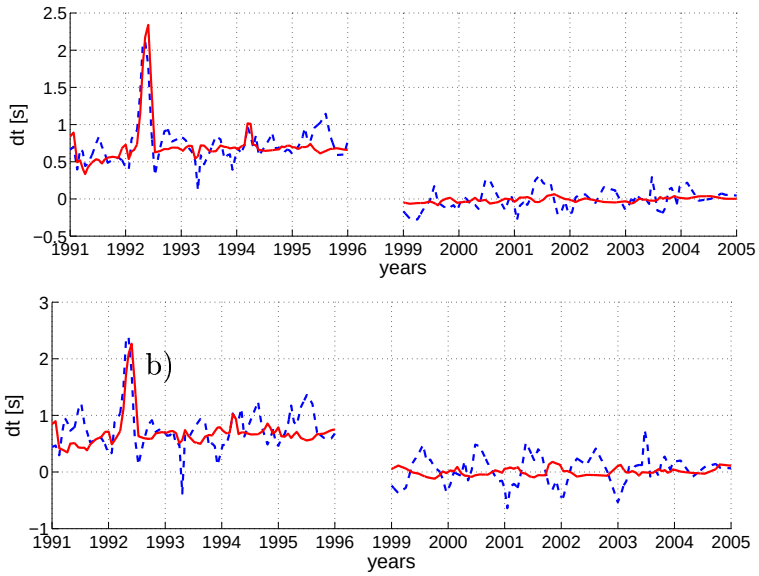

FIG. 6.4: Travel time variations of Rayleigh (a) and Love (b) waves, for the path GSC-PAS measured from one-month cross-correlations in the 5-10 s period band. Travel time of Rayleigh waves are obtained by averaging measurements performed on Z-Z, Z-R, R-Z and R-R cross-correlations. Loves waves are obtained from T-T cross-correlations. Results from the positive and negative correlation time are shown with blue dashed lines and red lines, respectively.

times are very stable and their fluctuations do not exceed 0.2 s. The fluctuations are systematically much larger for the positive time. Let us first consider the 1999-2005 period .

6.5.1 Time delay in the 5-10 s period band between 1999 and 2005

We consider the period 1999-2005, for which we did not detect any obvious instrumental errors. Figure 6.5 shows the apparent travel time variations of surface waves for paths GSC-PAS, GSC-PFO, and PAS-PFO in the 5 to 10 s period band, averaged over all components of the Green function, that is including both Love and Rayleigh waves. The correlations are performed day per day and are then stacked month per month using a moving window. Results from the positive time of the correlation shown with a blue line correspond to waves going from the first to the second station (ie from GSC to PAS, GSC to PFO, and PAS to PFO). The red line shows results from the negative part of the cross-correlations.

The negative time of the correlation of GSC-PAS is sensitive to sources located in the Pacific Ocean and exhibits smaller fluctuations than the positive time which is sensitive to sources in the Atlantic Ocean (*Stehly et al.* (2006)). The fluctuations on the negative time of GSC-PAS never exceed 0.05s and has a variance of only 0.0007s. As the travel time of the Rayleigh waves is about 60 s, the maximum amplitude of the fluctuations and its variance represents respectively 0.08% and 0.0012% of the travel time of the Rayleigh waves. This shows that the reconstruction of the Green function is extremely robust. Also, the equal travel times measured from the negative and positive time of cross-correlations demonstrate that no significant instrumental errors occurred between 1999 and 2005.

Largest fluctuations are found for the causal part of the GSC-PFO cross-correlation. The Green function reconstruction is less stable for this path because it is not directed toward a nearly located oceanic coast. However, even for this 'unfavorable' path the observed fluctuations never exceed 0.75s (i.e., about 1% of the travel time of Rayleigh waves), for a relatively short windows of analysis of one month. Moreover, the fluctuations measured from the negative part are less than 0.19s (i.e., 0.3% of the travel time).

6.5.2 Time delay in the 10-20 s period band between 1999 and 2005

The upper panels of the Figure 6.6 shows the travel time variation of surface waves measured in the 10-20 s period band and averaged on all components. Cross-correlations

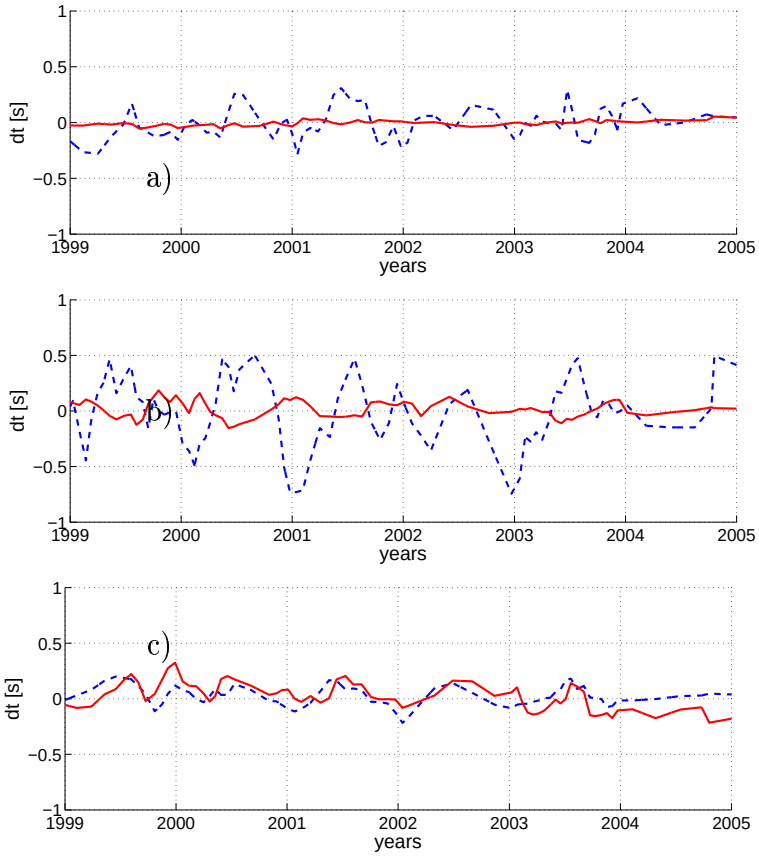

FIG. 6.5: Variation of the surface waves travel times measured in the period band 5-10 s and averaged on all components for different paths : (a) GSC-PAS, (b) GSC-PFO, and (c) PAS-PFO. Results obtained from positive and negative cross-correlations time are shown with blue dashed lines and red lines, respectively.

were computed in a moving one-month window. Similar to Figure 6.5, positive times correspond to waves going from GSC to PAS and from GSC to PFO. We do not show the result for PAS-PFO, because the Green function for this path is not well reconstructed in the 10-20 s period band. The location of sources of the background primary microseism (10-20 s period band) is not constant and has a clear seasonal dependence (*Stehly et al.* (2006)). As a consequence, the term ε_{ij} in equation (6.1) is expected to exhibit significant seasonal oscillations. This can be clearly seen in the measured travel times that exhibit clear fluctuations with a nearly one-year period whose amplitude reache 0.5 seconds for both paths and for the causal and the anti-causal parts of cross-correlations simultaneously. These fluctuations prevent us from achieving a satisfactory accuracy from cross-correlating only one month of data in the 10-20 s period band. To have a more stable Green function reconstruction, we should use longer time windows.

The lower panels of Figure 6.6 shows the variations of the arrival time of surface waves when considering cross-correlation over a moving window of 6 months. These variations never exceed 0.2s for the GSC-PAS path (0.3% of the travel time) and 0.16s for the GSC-PFO path (0.25% of the travel time). These values represents about 1% of the central period of the signal.

6.5.3 Evidence of instrumental time shifts during 1991-1996

Time fluctuation for GSC-PAS

Variations of the arrival time for the path GSC-PAS for the two period bands 5-10 s and 10-20 s during the period 1991-1996 are shown in Figure 6.7. Averaged relative time delays measured from the positive and negative times of the reconstructed Green functions are clearly correlated for the two period bands. In 1992, the time delay $\delta\tau(t)$ exhibits a peak reaching 2 s, that can be observe both for positive and negative correlation time with the same polarity. Also a positive time shift is observed during all the considered period on the positive and negative time. This means that the apparent arrival time become larger on the positive time and smaller in the negative time. These observations cannot be related to changes of the physical properties of the crust that would result in fluctuations of opposite polarity for the positive and negative correlation time (the function $\varphi(t)$ in equation 6.1 is an odd function). It is also unlikely that such almost perfectly even variations are due to the variations in the distribution of the microseism sources because the positve and negative cross-correlation times are not sensitive to sources located in the same region (Figure 6.1). Moreover, all these features can be seen on the two period bands 5-10 s and 10-20 s (Figure 6.7 b) while the source of noise are not expected to be the same for the two period bands (*Stehly et al.* (2006)) . Therefore, these even and period-independant time fluctuations strongly suggest a clock drift or instrumental errors at one of the

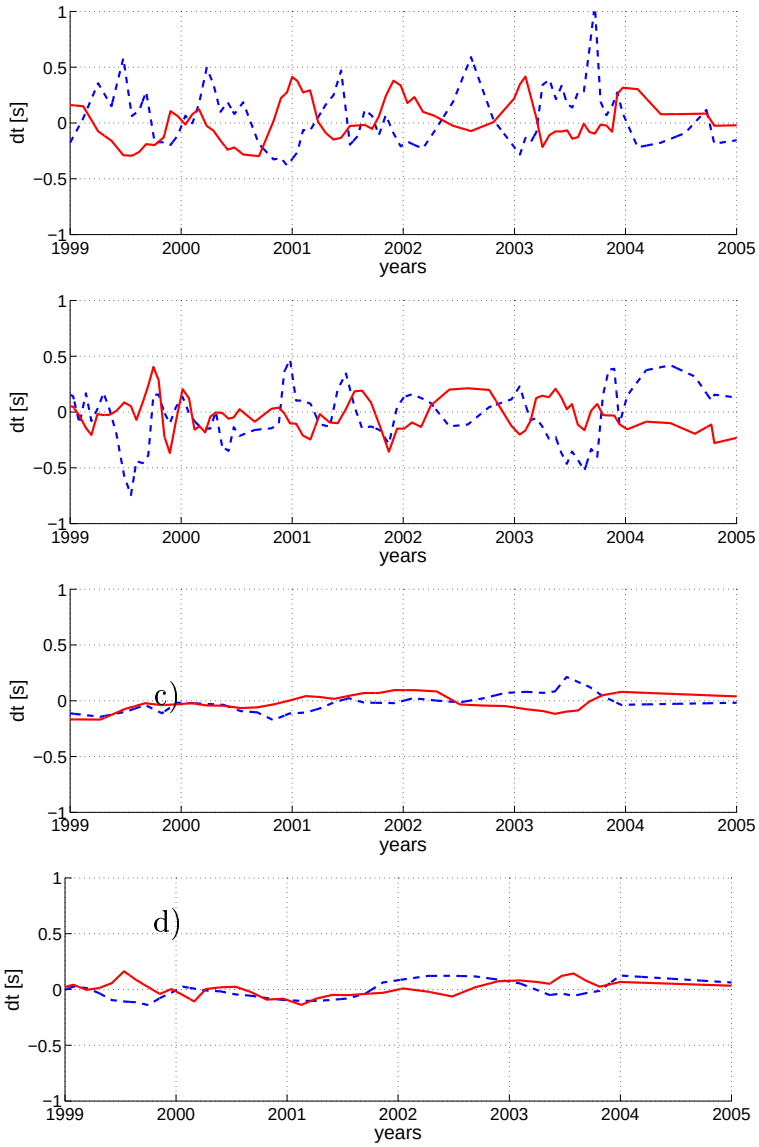

FIG. 6.6: Surface wave travel time variations measured in the 10-20 s period band and averaged on all components. (a) GSC-PAS using one month stacks (b) GSC-PAS using six months stacks. (c) GSC-PFO using one month stacks (d) GSC-PFO with six months stacks. Results obtained from the positive and negative correlation time are shown with blue dashed lines and red lines, respectively.

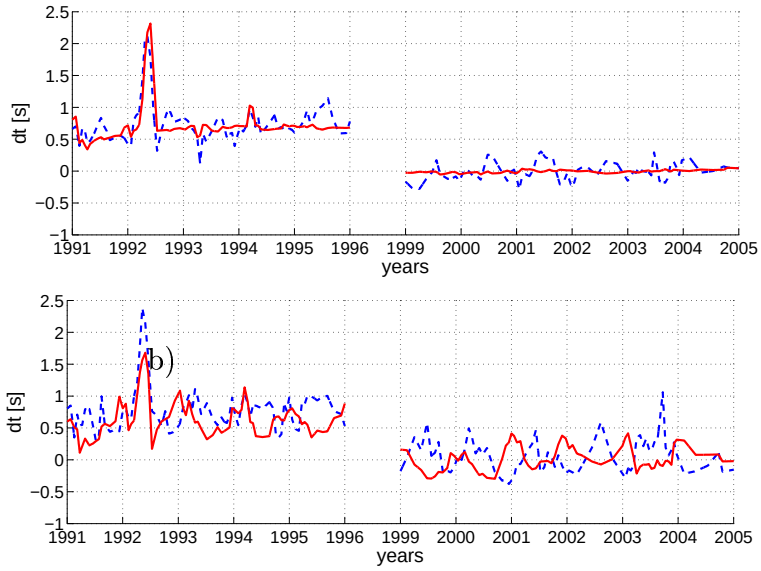

FIG. 6.7: Surface wave travel time variations averaged on all components for the path GSC-PAS at period ranging from (a) 5 to 10 s (b) 10 to 20 s. Results obtained from the positive and negative correlation time are shown with blue dashed lines and red lines, respectively.

two stations.

Evaluating instrumental errors for the GSC-PAS path

By taking the even part of the surface wave travel time fluctuations obtained from the positive and negative noise cross-correlation time , we isolate instrumental errors (see equation 6.2). Results from the two period bands presented in Figure 6.8 show several robust features (i.e., the fluctuations that can be observed in the two period bands simultaneously) : the main peak of 1992, the minor peak of 1994, the offset of the curve between 1991-1996 and 1999-2005, as well as the small positive trend between 1991-1996. Smaller instrumental errors are masked by the fluctuations associated with changes in the spatial distribution of the noise sources.

Comparing observed instrumental errors for different paths

We also evaluate instrumental errors for the GSC-PFO and the PAS-PFO paths during 1991-1996 using a moving one-month window . For PAS-PFO, we only used the period band 5-10 s because the Green function is not well reconstructed between 10 and 20 s. We show the results in Figure 6.9. Relative instrumental errors for GSC-PFO are similar to those measured for GSC-PAS : the main peak of 1992, the minor

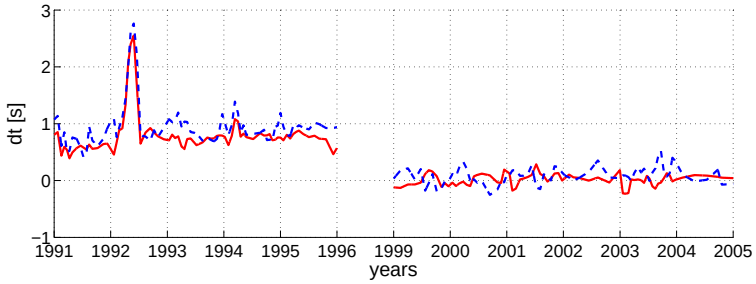

FIG. 6.8: Relative instrumental error between GSC and PAS measured in the 5-10 s (red) and the 10-20 s (blue) period bands by computing the even part of $\delta t(t)$ following equation 6.2.

peak of 1994, and the shift in the arrival time between 1991-1996 and 1999-2005. These features are not observed for the PAS-PFO path. Therefore, they are likely all caused by instrumental problems at GSC. One can notice that the shape and the amplitude of the 1992 and 1994 peaks are not exactly similar for the two paths : GSC-PAS and GSC-PFO. This apparent discrepancy is explained by the different data availabilities for the two pairs of stations. As a consequence, our measurements are not made exactly at the same dates. Moreover, the amplitude of the 1992 peaks is equal to 2.41s for GSC-PFO and 2.14s for GSC-PAS. This suggests there is also a small relative error between PFO and PAS.

Slowly evolving instrumental time shifts

We exclude the period of the two peaks of 1992 and 1994, and we consider only long term variations of the time delay that are much smaller than the 1992 peaks. One can notice in Figure 6.9 that the average values of the measured instrumental error change slightly with time for the three paths. Three main periods can be distinguished :1991-march 1992, august 1992-february 1994, and may 1994-december 1995. We average the measurement performed in 5-10 s and 10-20 s period band, in this three main periods to evaluate the long term intrumental errors. For example, for GSC-PAS between 1991 and the beginning of the 1992 peak, the average error is 0.585s whereas it is 0.65s between the 1992 and 1994 peaks and 0.67s after the 1994 peak. This suggests long term drifts of the clock at some of the stations, or others slowly evolving instrumental problems. Measurements of the differents average values of the surface wave arrival times measured from the noise correlations are summarized in Table 1. We can check that they actually correspond to a relative instrumental errors of the stations, by verifying a closure relation. The relative instrumental error of GSC-PAS - GSC-PFO + PAS-PFO should be equal to zero. Observed closure amplitudes are smaller than 0.02 s which is one order of magnitude smaller than the measured long term instrumental errors.

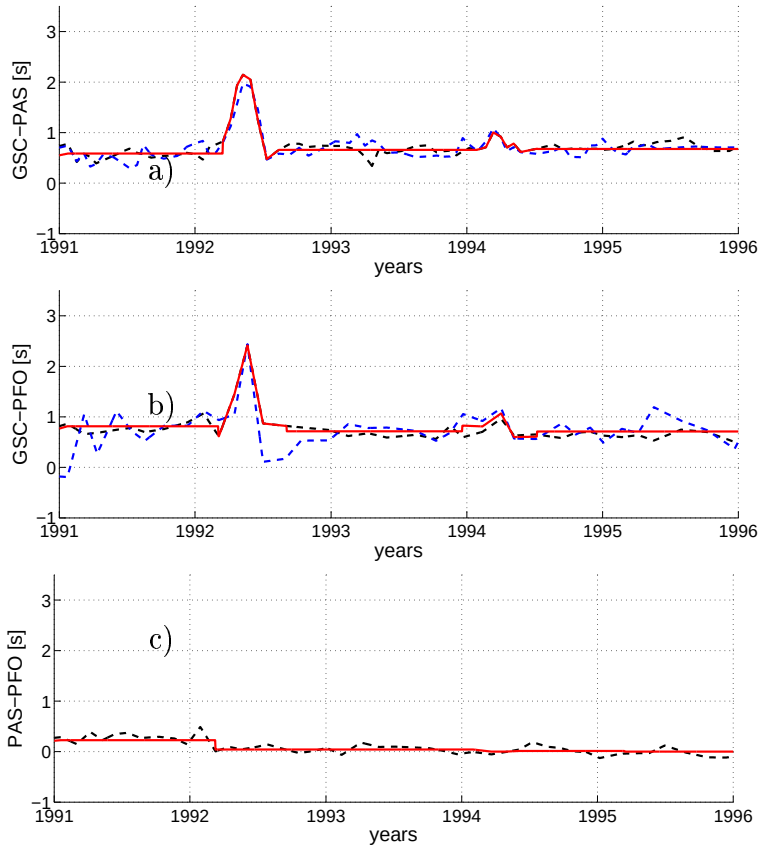

FIG. 6.9: Instrumental errors computed using equation 6.2 for different paths : (a) GSC-PAS, (b) GSC-PFO, and (c) PAS-PFO. Measurement performed in the 5-10 s period band are shown in black, and those between 10 and 20 s are shown in blue. In red we show the "shematic" relative instrumental errors defined as following :
-During the peak of 1992 and 1994, we use the average value of the instrumental errors computed in the period band 5-10 s and 10-20 s using one month stack. We do not average the measured value over time.
- The rest of the time, we show the "slowly evolving instrumental error", by taking the average value of the relative clock error evaluated during the three period of time : Jan 1991-Mar 1992, Aug 1992-Feb 1994 and May 1994-Dec 1995. Again we average measurements performed in the two period bands, 5-10 s and 10-20 s. The value used are summed up on table 6.1.

	1991-1992	1992-1994	1994-1996
GSC-PAS	0.585	0.658	0.675
GSC-PFO	0.814	0.714	0.709
PAS-PFO	0.226	0.041	0.013
Closure	-0.0018	-0.014	-0.02

TAB. 6.1: Average values of the relative instrumental errors for three stations pairs : GSC-PAS, GSC-PFO and PAS-PFO computed with equation 6.2 from moving stacks of one month of cross-correlations of ambient seismic noise, performed in the two period band 5-10 s, and 10-20 s. The three-station closure relation of relative instrumental errors is (GSC-PAS)-(GSC-PFO)+(PAS-PFO).

Evaluating station time shifts from relative time shifts measurements

In the previous sections, we evaluated the relative instrumental errors between pair of stations. The next step is to obtain the absolute instrumental errors at each stations. Obtaining individual station errors from relative measurements is not straightforward, and has not a unique solution : The relative clock error of GSC-PAS, GSC-PFO, and PAS-PFO give us three equations, but only two of them are independant whereas we have 3 unknowns : the error at GSC, PAS and PFO. Concerning the major dysfunctions (the peaks of 1992 and 1994), we have already seen that they are all due to a problem at GSC as seen on section 6.5.3.

For the slowly evolving errors, although several scenarios could fit our measurements, we propose the following model under the arbitrary assumption that there is no error on PAS (this subjective hypothesis is only considered to check how consistent are our measurements) :

- Between 1991 and the beginning of the peak of 1992 (see Table 1), GSC has error equal to 0.58 s, PFO an error of about 0.23 s, and PAS no error at all. This would explain that the relative error for the GSC-PAS path is 0.58s, the one for GSC-PFO is 0.81 s, and for PAS-PFO it is equal 0.23 s.
- Between the peaks of 1992 and 1994 : GSC has an error of +0.65 s and PFO has an error of -0.056 s.
- between 1994 and 1996, GSC would have an error of +0.67 s, and PFO an error of -0.03 s.

Our evaluation of individual station errors are summarized in Table 2.

	1991 1992	May 1992	1993 1994	Apr 94	1995
GSC	+0.58s	+2.18s	+0.65s	+1.00s	+0.67s
PFO	-0.23s		-0.056s	-0.06s	-0.03s
PAS	+0s				

TAB. 6.2: Interpretative values of instrumental errors for the stations GSC and PFO, under the assumption that there is no error at PAS and deduced from the measurements of relative instrumental errors of GSC-PAS, GSC-PFO, and PAS-PFO.

Correcting instrumental time shifts

After evaluating the instrumental errors $D(t)$ (see equation 6.2, and figure 6.9), we remove them from the data. Figure 6.10 presents the travel time variations remeasured for the GSC-PAS path between 5 and 10 s after removing the estimated instrumental errors. We corrected the data from the average peak of 1992 and 1994s measured in the 5-10 and 10-20 s period band, using stack of one month of cross correlation, as well as the slowly evolving error evaluated by taking the average value of the time delay $\delta\tau(t)$ for the three periods 1991-1992, 1992-1994, and 1994-1996. This corresponds to the instrumental errors shown in red on Figure 6.9, and to the value in Tables 1 and 2.

Following equations 6.1 and 6.2, the measured time delay fluctuations $\delta\tau^*$ after correcting the data from the instrumental errors are :

$$\delta\tau^*_{ij}(t) = [D(t) + \varphi(t) + \varepsilon_{ij}(t)] - [D(t) + \frac{\varepsilon_{ij}(t) + \varepsilon_{ij}(-t)}{2}] \quad (6.4)$$

$$\delta\tau^*_{ij}(t) = \varphi(t) + \frac{\varepsilon_{ij}(t) - \varepsilon_{ij}(-t)}{2} \quad (6.5)$$

φ is the time shift due to a change in the medium and ε is the time shift due to a change in the spatial distribution of the sources of noise. The peaks of 1992 and 1994 have completly disappeared as expected, as well as the time shift between the 1991-1996 and 1999-2005 period and the small trend between 1991 and 1996 (Figure 6.10).

The measured time delay in the positive and negative time of the cross-correlation are not correlated (Figure 6.10). In other words after correction of the instrumental errors, $\delta\tau^*$ is not an odd function, whereas φ is an odd function (see section 6.4). This means that in equation 6.4, φ is small with regard to $\frac{\varepsilon_{ij}(t)-\varepsilon_{ij}(-t)}{2}$. Therefore, we could not detect any change of the medium and the fluctuations of the remeasured time delay are mainly due to changes in the spatial distribution of the noise sources.

Travel time fluctuations after the correction of instrumental errors have a variance

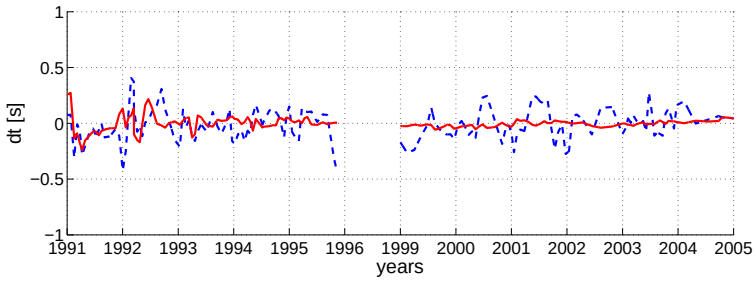

FIG. 6.10: 5-10 s surface wave travel time variations averaged on all components for the GSC-PAS path after correcting the instrumental errors shown on figure 6.9. Results obtained from the positive and the negative correlation times are shown with blue dashed lines and red lines, respectively.

of 0.012s and 0.0022s on the positive and negative time, respectively. This represents 0.02% and 0.003% of the travel time of Rayleigh waves. This shows that the Green Functions reconstructed by correlating ambient seismic noise are accurate enough to detect and to correct small instrumental errors and to measure inter-station travel times with a precision of a few tenths of second for stations 200 km apart .

6.6 Conclusions

We studied variations of surface wave travel times measured from cross-correlations of seismic noise records between three seismic stations in California during 11 years in two period bands : 5-10 s and 10-20 s. Simultaneous analysis of causal and anticausal parts of cross-correlations allowed us to isolate and to correct various instrumental time shifts occurred between 1991 and 1996. This measure of instrumental error does not require any assumption on the wave velocity and relies only on the fundamental properties of time symetry. It could be used routinely to detect instrumentals problems.

Remaining travel time fluctuations were attributed to errors caused by variations in distribution of the noise sources. In the 10-20 s period band, these errors exhibit strong fluctuations with a clearly identified one-year period that is related to seasonal migration of sources of the primary microseism (*Stehly et al.* (2006)). These seasonal fluctuations can be reduced by averaging the results in longer time windows.

After introducing all discussed corrections, the inter-station travel times can be measured with a precision of a few tenths of a second for stations separated by ∼200 km. The achieved level of accuracy was not sufficient to unambiguously detect travel time variations associated with changes of the physical properties of the crust for the three station pairs and during the considered 11 years. The obtained results are,

however, encouraging because they demonstrated that the travel time variations can be measured with errors that are smaller than 0.3% of the inter-station travel time and than 1% of the considered wave period. First, this indicates that the precision of the measurement is at least comparable with the one obtained with earthquakes implying that the noise correlation is definitely a good approach for high resolution seismic imaging. Second, the noise based travel time measurements over shorter paths are expected to be more sensitive to localized changes in the media. Therefore, for future experiments we suggest to consider pairs (or arrays) of stations separated only by a few tens of kilometers up to one hundred of kilometers and located very close to tectonically active features such as active faults or volcanos. With such configurations the achieved absolute level of accuracy of the noise-based travel time measurements that can be achieved may be sufficient to detect variations of the physical properties of the crust caused by tectonic or volcanic processes. Using surface waves extracted from the noise in the microseismic peak frequency bands will allow us to monitor relatively deep parts of the crust where it is very difficult to obtain repeatable measurements based on artificial seismic sources.

6.7 acknowledgments

This work does not intend by any way to criticize the important work that has been done by the researcher and engineers who developed instruments and networks which recorded the data used in this work and to which they generously give an open access to the community. All the seismic data used in this study have been obtained at the IRIS DMC (http ://www.iris.edu/), and comes from the Southern California Seismic Network.

This research has been supported by the Commissariat à l'Energie Atomique (CEA, France), by the Agence National de la Recheche (France) under contract PrecorSis (05-CATT-010-01) and CoherSis, and by the European Community (project Neries).

Quatrième partie

Tomographie à partir de corrélations de bruit de fond

Chapitre 7

High Resolution Surface Wave Tomography From Ambient Seismic Noise

N.M. Shapiro, M. Campillo, L. Stehly, M.H. Ritzwoller
Article publié dans *Science* (2005)

Sommaire

7.1 Introduction à l'article

Après avoir étudié l'origine du bruit de fond et montré que les corrélations de bruit en Californie étaient stables et suffisamment robustes pour identifier des dérives d'horloge interne des stations, nous présentons ici une première application des corrélations à la tomographie.

Nous testons cette nouvelle méthode en Californie. Outre la grande qualité des données disponibles, cette région est caractérisée par des contrastes de vitesse importants

selon les diverses unités géologiques, ce qui en fait une zone de prédilection pour tester les corrélations. Nous utilisons un mois de bruit de fond enregistré entre août et septembre 2004 par 62 stations en Californie du Sud. Les enregistrements sont corrélés entre les 1891 couples de stations. Nous sélectionnons les meilleurs trajets, en fonction du rapport signal sur bruit, et en nous assurant que les vitesses mesurées sur les temps positifs et négatifs des corrélations sont similaires. Nous gardons ainsi entre 600 et 900 mesures de vitesse de groupe selon les périodes considérées, nous permettant d'obtenir des cartes de vitesse de groupe des ondes de Rayleigh entre 5 et 20s de période.

7.2 abstract

Cross-correlating one month of ambient seismic noise recorded at USArray stations in California yields hundreds of short period surface-wave group-speed measurements on inter-station paths. We used these measurements to construct tomographic images of the principal geological units beneath California, with low-speed anomalies corresponding to the main sedimentary basins and high-speed anomalies corresponding to the igneous cores of the major mountain ranges. This method can improve the resolution and fidelity of crustal images obtained from surface wave analyses.

7.3 Introduction

The aim of ambitious new deployments of seismic arrays, such as the PASSCAL and USArray programs, is to improve the resolution of images of Earth's interior by adding more instruments to regional- and continental-scale seismic networks. Traditional observational methods cannot fully exploit emerging array data because they are based on seismic waves emitted from earthquakes, which emanate from select source regions predominantly near plate boundaries and are observed at stations far from source regions, such as most locations within the United States. With such teleseismic observations, high frequency information is lost due to intrinsic attenuation and scattering and resolution is degraded by the spatial extent of the surface wave's sensitivity which expands with path length *Nolet and Dahlen* (2000); *Spetzler et al.* (2002); *Ritzwoller et al.* (2002a). Here we move beyond the limitations of methods based on earthquakes and recover surface wave dispersion data from ambient seismic noise *Shapiro and Campillo* (2004).

The basic idea of the new method is that cross-correlation of a random, isotropic wavefield computed between a pair of receivers will result in a waveform that differs only by an amplitude factor from the Green function between the receivers *Weaver*

and Lobkis (2001); *Snieder* (2004). This property is reminiscent of the fluctuation-dissipation theorem *Kubo* (1966) which posits a relation between the random fluctuations of a linear system and the system's response to an external force. The relation is widely used in a variety of physical applications, finding its roots in early works on Brownian noise *Kos and Littlewood* (2004); *Einstein* (1905). Recent results in helioseismology *Duvall et al.* (1993), acoustics *Lobkis and Weaver* (2001b); *Derode et al.* (2003b); *Roux and Kuperman* (2004); *Larose et al.* (2004b); *Malcolm et al.* (2004), and seismology *Shapiro and Campillo* (2004); *Campillo and Paul* (2003) suggest that such a statistical treatment can be applied to non-thermal random wavefields, in particular to long series of ambient seismic noise because the distribution of the ambient sources randomizes when averaged over long times. Ambient seismic noise is additionally randomized by scattering from heterogeneities within Earth *Hennino et al.* (2001). Surface-waves are most easily extracted from the ambient noise *Shapiro and Campillo* (2004) because they dominate the Green function between receivers located at the surface and also because ambient seismic noise is excited preferentially by superficial sources, such as oceanic microseisms and atmospheric disturbances *Friedrich et al.* (1998); *Tanimoto and Um* (1999); *Ekström* (2001); *Rhie and Romanowicz* (2004). The seismic noise field is often not perfectly isotropic and may be dominated by waves arriving from a few principal directions. To reduce the contribution of the most energetic arrivals, we disregard the amplitude by correlating only one-bit signals *Campillo and Paul* (2003); *Larose et al.* (2004b) before the computation of the cross-correlation.

7.4 Dispersion curves in California

Examples of cross-correlations between pairs of seismic stations in California appear in Fig. 1. Cross-correlations between two station pairs (MLAC - PHL, SVD - MLAC) in two short period bands (5 s - 10 s, 10 s - 20 s) are presented using four different one month time series (January, April, July, October 2002). For each station-pair, results from different months are similar to one another and to the results using a whole year of data, but differ between the station-pairs. Thus, the emerging waveforms are stable over time and characterize earth structure between the stations. In addition, the cross-correlations of noise sequences are very similar to surface-waves emitted by earthquakes near one receiver observed at the other receiver. This confirms that the cross-correlations approximate Green functions of Rayleigh waves propagating between each pair of stations and that one month of data suffices to extract Rayleigh wave Green functions robustly in the period band of interest here (7 s - 20 s)

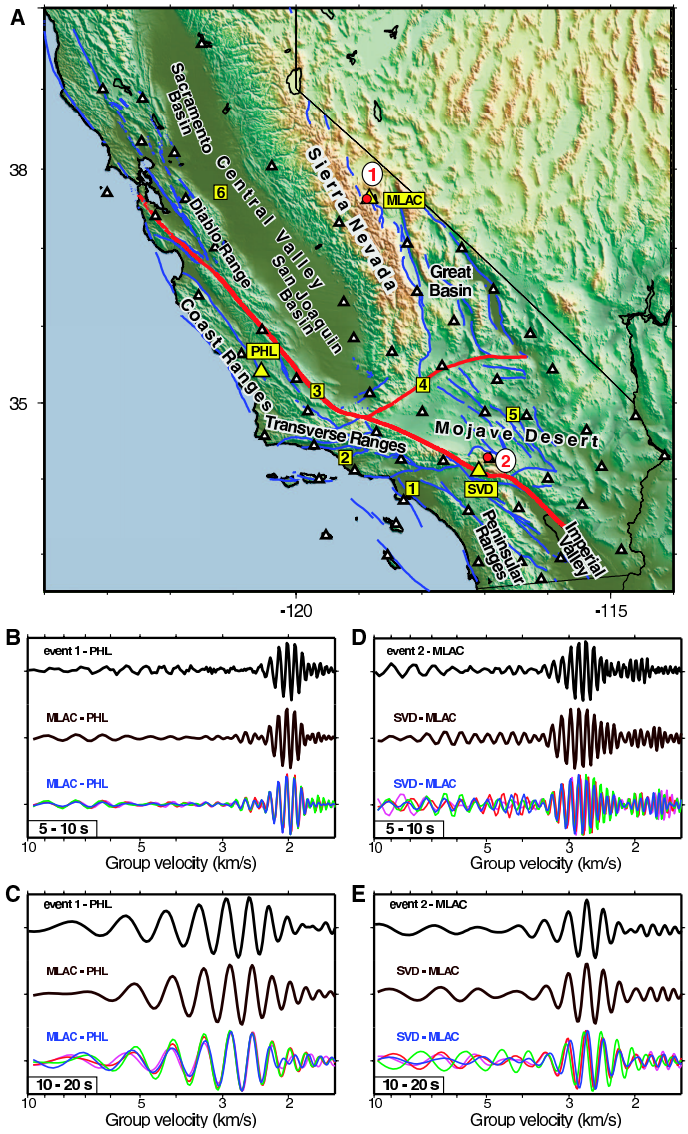

FIG. 7.1: Waveforms emerging from cross-correlations of ambient seismic noise compared with Rayleigh waves excited by earthquakes. (A) Reference map showing the locations of the principal geographical and geological features discussed in the test. White triangles show the locations of the USArray stations used in this study (5 of the 62 stations are located north of 40°N). Blue and red solid lines are locations of known active faults. Yellow rectangles with digits indicate the following features : (1) Los Angeles Basin ; (2) Ventura Basin ; (3) San Andreas fault ; (4) Garlock fault ; (5) Mojave shear zone ; and (6) Stockton Arch. (B) Comparison of waves propagating between stations MLAC and PHL (yellow triangles), bandpassed between 5 and 10 s period. The upper trace (black) is the signal emitted by earthquake 1 (red circle in A) near MLAC observed at PHL, the middle trace (gold) is the cross-correlation from one year of ambient seismic noise observed at stations MLAC and PHL, and the lower traces are cross-correlations from four separate months of noise observed at the two stations in 2002 (magenta – January, red – April, green – July, blue – October). The earthquake-emitted signal was normalized to the spectrum of the cross-correlated ambient noise. (C) Similar to (B), but with the bandpass filter between 10 s and 20 s period. (D) Similar to (B), but between stations SVD and MLAC (yellow triangles). Earthquake 2 is near station SVD observed at station MLAC. (E) Similar to (D), but with the bandpass filter between 10 s and 20 s period.

7.5 Application to USArray data

We selected 30 relatively quiescent days (during which no M>5.8 earthquakes occurred) of continuous 1 sample per second data from 62 USArray stations within California from August and September 2004. Short period surface wave dispersion curves are estimated from the Green functions using frequency-time analysis *Levshin et al.* (1989); *Ritzwoller and Levshin* (1998); *Shapiro and Singh* (1999) from the 1891 paths connecting these stations. We rejected waveforms with "signal-to-noise" ratios smaller than 4 and for paths shorter than two wavelengths, resulting in 678 and 891 group speed measurements at periods of 7.5 s and 15 s, respectively (Fig. S2). We then applied a tomographic inversion *Barmin et al.* (2001) to these two data sets to obtain group speed maps on a 28 km $\times$ 28 km grid across California (Fig. 2). The maps produced variance reductions of 93% and 76% at 7.5 s and 15 s, respectively, relative to the regional average speed at each period. To test the robustness of the inversion, we applied the same procedure to a second month of data and produced similar tomographic maps (Fig. S3) The resolution of the resulting images is about the average inter-station distance, between 60 and 100 km across most of each map (Fig. S4).

7.6 Discussion and interpretation of dispersion maps

A variety of geological features are recognizable in the estimated group-speed dispersion maps (Fig. 2). For the 7.5 s Rayleigh wave, which is most sensitive to shallow crustal structures no deeper than about 10 km, the dispersion map displays low group speeds for the principal sedimentary basins in California, including the basins in the Central Valley, the Salton Trough in the Imperial Valley, the Los-Angeles Basin, and the Ventura Basin. Regions consisting mainly of plutonic rocks (e.g., the Sierra Nevada, the Peninsular Ranges, the Great Basin, and the Mojave Desert region) are characterized predominantly by fast group speeds. Somewhat lower speeds are observed in the Mojave Shear Zone and along the Garlock fault. The Coast Ranges, the Transverse Ranges, and the Diablo Range which are mainly composed of sedimentary rocks are characterized by low group speeds, with the exception of the Salinian block located south of Monterey Bay.

For the 15 s Rayleigh wave, sensitive mainly to the middle crust down to depths of about 20 km, very fast group speeds corresponds to the remnants of the Mesozoic volcanic arc : the Sierra Nevada and the Peninsular Ranges composed principally of Cretaceous granitic batholiths. The map also reveals the contrast between the western and eastern parts of the Sierra Nevada *Jones et al.* (1994). The group speeds are lower in the Great Basin and in the Mojave Desert, indicating that the middle crust in these areas is probably hotter and weaker than in the Sierra Nevada. In the Central Valley,

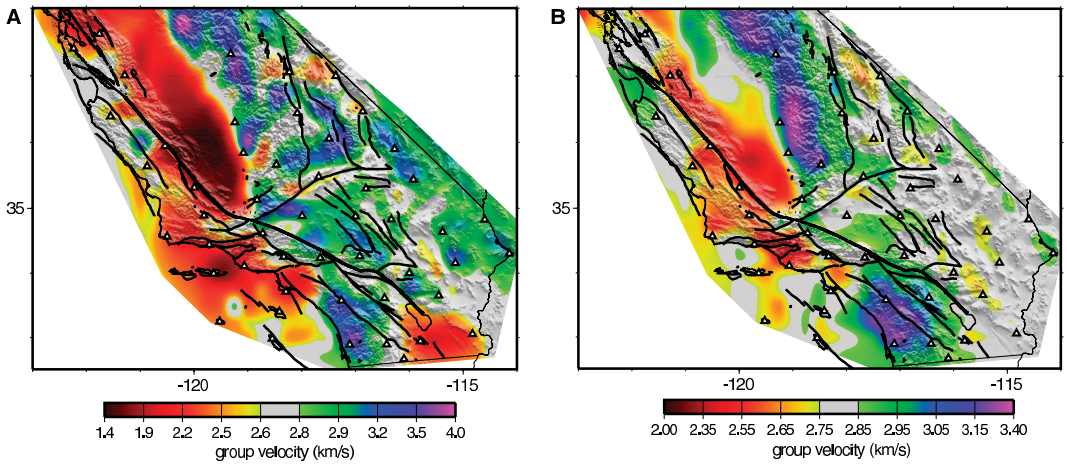

FIG. 7.2: Group speed maps constructed by cross-correlating 30 days of ambient noise between USArray stations. (A) 7.5 s period Rayleigh waves. (B) 15 s period Rayleigh waves. Black solid lines show known active faults. White triangles show locations of USArray stations used in this study. Similar maps from a different 1 month of data are shown in the Supplementary Materials.

slow group speeds are associated with two deep sedimentary basins, the San Joaquin Basin in the south and the Sacramento Basin in the north separated in the middle by the igneous dominated Stockton Arch *Wilson et al.* (1999). Group speeds are low in the sedimentary mountain ranges; e.g., the Transverse Ranges, the southern part of the Coast Ranges, and the Diablo Range. Neutral to fast wave speeds are observed for the Salinian block. In this area, the 15 s map shows a contrast between the high speed western wall of the San-Andreas fault, composed of plutonic rocks of the Salinian block, and its low-speed eastern wall composed of sedimentary rocks of the Franciscan formation.

7.7 Conclusions

These results establish that Rayleigh wave Green functions extracted by cross-correlating long sequences of ambient seismic noise, which are discarded as part of traditional seismic data processing, contain information about the structure of the shallow and middle crust. The use of ambient seismic noise as the source for seismic observations addresses several shortcomings of traditional surface wave methods. The method is particularly advantageous in the context of temporary seismic arrays such as the Transportable Array component of USArray or PASSCAL experiments because it can return useful information even if earthquakes do not occur. The short period dispersion maps produced by the method can provide homogeneously distributed

information about shear wave speeds in the crust which are hard to acquire with traditional methods. The new method enhances resolution because measurements are made between regularly spaced receivers which may lie much closer to one another than to earthquakes.

It may seem initially surprisingly that deterministic information about the Earth's crust can result from correlations of ambient seismic noise. This result reminds us that random fluctuations can, in fact, yield the same information as provided by probing a system with an external force *Kos and Littlewood* (2004) and that not all noise is bad. In seismology, external probing through active seismic sources (e.g., explosions) may be prohibitively expensive and earthquakes are both infrequent and inhomogeneously distributed. In many instances, merely "listening" to ambient noise may be a more reliable and economical alternative.

Competing interests statement.

The authors declare that they have no competing financial interests.

Acknowledgments

The data used in this work were obtained from the IRIS Data Management Center. We are also particularly grateful to Mikhail Barmin for help with the tomographic code and to Peter Goldstein for clarifications about the SAC program. We thank Craig Jones for a tutorial on the geology of California and Eric Larose, Oleg Lobkis, Ludovic Margerin, Roger Maynard, Anne Paul, Bart van Tiggelen, and Richard Weaver for helpful discussions. We acknowledge the support from CNRS/INSU (program DyETI) and CEA (France).

Chapitre 8

Tomography of the Alpine Region from Observations of Seismic Ambient Noise

L. Stehly, B. Fry, M. Campillo, N.M. Shapiro, J. Guilbert, L. Boschi, D. Giardini

Manuscrit en préparation

Sommaire

Résumé

Dans ce chapitre, nous utilisons les corrélations de bruit afin d'étudier la lithosphère en Europe de l'Ouest, et plus particulièrement dans les Alpes. Au chapitre précédent, nous avons montré que les corrélations de bruit permettaient d'obtenir des cartes de vitesse de groupe du mode fondamental des ondes de Rayleigh à l'échelle régionale entre 5 et 20s de période. Nous souhaitons à présent mieux cerner les possibilités et les limitations de cette méthode. Plusieurs questions se posent : est-il possible de proposer un modèle crustal réaliste en utilisant simplement un an bruit, sans imposer d'apriori sur le résultat ? Dans quelle mesure la directivité du bruit limite t-elle le nombre de trajets pour lesquels nous pouvons mesurer des vitesses de groupe ? Jusqu'à quelle période le bruit de fond est-il utilisable ? Les ondes de Love sont-elles également visibles sur les corrélations ?

Pour répondre à ces question, nous disposons d'un an de données enregistrées par 150 stations réparties dans toute l'Europe de l'Ouest, avec une densité particulièrement élevée en Suisse. La méthodologie employée est proche de celle du chapitre précédent : nous corrélons les enregistrements de bruit entre toutes les paires de stations. Disposant de stations 3 composantes, nous corrélons à la fois les enregistrements verticaux, radiaux et transverses entre chaque couple de stations, nous permettant ainsi de reconstruire les ondes de Rayleigh (sur les corrélations Z-Z, Z-R, R-Z et R-R), ainsi que les ondes de Love (sur la composante T-T). Nous sélectionnons les meilleurs trajets, ceux pour lesquels nous pouvons mesurer des vitesses de groupe fiables, d'une part en fonction du rapport signal/bruit des ondes de surface reconstruites, et d'autre part en nous assurant que nous mesurons les mêmes vitesses sur les temps positifs et négatifs des corrélations. Nous obtenons ainsi plus de 3000 mesures de vitesse de groupe pour les ondes de Love et de Rayleigh à des périodes allant de 5 à 80s.

Ces mesures nous permettent d'établir des cartes de vitesse de groupe des ondes de Love et de Rayleigh entre 5 et 80 s de période. La directivité du bruit, ainsi que la répartition inhomogène des stations fait que l'on a plus de mesures selon certains azimuts que selon d'autres. Par conséquent nos cartes de vitesse de groupe ont une meilleure résolution dans la direction Sud-Est que Nord-Est.

Finalement, nous inversons les cartes de vitesse de groupe des ondes de Rayleigh afin de déterminer la profondeur du Moho sous les Alpes. Nos résultats sont en bon accord avec les études précédentes des Alpes. Ceci indique que les corrélations de bruit permettent d'obtenir des modèles crustaux réalistes rivalisant avec ceux obtenus par des méthodes actives.

abstract

We use seismic ambient noise correlation to study the lithosphere in western Europe. Cross correlation of one year of noise recorded at 150 3-components broadband stations yields more than 3000 Rayleigh and Love wave group velocity measurements. These measurements are used to construct Rayleigh and Love group velocity models of the Alpine region and surrounding area in the 5-50s period band. The seismic noise recorded in Europe is dominated by noise originating from the Northern Atlantic ocean. This anisotropy of the noise and the uneven station distribution affect the azimuthal distribution of the paths where we obtain reliable group velocity measurements. As a consequence our group velocity models have better resolution in the South-East direction than in the North-East direction. Finally we invert the resulting Rayleigh wave group velocity maps to determine the Moho depth. Our results are in good agreement with the result of the numerous active experiments in the Alps.

Introduction

Accurate high-resolution imaging of the crust is necessary to understand the interaction between mantle dynamics and near surface geological processes. Observational methods in seismology are typically based on earthquake seismograms or rely on active sources. Specifically, surface wave tomography has traditionally exploited the frequency-dependent wave velocity (dispersive) characteristic of Love and Rayleigh waves. Dispersion has been measured as an average property of the propagation path of earthquake waves traveling from an earthquake source to a station (1-station method, e.g. *Trampert and Woodhouse* (1995); *Ekström et al.* (1997); *Ritzwoller and Levshin* (1998) ; *Pasyanos* (2005)), or between two stations (2-station method) with approximately the same azimuth or backazimuth with respect to the earthquake source (*McEvilly* (1964) ; *Dziewonski et al* (1972) ; *Meieret al.* (2004)). When considering surface wave dispersion measurements along earthquake source-station paths, the resolution is limited by two main factors : (1) nonuniformity in the geographical distribution of earthquake sources and receivers, and (2) inherent attenuation of the high-frequency content of teleseismic records. The heterogeneous distribution of sampled fresnel zones resulting from (1) limits resolution in regions sampled by few or no raypaths of observed waves. At teleseismic distances, most of the high frequency information is lost due to the attenuation of the medium. As surface waves sample the average material properties to a given depth and higher frequency signals sample shallower structure, losing the high-frequency component of the earthquake signal limits the ability to image the crustal structure.

Recent theoretical and laboratory studies have demonstrated that the time cross-correlation function of random wavefields computed at two distant receivers contains

the Green's Function between these two receivers (*Weaver and Lobkis* (2001); *Lobkis and Weaver* (2001a); *Colin de Verdière* (2006a,b); *Sánchez-Sesma et al.* (2006a,b); *Larose et al.* (2006b) and references therein). In seismology this idea has been successfully applied to the seismic coda (*Campillo and Paul* (2003),*Paul et al.* (2005)) and the seismic noise (*Shapiro and Campillo* (2004); *Shapiro et al.* (2005); *Sabra et al.* (2005c)). Ideally, this gives us the possibility to measure surface wave dispersion curves between any pair of stations of an array using only ambient noise records.

Stehly et al. (2006) have shown that the seismic noise sources in the [5-20 s] period band are distributed over a large surface when integrated over a long time. This means that in the case of the seismic ambient noise, the randomness is ensured mainly by the random spatial distribution of the sources when considering long time series, as well as scattering. Following the cross-correlation procedure of *Shapiro and Campillo* (2004), we retrieve the Green's function between two stations by correlating background seismic noise records. The emerging signal is dominated by surface waves because the background seismic noise in our processed data consists mainly of surface waves (e.g. *Friedrich et al.* (1998), *Ekström* (2001)) and because the expected actual Green function is also dominated by surface waves. The reconstructed Green's functions are stable over time and robust enough to measure group velocity dispersion with a precision of a few tenths of a second, independently of the azimuth of the considered station-station path (*Stehly et al.* (2007)).

Passive imaging from seismic noise and Rayleigh wave group velocities has first been used by *Shapiro et al.* (2005) and *Sabra et al.* (2005c), who provided images of the Californian crust. More recently, noise based surface-wave tomography has been applied in Tibet *Yao et al.* (2006), New Zealand *Lin et al.* (2007), Korea *Kang and Shin* (2006), Finland *Pedersen et al.* (2006) and to produce large-scale Rayleigh wave group velocity maps across Europe *Yang et al.* (2007). At a smaller scale, *Brenguier et al.* (2007b) investigated the 3D S-wave structure of the Piton de la Fournaise volcano.

In this paper we use seismic ambient noise correlation to study the lithosphere in western Europe. Using 150 broaband stations, we determine the surface wave velocity structure of the Alpine region and surrounding area in the 5-50s period band. Using 3-component seismic stations allows us to measure both Rayleigh and Love waves dispersion curves. We then invert the resulting Love and Rayleigh wave group velocity maps, to determine the Moho depth.

8.1 Data Processing

We used one year of continuous records from October 2004 to October 2005 at 150 3-components broadband European stations. Our aim is to focus on the Alps, where the station density is particularly large (figure 8.1). All the records are processed day

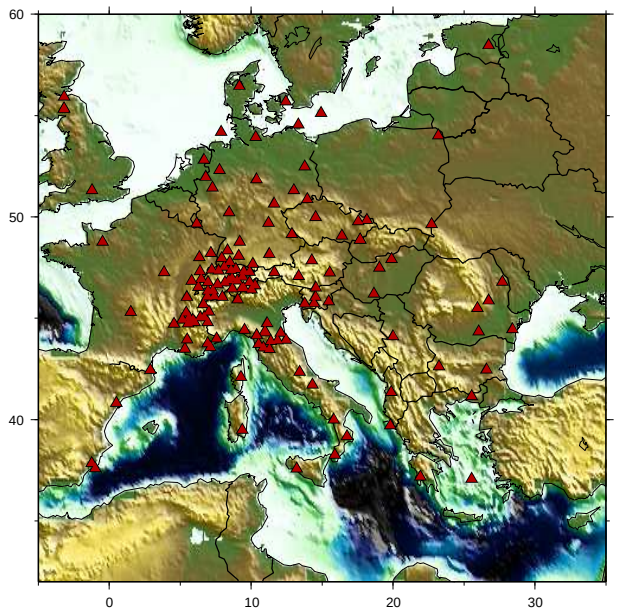

FIG. 8.1: Map showing the location of broadband recorders used for this study.

per day. First the 24-hour records are decimated to 1 Hz and the instrument responses are deconvolved ; then the spectrum of the records are whitened between 5 and 150s.

For each station pair, North and East horizontal components were rotated in the direction of the inter-station azimuth to provide radial (R) and transverse (T) components of energy propagating directly along the great circle connecting the two stations. We then correlated signals recorded on the components that correspond to the surface wave term of the Green's function day by day. The vertical and radial components were correlated in all 4 possible combinations (ZZ corresponding to a cross-correlation of both vertical components (Z), RR corresponding to both radial components, and both RZ and ZR corresponding to one radial and one vertical component each) to retrieve the Rayleigh wave Green's function ; the TT (correlation of both transverse components) correlation yields the Love wave Green's function. Correlations of one-day records are then stacked. This is equivalent to directly cross-correlating the whole year of records. Note that compared to other studies (*Shapiro and Campillo* (2004); *Sabra et al.* (2005c); *Shapiro et al.* (2005); *Yao et al.* (2006); *Yang et al.* (2007)), no amplitude normalization was applied prior to the correlation.

8.1.1 Exemple of AIGLE-STU

Figure 8.2 shows the ZZ cross correlation of one year of records between the Swiss Digital Seismic Network (SDSNet) stations AIGLE and STU, band-passed into several

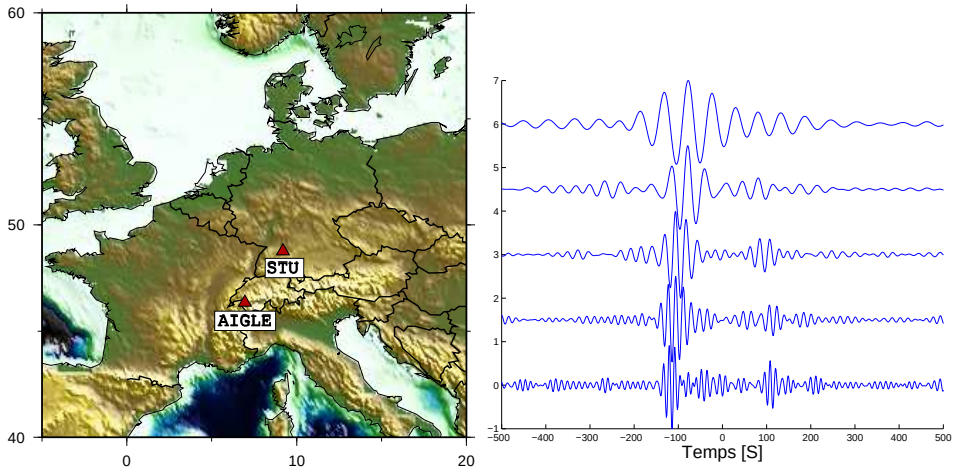

FIG. 8.2: Cross-correlation of one year of records between AIGLE STU bandpassed in several period bands from 10 to 60s.

period bands from 10s to 60s. The inter station distance is 320 Km. The positive time of the correlation corresponds to the causal Green's function of the medium between AIGLE and STU, and the negative time corresponds to its anticausal counterpart (ie the Green's function between STU and AIGLE). A wave train corresponding to Rayleigh waves is clearly visible on all period bands in the positive and negative correlation time at 100s. This corresponds to a velocity of $3.2km/s$. Dispersion is evident with high-frequency waves arriving after low-frequency ones. In practice, correlations are generally not perfectly symmetric. In this example, the amplitude of the Rayleigh waves is larger for negative than for the postive time, although the phase arrival times are equal. This indicates that during the year 2004-2005 more energy propagated from STU to AIGLE than from AIGLE to STU. As most of stations record three component signals, we were able to retrieve Rayleigh waves by correlating the vertical and radial components (ZZ, RR, ZR, and RZ). Figure 8.3a shows the correlations corresponding to Rayleigh waves for the AIGLE-STU path bandpassed in the 10 to 20s period band. The waveforms are similar and the arrival times are the same for all traces. Similarly, Love waves are clearly visible on TT correlations (figure 8.3b).

8.2 2D Inversion

8.2.1 Selection of the paths

Rayleigh and Love wave dispersion curves are evaluated from the emerging Green's functions using frequency-time analysis (*Levshin et al.* (1989); *Ritzwoller and Levshin* (1998)) for the 12,000 inter-station paths. For each path we measure eight possible

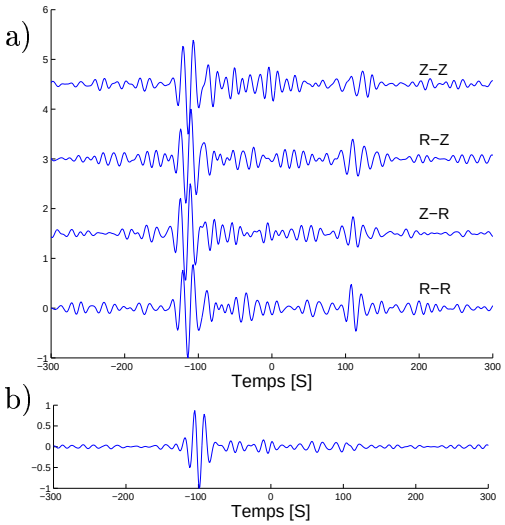

FIG. 8.3: Cross-correlation of one year of records between AIGLE and STU bandpassed in the 10-20s period band a) Rayleigh waves obtained from ZZ, RZ, ZR and RR correlation b) Loves waves obtained from TT correlation.

Rayleigh wave dispersion curves by considering four components of the correlation tensor (ZZ, RR, RZ and ZR) and both the positive and the negative part of the noise correlation function. Similarly, we get two estimates of Love-wave dispersion curves from the positive and negative parts of TT correlations.

To be selected for use in our dispersion analysis, correlations must meet several criteria. We define signal to noise ratio as the ratio of the amplitude of the Rayleigh (or Love) wave and the variance of the noise following Rayleigh (or Love) waves. More precisely, the variance of the noise is evaluated in a time window that start at arrival times corresponding to a velocity of $1km.s^{-1}$, and finish at 4000 seconds (ie if the inter station distance is 300 km, the standard deviation of the noise is evaluated in a time windows from 300s to 4000s). The signal to noise ratio is measured separately on the positive and negative correlation time at the discrete period at which we compute a group velocity map.

For Rayleigh waves we reject waveforms with a signal to noise ration ≤ 7. This threshold was chosen to maximize the number of high-quality measurements in the dataset. Furthermore we keep only measurements with a difference of group velocity evaluated on the positive and negative correlation time $< 5\%$ in either the Z-Z,R-R,R-Z, or Z-R correlation. The retained measurement are then averaged to get the final velocity.

As often Love wave emerge only in one side of the correlation, and as they are only visible on T-T correlation, we cannot use this procedure for Love waves. Instead, we keep only group velocity measurement performed on waveforms whose signal to noise

ratio is $\geq$ 10. If this condition is met simultaneously in the positive and negative correlation time, we average the group velocity measured on the two side of the correlation.

We further reject records with inter-station distances less than 2 wavelengths for both Rayleigh and Love waves.

At 5s, using these criteria we selected 3300 Rayleigh wave observations from the initial 12000 station pairs (Fig. 8.4). Using a 25x25 km parameterization of central Europe, we achieve a path density of more that reaches 150 paths per cell in Switzerland (Figure 8.4b). We obtain similar path densities at period up to 40s. Above 40s, the number of paths tends to decrease, and we choose to use a grid of 50x50 Km instead. At 60s, we selected 2100 paths resulting in a density of more than 120 paths per cells in Switzerland.

8.2.2 Inversion method

We invert our dispersion measurements to obtain group velocity maps. The standard forward problem can be written in tensor notation :

$$\boldsymbol{d} = \boldsymbol{G}\boldsymbol{m} \tag{8.1}$$

$\boldsymbol{d} = \boldsymbol{t}^{meas} - \boldsymbol{t}^{o}$ is the data vector whose elements are the difference between the measured velocity and the velocity computed from the initial model for each path. $\boldsymbol{G}$ is the matrix ds/co, which represent for each path and for each cell of the initial model the travel time of Rayleigh wave. $\boldsymbol{m} = (c - co)/c$ is the group velocity map we want to determine, c being the velocity obtained after inversion, and co the initial Rayleigh wave velocity.

We inverted the described dataset following *Barmin et al.* (2001) to obtain group velocity maps on a 100×100 = 10,000 cells of 25×25 km across Europe (Fig. 8.4). As described by *Barmin et al.* (2001), the solution model $\boldsymbol{m}$ minimizes the penality function

$$(\boldsymbol{G}(\boldsymbol{m}) - \boldsymbol{d})^T(\boldsymbol{G}(\boldsymbol{m}) - \boldsymbol{d}) + \alpha^2||\boldsymbol{F}(\boldsymbol{m})||^2 + \beta^2||\boldsymbol{H}(\boldsymbol{m})||^2 \tag{8.2}$$

i.e., a linear combination of the data misfit, the final model smoothness, and the magnitude of the perturbation. The second term, $\boldsymbol{F}$, is the gaussian spatial smoothing operator :

$$F(\boldsymbol{m}) = m(\boldsymbol{r}) - \int_S K_o exp\left(-\frac{|r - r'|^2}{2\sigma^2}\right) m(\boldsymbol{r}' d\boldsymbol{r}') \tag{8.3}$$

The last term $\boldsymbol{H}$ limits the magnitude of the perturbation in areas with low path density. With this scheme, the inverted model fades progressively into the initial model.

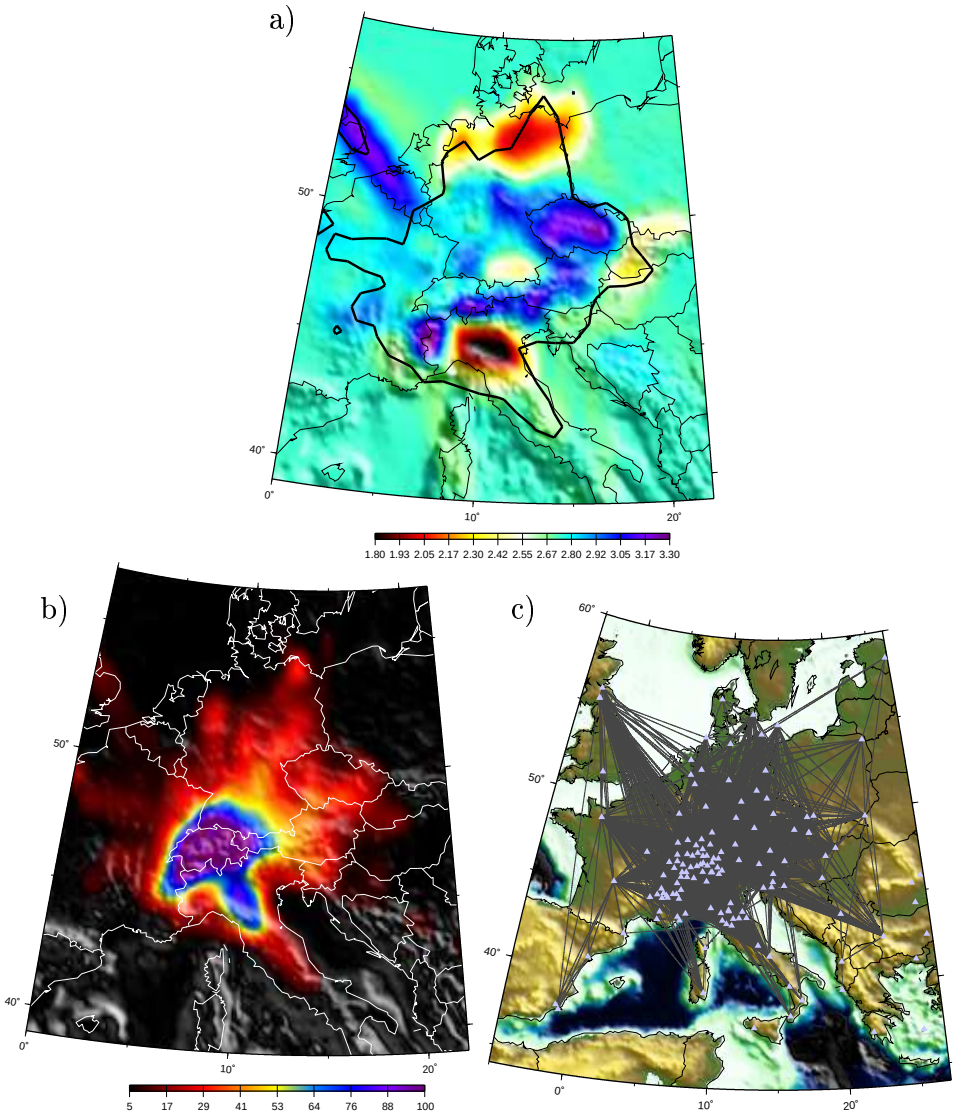

FIG. 8.4: a) Group velocity map for Rayleigh wave at 5s period. The black line delimits the area where at least 10 paths are crossing each cell. b) Map showing the number of paths crossing each cell for the 5s Rayleigh paths. c) 3400 paths where reliable group velocity measurement were obtained for 5s Rayleigh waves.

Three regularization parameters are chosen manually prior to the inversion : α and β determine respectively the weight that is given to the spatial smoothing and to the dependence of the perturbation magnitude with the path density. σ is the correlation length, it controls the width of the spatial smoothing kernel. Because of the dense path coverage we found the results are not sensitive to the choice of β in the region of highest data density (the central and western Alps and southern Germany). The correlation length σ was chosen equal to 25 km at period between 5 and 40s, and equal to 50 km for period above 50s. To choose the value of α, we computed 'trade-off' curves : After performing numerous inversions with different values of α, a measure of the misfit of each solution to the model to the data is plotted against α. The resulting trade-off curve, sometimes called 'L curve', has the shape of a decreasing exponential, resembling to the character L : A high value of α gives over damped models that cannot fit the data, whereas low value of α result in models fitting perfectly the data but which are not spatially smooth. The transition between the two extreme kinds of model is abrupt, and we keep the models close to the corner of the 'L-curve'.

8.2.3 Rayleigh and Love Wave Group Velocity Maps

Group velocity maps are computed in two steps. 1) A first overdamped model including all selected paths is computed. The difference of the measured travel time and the travel time predicted by the inverted model is computed for each path. We discard all paths where this time difference exceeds twice the average difference. 2) We compute the final group velocities map on a 25*25 km grid across Europe. No a priori information is used since the initial model is homogeneous.

Figure 8.4a shows the obtained group velocity maps for 5s Rayleigh waves. At this period, Rayleigh waves are mostly sensitive to shear velocities in the upper crust (3 to 7 km). Velocity anomalies correlate well with geological units. Low velocity regions are shown in red and black and generally correspond to sedimentary basins. The Po basin is clearly visible as well as are the North Sea basin and the Mollasse Basin. High velocity areas shown in blue and purple correspond to the crystalline crust of the Alps and Bohemian Massif.

Computed group velocties map for Rayleigh and Loves waves at period 8s, 16s and 35s are shown on Figure 8.5. At 8s surface waves are mostly sensitive to the upper crust (5-8 Km). The Alpine arc is associated with high velocities that can reach $3.2km.s^{-1}$ as well as the Bohemian Massif. At 16s, surface waves are sensitive to the mid crust. The main structures visible on the 8s map are still visible, but in addition the French Jura is visible with high velocities reaching $3km.s^{-1}$.

At 35s (Figure 8.5c), group velocities are sensitive to the crustal thickness : in region where the crust is thin, surface waves high mantellic velocities, whereas in region where the crust is thick they are associated with slower crustal velocities. The 35s

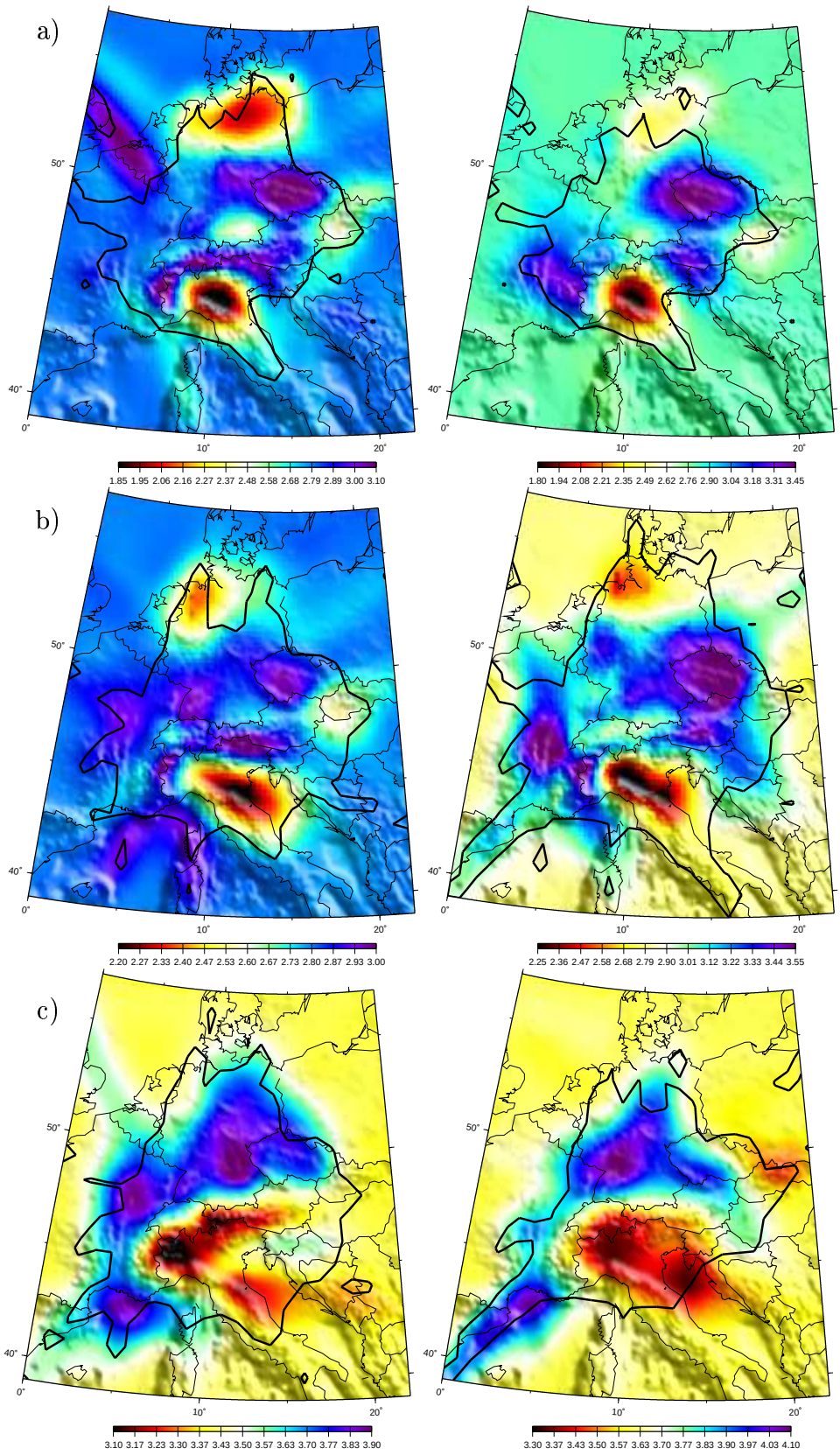

FIG. 8.5: Rayeigh (left) and Love (right column) group velocity maps at a)8s b)16s c)35s.

group velocities maps shows a great contrast between area of "normal" crust thickness (Germany, central France, with high velocities), and areas where the crust is particulary thick (e.g. the Alps with a low low velocity that indicates a crustal root).

8.2.4 Resolution of Group Velocity Maps

The resolution of the group velocitiy maps depends mostly on the density of paths and on their azimuthal distribution (crossing paths). In our case, these two parameters depend on the geometry of the network and on the distribution of the noise sources that can limit the number of available paths for some directions. The resolution is estimated from resolution matrices, that are computed during the inversion as described by *Barmin et al.* (2001). Each row of the resolution matrix is a map representing the resolution for one cell of the model. It quantifies how the obtained group velocities at one node depend on the measurements performed at others nodes.

We define the resolution length at each node of the model as the distance for which the value in the matrix resolution has decrease by a factor 2. The resolution length is not expected to depends on the azimuth : the measurements obtained at one node depend on the measurements performed at adjacent nodes, with no preferential direction. However, because of the heterogeneous distribution of the stations as well as the uneven distribution of the noise sources, in our case the shape of the resolution surface is elliptical : the resolution is actually better in the southeast direction than in the northeast one (Figure 8.7).

At each node of the model, we measure the resolution length in direction corresponding to the direction of maximum and minimum resolution. By averaging these two values we define the average value of the resolution. Figure 8.6a shows the average resolution for the 5s Rayleigh group velocity map in the area where we have at least 5 paths per cell. Maximum resolution is in Switzerland where the path density is the highest. In this area, and using this definition we obtain a nominal resolution of 25-30 km. Peripheral to the central Alps (Soutern Germany, eastern Austria, south-east France), the average resolution varies between 40 and 65 km. Outside this area the resolution is about 70 to 90 km.

Figures 8.7a and b show respectively the directions of maximum and minimum resolution, respectively, and the value of the resolution. Two main factors explain that the resolution depends on the azimuth : i) The noise recorded in Europe is dominated by noise coming from the Northern Atlantic ocean. The quality of the Green functions reconstruction is better for path oriented towards the Northern Atlantic Ocean, than in the perpendicular direction. ii) The correlation converge more easily towards the Green function for short paths than for long paths.

As a result in area such as Germany where the inter station distance is large, we have

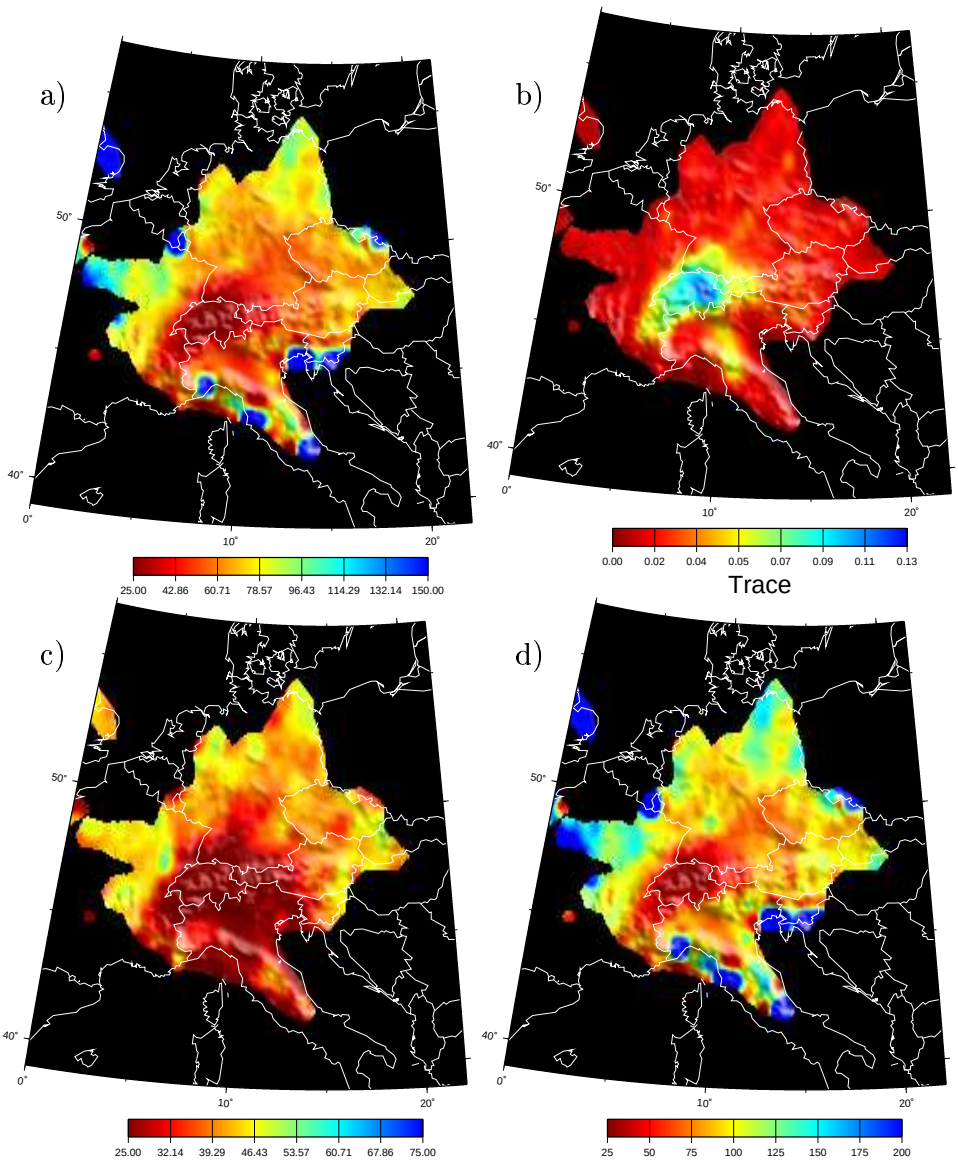

FIG. 8.6: a) Isotropic resolution b) Trace of the resolution matrix c) Value of the Resolution in the best direction d) Value of the resolution in the worst direction

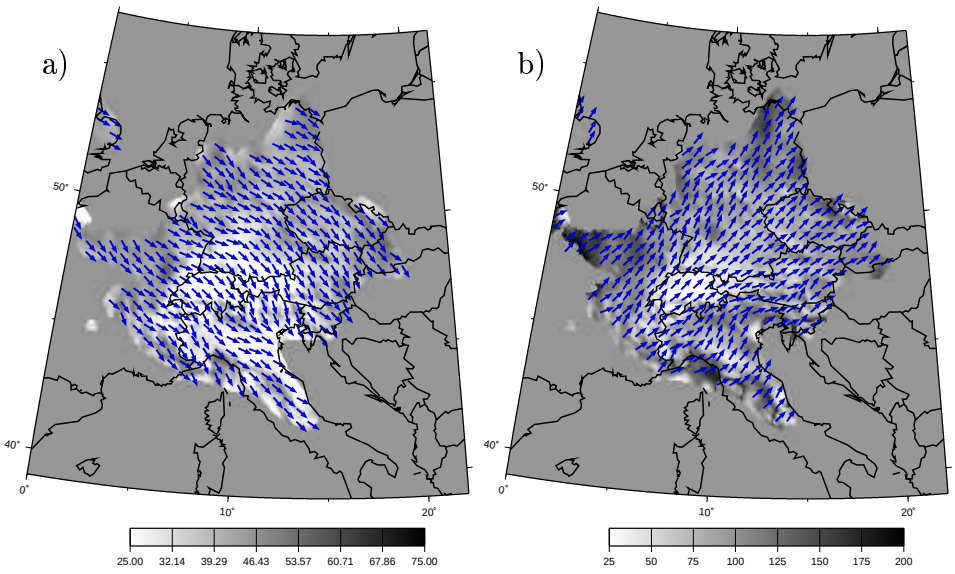

FIG. 8.7: a) Azimuth for which the resolution of the 5s Rayleigh group velocity map is the best. The color scale indicates the value of the resolution length for this direction. b) idem for the direction where the resolution is the lowest.

more reliable group velocities measurements for path oriented towards the Northern Atlantic Ocean than in other directions. The resolution is about twice better in the South-East direction (40-45 km) than in the North East direction (75-125 Km). In Switzerland we have an higher path density, the inter station distance is much lower than in other areas. In this context, the convergence of the correlation towards the Green function depends less on the azimuth, and the resolution is almost isotropic (i.e. we have the same value in the best and worst direction). This observation was made for the period band from 5-60s.

8.3 3D Inversion

8.3.1 Method

Group velocity maps provide information about laterally varying surface wave velocities with respect to the period. From each cell of the model we extract the period-dependent velocities of Rayleigh waves from all the computed group velocities maps (5s, 8s, 12s, 16s, 18s, 20s, 25s, 30s, 35s, 40s, 50s, 60s, 70s, 80s), obtaining one dispersion curve for each cell. We did not include Love waves since we found that Rayleigh wave dispersion curve are more reliable. Actually, Rayleigh group velocities measurements were selected using both a signal to noise ration and a time symmetry criteria,

whereas Loves waves were selected only depending on their signal to noise ratio (see section 8.2.1).

Each dispersion curve (one per cell) is inverted to obtain the corresponding S-wave profile. To better constrain crustal thickness, we look specifically for a 3 layer model (sedimentary layer, inferior crust, crust/mantle boundary). We use a non-linear Monte Carlo inversion with two iterations. In the first step of the inversion, we conduct a non-linear search over much of the model space. We allow both the S velocity and the depth of each interface to vary, and we tolerate large misfit values. The initial model is chosen with a Moho depth of 30 Km, and an lower crust limit at 15 Km. Since our shortest period observations are at 5s, we cannot constrain the thickness of the sedimentary upper crust. We use the sedimentary thickness provided by Crust2.0 (http ://mahi.ucsd.edu/Gabi/rem.html) for the initial model. Since this model has a resolution of 1° and our model is discretized in 25km pixels, we allow the thickness of the sedimentary layer to vary ±1km during the inversion.

In the second step, we use the model with the lowest misfit from the first step as the "new" initial model. Because we emphasize locating the crust-mantle boundary, we allow the S-wave velocity to vary only by ±0.1 km.s in each layer, but we allow for larger changes in layer thickness. We impose only that the Moho depth is between 20 and 60km, and that the sedimentary layer is less than 5 km. As the solution of the inversion is non unique, we keep the 10 best models.

8.3.2 Exemple of S-wave profile

Figure 8.8 shows three examples of S velocity profiles obtained at three nodes of our model corresponding to diverse geological settings, the Po plain, the Austrian Alps, and southern Germany. For each example, we show group velocity in the right panel with black dots and the dispersion curve associated with the 10 best Vs profiles in solid lines on the left panel. For all the examples, we were able to model Vs profiles which fit the measured dispersion curves. Although the inversions provide non-unique solutions, the depth of Moho in the series of chosen models varies only slightly.

We found in Southern Germany a Moho depth of about 30 Km, that corresponds to a standard crust (Figure 8.8d). In the Austrian Alps (Figure 8.8c), the thickening of the crust is clearly visible, with a Moho depth of 45 km. In the Po Plain, all the selected inverted models show a similar sedimentary layer at 2.5 km, and a Moho depth of 33 km.

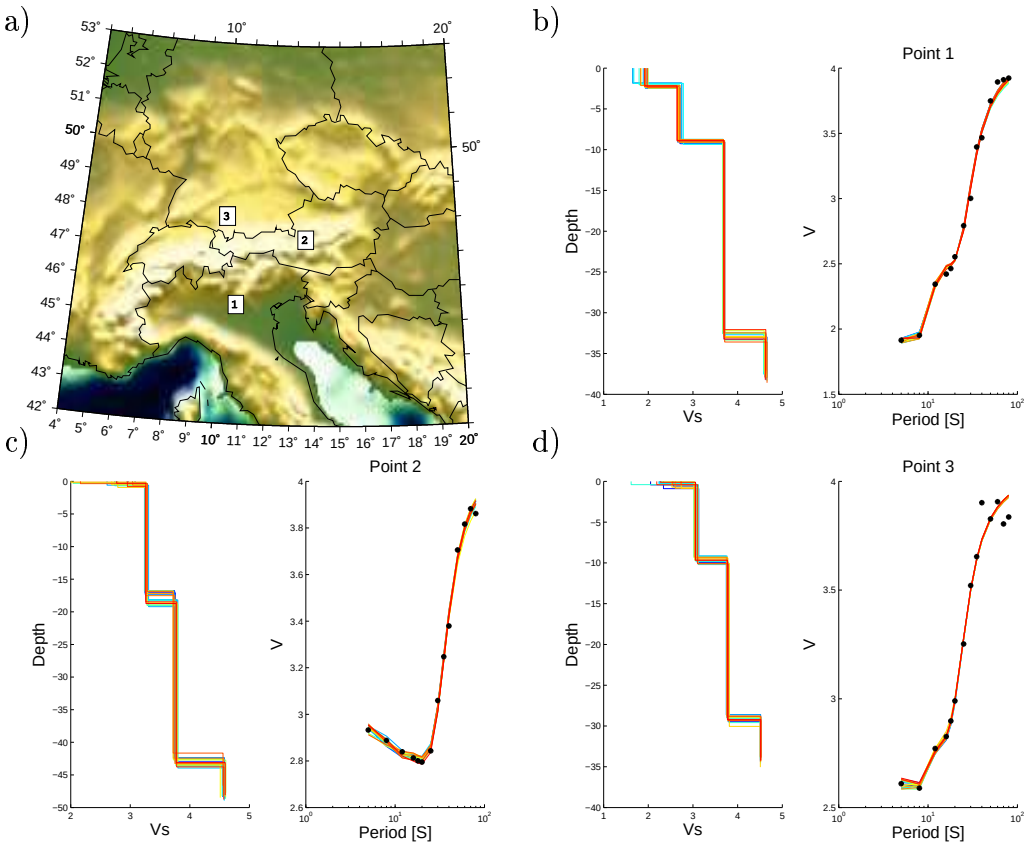

FIG. 8.8: a) Map showing the location where we present S-wave profile obtained after inverting Rayleigh wave dispersion curves. b) c) d) Inversion of Rayleigh wave dispersion curve into S wave profile at 3 cells respectively in the Po Plain, Austrian Alps, and Southern Germany. The right panel shows the measured Rayleigh waves dispersion curves (black dots) and the dispersion curves associated with 10 best Vs Profiles shown in solid lines on the left panel.

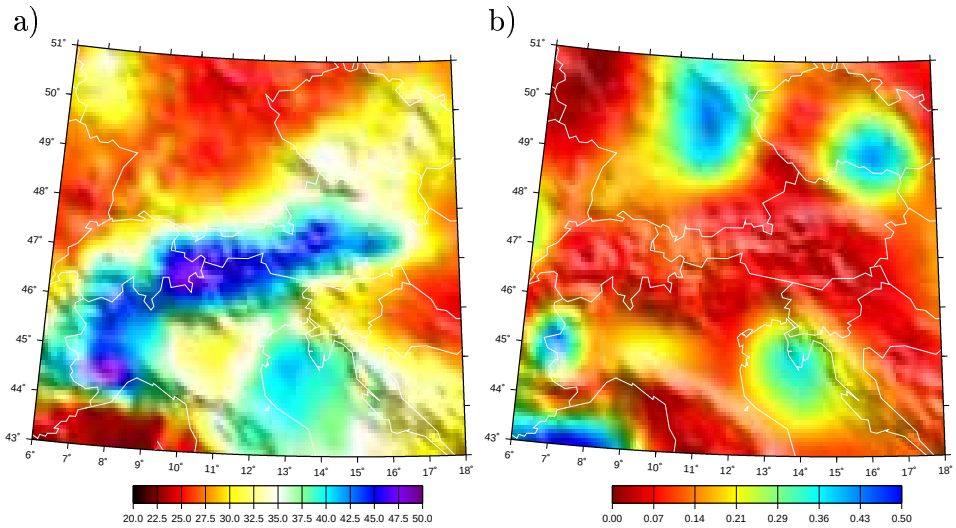

FIG. 8.9: a)Map of the Moho depth b) Misfit of the Inversion.

8.3.3 Moho map

Figures 8.9a and 8.10 show the inverted depth of the Moho at each cell of the model. Note that no spatial smoothing was used during the 3D inversion. The results obtained at each cell are spatially consistent. The Moho topography varies between 25 and 55 Km, and is divided into two main parts : European Moho and Adriatic Moho. The boundary separating the two provinces corresponds to the southern terminus of the Alpine crustal thickening.

A third unit, the Ligurian Moho, is located at the southernmost part of the studied region. The main features of the Moho topography are explained by the triple-junction between these 3 units. The European lower crust is subducting southward under the shallower north-dipping Adriatic Moho. At the same time, the Adriatic lower crust is subducting southward beneath the Ligurian Moho. The Adriatic Moho, compressed between the European Moho in the North and the Ligurian Moho in the south, is elevated beneath the northern Po Plain (46N,11E). The central and western Bohemian Massif is characterized by a relatively flat Moho at around 28km. The transition from the average Moho of the Bohemian Massif and the thick crust of the Alpine region is very sharp and outlines the geometry of Alpine subduction. We find the Moho depth varying between 30 and 55 km within the Alps with maximum crustal thickness in southwestern Switzerland and south of the France-Italian border close to the Ivrea Zone.

The misfit of the inversion is shown in Figure 8.9b. Misfit of the model and measured data (< 0.7) within the central and western Alps is remarkably low. The model is characterized by higher misfit north of the Alps where have a lower path density.

8.3.4 Comparison with other studies

The Alpine region has been studied intensively using controlled source and earthquake tomography. These studies provide insight into the crustal and upper mantle velocity structure (*Marchant and Stampfli*, 1996; *Waldhauser et al.*, 1998, 2002; *Bleibinhaus and Gebrande*, 2005; *Thouvenot et al.*, 2002; *Paul et al.*, 2001; *Marone et al.*, 2004, and references therein). *Dèzes and Ziegler* (2001) presented a Moho map of Europe resulting from the compilation of several seismological and gravimectric studies. The overall shape of their Moho map matches our results at locations where we have a high density of data coverage (southern Germany, Switzerland and Austria). However, we tend to obtain a thinner crust in germany. We found a Moho depth of 26-27 km, where it is usually believed to be deeper :28-30 Km. Our Moho model within the alpine orogenic root is strikingly similar to the one obtained by *Waldhauser et al.* (1998). That study relied on published seismic reflection and refraction data of about 250 profiles across the Alpine region. They determined the simplest geometrical configuration of the Moho consistent with this data set. Their Moho map within the Alpine arc shows an overall good agreement with our result (Figure 8.10).

Although our results shares the same main charactestics there are two noticeable difference : 1) we were not able to image the Ivrea body (the Ivrea body is assumed to be a mantellic body with a small lateral extent)and 2) *Waldhauser et al.* (1998) shows a fluctuation within the Adriatic plate at the southern most part of their model. However we believe these differences are mostly due to our poor path coverage in these two areas.

8.4 Conclusion

We used one year of records at 150 three components broadband European stations. We retrieved the Rayleigh and Love wave Green functions by correlating the noise records between all station pairs. We selected the best waveforms using a signal to noise and a time symmetry criteria. We obtained about 3500 reliable Rayleigh and Love waves group velocities measurements at period below 50s, and about 2000 measurements at period above 50s. We used these measurements to perform a Rayleigh and Love waves tomography at period ranging from 5s to 80s using a 25x25 Km grid below 50s. The resulting group velocities map shows numerous geological units.

At each cell of our model, we extracted Rayleigh waves dispersion curves from our group velocities map, and invert them using a two step Monte Carlo algorithm in order to determine the depth of the Moho in the Western Alps (Switzerland, Austria, southern Germany). Our results shows clearly the thickening of the moho below the Alpine crust. Our moho map shares striking similarities with the previous model of

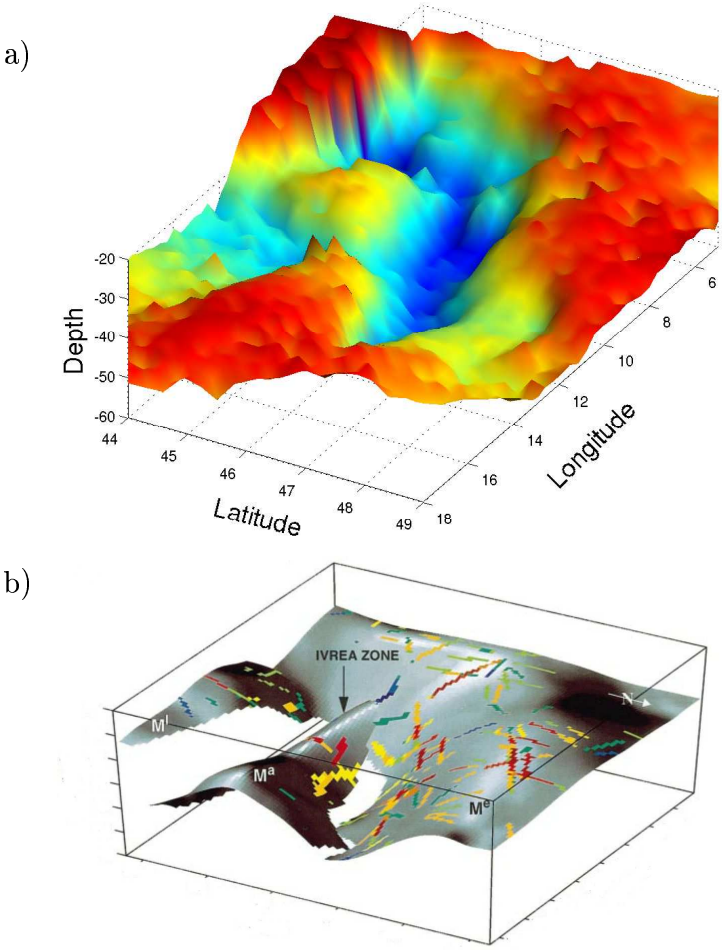

FIG. 8.10: 3D view of the Moho depth a) from our results b) From Waldhauser et al (Geophysical Journal International, 1998) .

Waldhauser et al. (1998) in region where we have a high density of paths. This proves that the earth seismic noise can be efficiently used to obtain high resolution Love and Rayleigh group velocities map at period up to 80s that can be used for crustal and lithospheric 3D imaging.

8.5 Acknowledgements

All the seismic data used in this study have been obtained from from the IRIS DMC (http ://www.iris.edu/), the ORFEUS database (http ://www.orfeus-eu.org/), the ETH Zürich, and the Commissariat à l'Energie Atomique (CEA, France).

This research has been supported by the Commissariat à l'Energie Atomique (CEA, France), and by the European Community (project Neries).

Chapitre 9

Corrélations de coda de corrélations

Sommaire

9.1 Introduction

Dans le chapitre précédent nous avons vu que les corrélations de bruit pouvaient être utilisées efficacement pour imager la croûte terrestre depuis des profondeurs de quelques kilomètres jusqu'au Moho.

Théoriquement la fonction de Green complète entre n'importe quelle couple de stations peut-être reconstruite par les corrélations. En pratique, la directivité du bruit impose des limitations : 1) Lors de notre étude sur les Alpes, nous n'avons utilisé que 3000 à 4000 trajets sur les 12000 trajets initiaux, soit environ 1 trajet sur 3. Sur les autres, les ondes de surface n'ont pas un rapport signal/bruit suffisant ou alors les vitesses mesurées sur les temps positifs et négatifs diffèrent. 2) Seul le mode fondamental des ondes de surface est clairement visible sur les corrélations. Ainsi les études se servant des corrélations de bruit pour faire de la tomographie n'exploitent que les ondes de Rayleigh (*Shapiro et al.* (2005); *Sabra et al.* (2005c); *Pedersen et al.* (2006); *Yao et al.* (2006); *Yang et al.* (2007)). Il y a toutefois une exception : *Roux et al.*

(2005) ont pu identifier des ondes P sur des corrélations réalisées à Parkfield pour des trajets courts $< 10\ km$ (ce travail est présenté dans l'annexe du présent manuscrit).

Nous souhaitons aller au-delà de ces limitations. Pour ce faire nous nous servons des ondes de la coda. Sur un enregistrement de séisme, les ondes constituant la coda sont les arrivées tardives visibles après les ondes de surface. Il a été démontré que la coda est formée d'ondes émises lors de tremblements de terre et diffusées par les hétérogénéités de la croûte terrestre (*Aki and Chouet* (1975); *Aki and Richards* (1980); *Sato and Fehler* (1998)). Ainsi la coda tardive est un champ diffus ; la décroissance exponentielle de son amplitude peut-être modélisée par le transfert radiatif (*Abubakirov and Gusev* (1990); *Hoshiba* (1991); *Margerin et al.* (1998, 1999)), et le rapport d'énergie entre les ondes P et S tend vers une constante qui ne dépend que du milieu, et pas de la source (*Hennino et al.* (2001)). Il est donc également possible de corréler la coda générée par un même séisme entre deux stations A et B afin de mesurer la fonction de Green du milieu. C'est la démarche qu'ont suivi *Campillo and Paul* (2003) : en corrélant des enregistrements de coda issues 101 séismes entre des stations situées au Mexique et séparées par quelques dizaines de kilomètres, ils ont pu montrer que les corrélations de coda permettaient de retrouver des fonctions de Green du milieu.

Dans ce chapitre nous employons la même démarche, sauf qu'au lieu de considérer la coda issue de séismes nous utilisons la coda provenant de corrélations de bruit. Dans un premier temps nous décrivons la façon dont nous avons mis en oeuvre cette méthode. Dans un second temps nous comparons les corrélations de coda avec les corrélations de bruit. Enfin nous présentons un exemple où les corrélations de corrélations ont permis de retrouver la fonction de Green causale et acausale du milieu, tandis que la corrélation de bruit ne laisse apparaître que la fonction de Green causale.

9.2 Méthode

Pour tester les corrélations de coda, nous utilisons le même jeu de données que celui utilisé au chapitre précédent portant sur la tomographie des Alpes. Nous utilisons 150 stations large bande en Europe, dont la répartition est particulièrement dense en Suisse. Chaque station dispose d'un an d'enregistrement entre octobre 2004 et octobre 2005.

Soient A et B deux stations fixes et C_i l'ensemble des autres stations du réseau. Notre objectif est de reconstruire la fonction de Green entre A et B. Nous procédons en deux étapes. Tout d'abord, nous corrélons le bruit de fond entre A et B d'une part, et l'ensemble des stations C_i d'autres part. Les corrélations de bruit sont effectuées de la même manière qu'au chapitre précédent :

– Les enregistrements de bruit sont tout d'abord corrigés de la réponse instrumentale.

- Le spectre des enregistrements est blanchi entre 5 et 150s de période.
- Les données sont corrélées jour par jour, puis l'ensemble des corrélations journalières est sommé pour obtenir le résultat final.

Une fois les corrélations de bruit calculées sur l'ensemble des trajets C_iA et C_iB, nous passons à l'étape suivante. Il s'agit pour chaque station C de corréler la coda des corrélations CA et CB. Nous fenêtrons la coda dans les temps positifs et négatifs des corrélations de bruit en considérant qu'elle débute à un temps correspondant au double du temps d'arrivée des ondes de Rayleigh et dure 1200s. Pour chaque station C nous effectuons alors 4 corrélations (en corrélant la coda des temps positifs des corrélations de bruit calculées sur les trajets CA et CB, puis celle des temps négatifs ainsi que les corrélations croisées). Nous répétons cette opération avec l'ensemble des stations C_i, et sommons l'ensemble des corrélations ainsi effectuées. Nos obtenons ainsi le résultat final, qui en théorie, est la fonction de Green entre A et B.

9.3 Un exemple de corrélation de coda de corrélations : EMV-GIMEL

La figure 9.1 présente la fonction de Green entre les stations EMV et GIMEL obtenue à partir de corrélations de corrélations selon la méthode décrite au paragraphe précédent. Les stations C_i ayant servi sont indiquées sur la carte par des étoiles jaunes. Environ 100 stations ont été utilisées[1]. Nous montrons en bleu la corrélation de corrélations et en rouge la corrélation de bruit pour deux bandes de périodes : 5-10s (en bas) et 10-20s (en haut). Les ondes de Rayleigh émergent clairement sur les temps positifs et négatifs des corrélations. Leurs temps d'arrivée est de 30s. La distance interstation étant de 72 km, ceci correspond à une vitesse de 2.3 $Km.s^{-1}$, en accord avec notre modèle de vitesse (cf chapitre précédent). Nous constatons que la fonction de Green obtenue en corrélant directement le bruit entre EMV et GIMEL et celle en corrélant les codas de corrélations sont quasi identiques : leurs formes d'ondes sont superposables, et leurs temps d'arrivée similaires. Il est à noter que les durées du signal utilisé pour la corrélation sont sans commune mesure : environ une journée (1200 secondes * 100 stations) pour la corrélation de corrélations et 365 jours pour la corrélation de bruit.

Cet excellent accord indique que les corrélations de corrélations permettent effectivement de retrouver des fonctions de Green. Ceci prouve en outre que la coda est reconstruite par les corrélations de bruit. C'est donc bien à la fois la partie "balistique"

[1]Les stations trop éloignées, trop proches ou n'ayant pas assez de données n'ont pas été utilisées. Ainsi bien que disposant de 150 stations, nous nous sommes servis pour cet exemple que de 100 stations.

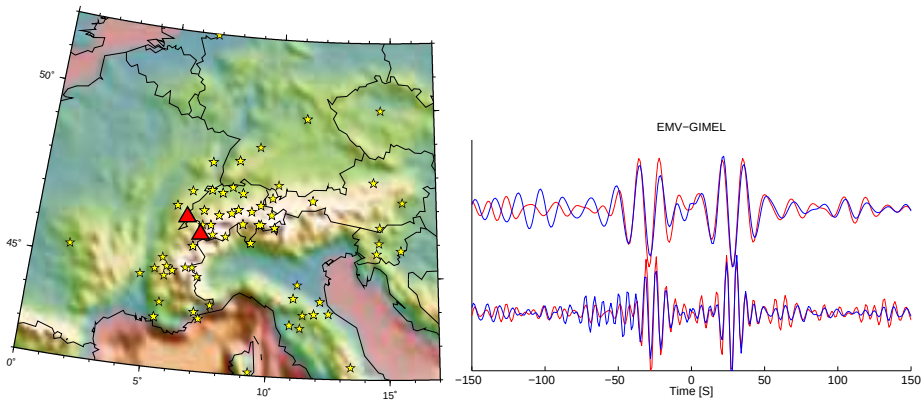

FIG. 9.1: Fonction de Green entre EMV et GIMEL (triangle rouge sur la carte), obtenue en corrélant un an de bruit (rouge) et en corrélant des codas de corrélations de bruit (bleu). Nous montrons deux bandes de période : 5-10s (en bas) et 10-20s (en haut). Les stations ayant servies pour les corrélations de coda sont indiquées par les étoiles jaunes sur la carte.

et diffuse de la fonction de Green que l'on mesure via les corrélations de bruit.

9.4 Hodochrones

La figure 9.2 présente deux autres trajets. Sur les trajets courts - inférieurs à 100 km - ce sont essentiellement les ondes de Rayleigh entre 5 et 20s qui émergent des corrélations de corrélations. C'est le cas par exemple pour le trajet DIX-RSL pour lequel la distance interstation est de 74 Km (figure 9.2b). En augmentant la distance interstation, les corrélations se dégradent entre 5 et 10s, mais commencent à converger vers la fonction de Green entre 20 et 40s de période. Ainsi sur le trajet FUSIO-UBR (175 km, figure 9.2c), les ondes de Rayleigh sont clairement visibles sur les corrélations de corrélations pour les bandes de période 10-20s et 20-40s. Le très bon accord entre corrélation de bruit et corrélation de corrélations indique que la fonction de Green est bien reconstruite.

Des exemples d'hodochrones réalisés à partir de corrélations de coda de corrélations de bruit, sont présentés sur la figure 9.3 pour les 3 bandes de période 5-10s, 10-20s et 20-40s. Pour chaque bande de période, nous ne montrons que les corrélations dont le rapport signal sur bruit des temps positifs est supérieur à 10 ; le rapport signal/bruit étant défini ici comme le rapport de l'amplitude des ondes de Rayleigh et de la déviation standard des fluctuations précédant et suivant l'onde de Rayleigh. Sur les 1200 trajets testés, 67 ont été sélectionnées entre 5-10s, 228 entre 10-20s, et 233 entre 20 et 40s. Ces chiffres peuvent sembler relativement faibles, mais il faut garder à l'esprit que les corrélations de corrélations ne peuvent être efficaces qu'au

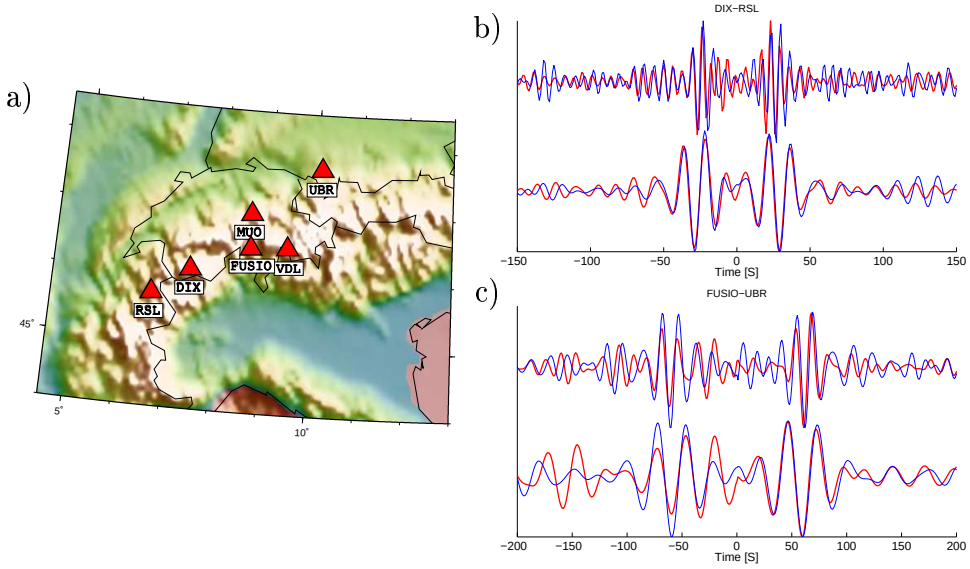

FIG. 9.2: a) Carte indiquant les stations entre lesquelles nous reconstruisons les fonction de Green. b) c) Exemples de fonction de Green reconstruites en corrélant des corrélations (bleu) et en corrélant du bruit (rouge) pour les trajets DIX-RSL et FUSIO-UBR. Nous montrons deux bandes de période (5-10s et 10-20s pour (b), 10-20s et 20-40s pour (c)).

milieu du réseau afin que la moyenne sur les stations C_i soit effective.

9.5 Peut-on gagner de l'information en corrélant des coda de corrélations au lieu de corréler le bruit directement ?

Le trajet MUO-VDL (figure 9.4) est intéressant : entre 5-10s la fonction de Green émergeant de la corrélation de corrélations est symétrique, on distingue les ondes de Rayleigh sur les temps positifs et négatifs avec une même amplitude. Ce n'est pas le cas de la corrélation de bruit qui ne laisse apparaître les ondes de Rayleigh que sur les temps positifs. Pour cette raison, lors de notre étude sur les Alpes présentée au chapitre précédent, ce trajet n'a pas été sélectionné pour les périodes inférieures à 10s. Par contre la corrélation de corrélations aurait été sélectionnée du fait de sa symétrie. Ainsi les corrélations de corrélations pourraient permettre à l'avenir de mesurer la vitesse de groupe des ondes de surface là où les corrélations de bruit ont échoué. En augmentant la couverture spatiale de nos mesures, cela pourrait permettre d'améliorer la résolution de la tomographie basée sur le bruit sismique.

On peut toutefois se demander comment est-il possible que les corrélations de corréla-

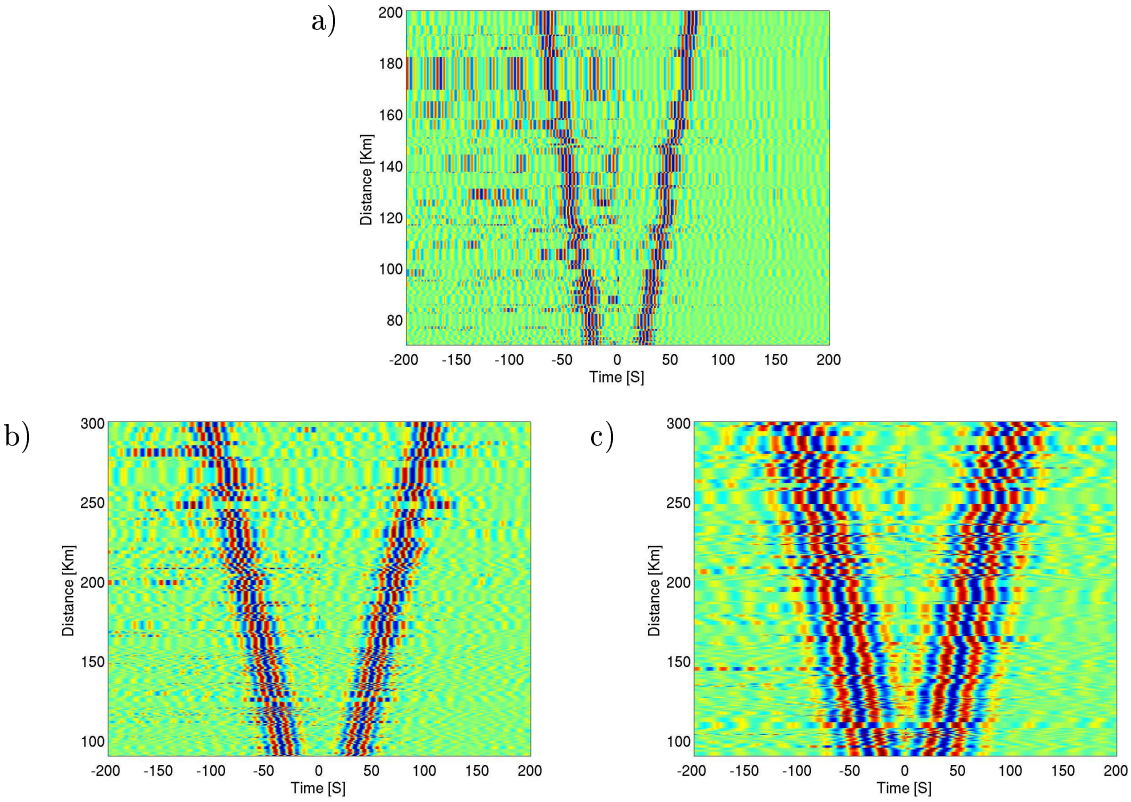

FIG. 9.3: Corrélations de coda de corrélations en fonction de la distance pour les bandes de périodes a) 5-10s b) 10-20s et c) 20-40s.

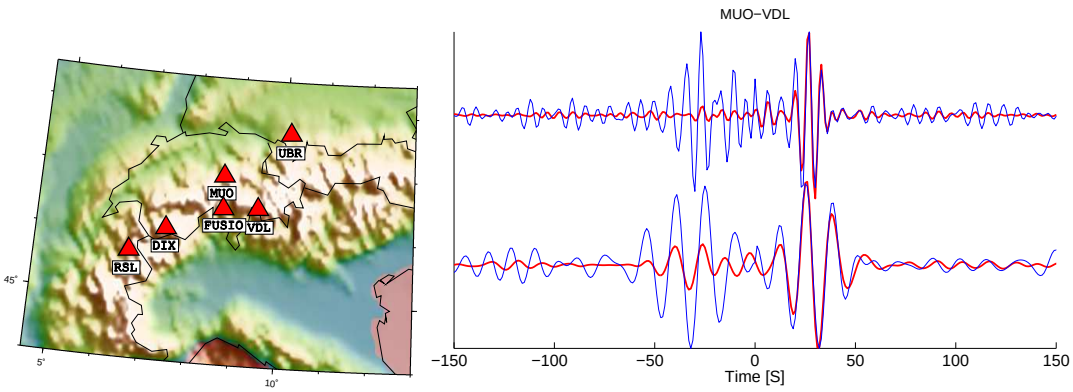

FIG. 9.4: Fonction de Green entre MUO et VDL obtenue en corrélant un an de bruit (rouge) et en corrélant les corrélations de bruit (bleu). Nous montrons deux bandes de période : 5-10s (en haut) et 10-20s (en bas).

tions puissent être symétriques sans que les corrélations de bruit le soient ? Autrement dit, pourquoi les corrélations de corrélations de contiendraient-elles plus d'informations que les corrélations de bruit ?

Si les sources de bruit étaient distribuées de façon homogène dans tout l'espace, la corrélation du champ entre deux points contiendrait la fonction de Green causale et acausale du milieu (voir chapitre 3 équation 3.13, et le chapitre 5 section 5.4). La propagation des ondes étant réciproque[2], celles-ci sont identiques. Les corrélations devraient donc avoir une même amplitude dans les temps positifs et négatifs. En pratique selon les azimuts et les bandes de fréquences considérées, les corrélations sont asymétriques (cf figure 5.4). Ceci est une conséquence de la distribution non homogène des sources de bruit qui implique que le flux d'énergie est plus important dans certaines directions que dans d'autres.

La coda est constituée d'ondes diffusées par le milieu. La diffusion permet d'homogénéiser le champ et de le rendre plus isotrope. Ainsi *Paul et al.* (2005) ont montré que les corrélations de coda de séismes permettaient de reconstruire des fonctions de Green. Toutefois, lorsque le début de la coda est utilisé les corrélations sont très asymétriques du fait de la distribution inhomogène des séismes utilisés, la diffusion n'ayant pas encore été suffisante pour rendre le champ totalement isotrope. Au contraire en utilisant la coda tardive la symétrie des corrélations augmente. Il y a ainsi une progression depuis le début de la coda qui correspond à un régime diffusion simple jusqu'à la coda lointaine qui tend à être un champ équipartitionné (*Hennino et al.* (2001)) du fait de la diffusion multiple. Ainsi lorsque nous corrélons les corrélations de bruit en fenêtrant la coda de la fonction de Green, nous utilisons spécifiquement les ondes diffusées par le milieu, qui constituent un champ plus isotrope que le bruit sismique. Ainsi les corrélations de coda de corrélations sont pour certains trajets plus symétriques que les corrélations de bruit (figure 9.4).

Il peut toutefois paraître surprenant que l'on puisse corréler la coda des corrélations alors qu'elle n'est pas clairement visible sur les corrélations et que son amplitude est plus faible que celle des ondes de Rayleigh directes. Le faible rapport signal/bruit de la coda illustre qu'en pratique les corrélations de bruit ne convergent pas de manière parfaite vers la fonction de Green. En effet, les corrélations obtenues consistent en la fonction de Green à laquelle il faut ajouter des fluctuations résiduelles. Ces fluctuations résultent à la fois de la durée limitée du calcul de la corrélation et de la distribution imparfaite des sources de bruit. Celle-ci implique que du bruit ne se propageant pas entre les stations A et B mais allant d'une source de bruit S vers A et de S vers B se retrouve également sur la corrélation entre A et B. Idéalement, si la source de bruit était un bruit blanc réparti dans tout le milieu et si on corrélait un signal de duré infini, ces fluctuations tendraient vers 0. En pratique elles demeurent d'un niveau suffisant pour empêcher d'identifier des phases de faibles amplitudes de

[2]La réciprocité signifie qu'il n'y pas de différence entre l'enregistrement en A d'une source en B et l'enregistrement en B d'une source en A

la fonction de Green, comme les ondes de la coda.

Ainsi la coda reconstruite en corrélant du bruit est la somme de deux signaux : la coda "réelle" faisant partie de la fonction de Green du milieu et des fluctuations résiduelles. Lorsque l'on corrèle la coda des corrélations de bruit entre des stations $C - A$ et $C - B$, et que l'on moyenne le résultat sur un ensemble de stations C_i, on tend à éliminer la contribution des fluctuations résiduelles, ces dernières étant différentes pour chaque trajet. On amplifie ainsi la part du signal consistant effectivement en la coda de la fonction de Green. Cette procédure améliore doublement le caractère aléatoire du champ d'ondes utilisé : par la distribution des sources virtuelles (C_i) et par la minimisation des effets des corrélations temporelles du bruit initial. On parvient ainsi à compenser la directivité du bruit de fond. Ceci nous permet de mesurer des fonctions de Green là où les corrélations de bruit ont échoué.

9.6 Conclusion

L'objet de ce travail préliminaire était de voir si les corrélations de bruit permettaient ou non de reconstruire la coda, et si celle-ci pouvait être à son tour corrélée pour évaluer des fonctions de Green.

Nous avons vu que les corrélations de coda de corrélations permettaient effectivement de mesurer la vitesse des ondes de surface entre des couples de stations distantes de moins de 300 km sur une gamme de période allant de 5 à 40s. Ce succès est une preuve indirecte que la coda émerge lors des corrélations de bruit.

Le potentiel des corrélations de corrélations en terme de tomographie reste encore à cerner précisément. Sur certains trajets tels que MUO-VDL (figure 9.4), elles permettent d'évaluer la fonction de Green causale et acausale alors que les corrélations de bruit sont asymétriques. En effet en corrélant les codas de corrélations nous mettons spécifiquement à contribution la partie diffuse du champ. Ceci permet de compenser la directivité spatiale du bruit et ainsi de reconstruire la fonction de Green entre 2 points sans qu'il y ait de sources alignées avec ces derniers.

Dans l'avenir, les corrélations de corrélations permettront d'augmenter significativement le nombre de trajets pour lesquels nous pourrons mesurer la vitesse de propagation des ondes de surface. La qualité des fonctions de Green ainsi obtenues dépend directement de la densité de stations : plus le réseau est dense, plus il possible de moyenner les corrélations. Ainsi il existe probablement une "masse critique" de stations au delà de laquelle les corrélations de coda permettraient de compenser de façon efficace la directivité du bruit de fond sismique.

Conclusion et perspectives

Cette thèse avait pour but de voir dans quelle mesure le bruit de fond sismique pouvait être utilisé en sismologie. D'un point de vue théorique, les corrélations de bruit permettent de connaître la fonction de Green entre n'importe quel couple de points d'un milieu quelconque, à condition que le bruit respecte la condition d'équipartition. Ceci signifie que tous les modes du milieu sont excités avec un même niveau d'énergie et une phase aléatoire. Dans ce cas le champ d'ondes dans un milieu homogène peut-être vu comme la superposition d'ondes planes de phase et d'amplitude aléatoire se propageant dans toute les directions de l'espace. Un tel champ est isotrope, le flux d'énergie en chaque point est nul, ce qui constitue la limite aux temps longs d'un champ diffus.

La première étape consistait à voir si le bruit de fond sismique respectait ces exigences ou non. En étudiant l'amplitude des corrélations en fonction de l'azimut, nous avons mis en évidence que les caractéristiques du bruit dépendent de la bande de fréquence considérée. Entre 5 et 10s de période, le bruit est généré localement le long des côtes tout au long de l'année. Au contraire entre 10 et 20s le bruit est global : l'ensemble des réseaux aux USA, en Europe et en Tanzanie perçoivent du bruit provenant des mêmes régions, situées dans l'hémisphère nord en hiver, et de l'hémisphère sud en été. Ainsi entre 5 et 10s, le bruit de fond ne peut pas être considéré comme isotrope, le flux d'énergie est plus important dans certaines directions (vers la côte) que dans d'autres. Au contraire entre 10 et 20s, moyenné sur un an, le bruit de fond est plus homogène, sans être toutefois complètement isotrope.

Ces résultats nous ont naturellement amenés à nous poser la question suivante : dans quelle mesure la directivité du bruit affecte-t-elle les corrélations de bruit ? Quelle est la précision des mesures de vitesse déduites des corrélations ? L'analyse de 11 ans de données continues enregistrées par 3 stations californiennes nous a permis d'aborder ces questions. Nous avons montré qu'en dépit de la directivité du bruit, les mesures de vitesse d'onde de surface sont stables au cours du temps, les variations du temps d'arrivée observées ne représentant que 0.3% du temps total de propagation. En utilisant des corrélations d'un mois, les mesures sont suffisamment précises pour identifier des dérives d'horloge brèves dans le temps d'amplitudes supérieures à 0.5s. En moyennant les mesures sur des temps plus longs, nous avons pu mettre en évidence

des erreurs instrumentales se produisant sur plusieurs années, de l'ordre du dixième de seconde.

Ces résultats laissent présager des applications futures. Les corrélations de bruit pourraient être utilisées de façon routinière pour détecter et corriger les dérives d'horloge de stations. Lors de notre étude nous avons considéré des stations séparées par des distances de l'ordre de 150 km. En considérant des distances plus petites on favorise la convergence des corrélations vers la fonction de Green ce qui améliore la précision des mesures. Ainsi en déployant des réseaux denses au voisinage de failles ou sur des volcans, les corrélations de bruit pourraient permettre de mettre en évidence des changements dans le milieu. Ainsi *Brenguier et al.* (2007b) ont pu imager le conduit volcanique du piton de la fournaise à partir de bruit de fond, puis montrer que le volcan se déformait peu avant les éruptions *Brenguier et al.* (2007a).

L'étape suivante de notre travail a été d'étudier les Alpes. Les corrélations d'un an de bruit entre 150 stations large bande réparties dans toute l'Europe, nous ont permis de mesurer les vitesses de groupe des ondes de Love et de Rayleigh sur plus de 3000 trajets, sur une gamme de période allant de 5 à 80s. Ces mesures ont permis d'obtenir des cartes de vitesse de groupe entre 5 et 80s. Les courbes de dispersion extraites en chaque point du modèle ont été inversées pour obtenir un modèle du Moho sous les Alpes. Celui-ci partage les mêmes caractéristiques principales que ceux déterminés par des études précédentes à partir de sismique active, notamment celle de *Waldhauser et al.* (1998). Cependant la méthode employée diffère radicalement : nous n'avons utilisé qu'un an de données et un traitement relativement simple sans a priori sur la structure. Par contraste le modèle de *Waldhauser et al.* (1998) est un modèle interprétatif obtenu en compilant les résultats de 250 profils sismiques réalisés au cours des 30 dernières années. Ainsi pour peu de disposer d'un réseau suffisamment dense, il est possible de déterminer un modèle de croûte réaliste. Ceci est particulièrement important pour les études de tomographie globale, afin de distinguer dans les modèles de Terre globale quelle est la part des différences entre les temps d'arrivée mesurés et prédits dues à la croûte et au manteau supérieur.

Il reste encore de nombreuses questions ouvertes. La directivité du bruit impose plusieurs limitations. La plus importante est qu'il est difficile de reconstruire des fonctions de Green dans certaines directions. Ainsi lors de notre étude sur les Alpes nous n'avons pu utiliser qu'un trajet sur trois environ. Il sera peut-être possible de palier au moins partiellement ce problème en corrélant les codas reconstruites par les corrélations de bruit entre elles afin de mesurer les fonctions de Green, sur des trajets pour lesquelles les corrélations de bruit ne donnent pas de résultat. Corréler les codas de corrélations, plutôt que le bruit directement est en effet une manière de mettre à contribution spécifiquement la partie diffuse du champ.

Dans nos études nous nous sommes servis des corrélations pour mesurer la vitesse de groupe du mode fondamental des ondes de Love et de Rayleigh. Est-il possible de

mesurer une vitesse de phase avec précision ? L'amplitude peut-elle être également exploitée ? D'autre mode de propagation émergent-ils des corrélations ? Sera t-il possible d'utiliser le bruit généré par les atmosphères de Mars ou de Vénus pour étudier la structure de ces planètes ? Nombre de questions restent posées.

Cinquième partie

Appendice

Chapitre 10

Cross-correlation of random fields : mathematical approach and applications

P. Gouédard, L. Stehly, F. Brenguier, M. Campillo, Y. Colin de Verdière, E. Larose, L. Margerin, P. Roux, F. J. Sánchez-Sesma, N. M. Shapiro, R. L. Weaver

Article soumis à *Geophysical Prospecting*

Sommaire

10.1 abstract

Random field cross-correlation is a new promising technique for seismic exploration, as it bypasses shortcomings of usual active methods. Seismic noise can be considered as a reproducible, stationary in time, natural source. In the present paper we show why and how cross-correlation of noise records can be used for geophysical imaging. We discuss the theoretical conditions required to observe the emergence of the Green's functions between two receivers from the cross-correlation of noise records. We present examples of seismic imaging using reconstructed surface waves from regional to local scales. We also show an application using body waves extracted from records of a small-scale network. We then introduce a new way to achieve surface wave seismic experiments using cross-correlation of unsynchronized sources. At a laboratory scale, we demonstrate that body wave extraction may also be used to image buried scatterers. These works show the feasibility of passive imaging from noise cross-correlation at different scales.

10.2 Introduction

Traditional observational methods in seismology are based on earthquake records which results in two main shortcomings :

1) Most techniques are based on waves emitted by earthquakes that occurred only in geologically active areas, mainly plate boundaries. This results in a limited resolution in all other areas where earthquakes are not present. In particular, at stations far away from the source region, all the high-frequency information is lost due to the attenuation of the medium.

2) The occurrence of earthquakes is too low, preventing study of real time change of active structures such as volcanoes or faults.

In the case of active seismic at smaller scales, the resolution is limited by the number and power of sources. It is thus difficult to image large areas or deep structures. Furthermore, controlled sources are difficult to carry out on hardly accessible places, like at the ocean bottom, where passive imaging could be much more convenient. For time-lapse monitoring, reproducible sources are necessary. This is very difficult to achieve for surveys of long duration, whereas noise wavefields may be stationary on those time scales.

Here we explore an alternative way of probing the Earth's interior using noise records only. The main idea is to consider seismic noise as a random source field when averaged over long time series. In this particular case, cross-correlation between two stations yields the Green's function between these two points. As the seismic noise is mainly

generated by atmospheric and oceanic forcing at the Earth's surface, the surface wave part of the Green's function is mostly extracted from the cross-correlation process.

At smaller scales, the same principle can be applied to study local structures. In this case, higher frequencies are used. At those frequencies, the wavefield is believed to be governed by local sources, which are unlikely to have the expected properties of randomness. This has to be taken into account in the processing.

In this paper, the theoretical relationship between noise cross-correlation and the Green's function is first discussed in section 10.3, based on theoretical derivations from (*Colin de Verdière*, 2006a,b). Several applications are then presented, from large to small scales, using noise wavefields of different origin and physical properties : surface wave tomography at the regional scale in Western Europe (section 10.4) and at a more local scale in section 10.5 at the 'Piton de la Fournaise' volcano (*Brenguier et al.*, 2007b) ; local P-waves extraction in the Parkfield network at the San Andreas Fault (*Roux et al.*, 2005a) in section 10.6 ; site characterization using surface waves extracted from noise cross-correlation (*Gouédard et al.*, 2006) in section 10.7 ; passive imaging of a buried scatterer at laboratory scale (*Larose et al.*, 2006a) in section 10.8.

10.3 Background and mathematical approach

10.3.1 Historical background

The Green's function of a medium between two points A and B represents the record we would get at A if an impulsive source is applied at B.

In the case of a completely random wavefield, the cross-correlation of signals recorded between two points converges to the complete Green's function of the medium, including all reflection, scattering and propagation modes (*Weaver*, 2005). To demonstrate this result and to define more precisely under which assumption it is valid, various experimental, numerical and theoretical approaches have been developed.

Historically speaking, helioseismology was the first field where ambient-noise cross-correlation performed from recordings of the Sun's surface random motion was used to retrieve time-distance information on the solar surface (*Duvall et al.*, 1993; *Gilles et al.*, 1997). The idea of day-light imaging was proposed by *Claerbout* (1968) in the context of prospecting. More recently, a seminal paper was published by *Weaver and Lobkis* (2001) that showed how diffuse thermal noise recorded and cross-correlated at two transducers fastened to one face of an aluminium sample provided the complete Green's function between these two points. They theoretically interpreted this result by invoking equipartitioning of the modes excited in the aluminium sample.

This result was generalized to the case where randomization is not produced by the distribution of sources, but is provided by multiple scattering that takes place in heterogeneous media (*Lobkis and Weaver*, 2001b).

The use of a spectral representation (*Lobkis and Weaver*, 2001b), the fluctuation-dissipation approach (*Weaver and Lobkis*, 2001, 2003; *van Tiggelen*, 2003; *Godin*, 2007) or a correlation-type representation theorem (e.g. *Wapenaar*, 2004) are rigorous theoretical approaches to interpret experimental results.

Experimental evidences demonstrated the feasibility of passive imaging in 1) acoustics (*Lobkis and Weaver*, 2001b; *Weaver and Lobkis*, 2001; *Larose et al.*, 2004a), 2) seismology where *Campillo and Paul* (2003) retrieve the Green's function between two seismic stations from a collection of earthquakes, and 3) oceanography in shallow underwater acoustics where both direct and reflected wavefronts were retrieved from ambient-noise cross-correlation (*Roux and Kuperman*, 2004; *Sabra et al.*, 2005e). By summing the contributions of all sources to the correlation, it has been shown numerically that the correlation contains the causal and acausal Green's function of the medium (*Wapenaar*, 2004). Cases of non-reciprocal (e.g., in the presence of a flow) or inelastic media have also been theoretically investigated (*Wapenaar*, 2006; *Godin*, 2007).

Derode et al. (2003a,b) proposed to interpret the Green's function reconstruction in terms of a time-reversal analogy and showed that correlation of multiply scattered waves could be used for passive imaging in acoustics. The convergence of the noise correlation function towards the Green's function in an unbounded medium can also be interpreted through the stationary phase theorem (*Snieder*, 2004; *Roux et al.*, 2005b).

In seismology, *Aki* (1957) proposed a long time ago to use seismic noise to retrieve the dispersion properties of surface waves in the subsoil. *Shapiro and Campillo* (2004) reconstructed the surface wave part of the Green's function by correlating seismic noise at stations separated by distances of hundreds to thousands of kilometers, and measured their dispersion curves at periods ranging from 5 to about 150 seconds. This method led to the first application of passive seismic imaging in California (*Shapiro et al.*, 2005; *Sabra et al.*, 2005c) with a much greater spatial accuracy than for usual active techniques. *Larose et al.* (2005) also used noise cross-correlation at small distances on the moon.

For the problem of elastic waves, it has been theoretically shown that the convergence of noise correlation to the Green's function was bonded by the equipartition condition of the different components of the elastic field (*Sánchez-Sesma et al.*, 2006a,b). In other words, the emergence of the Green's function is effective after a sufficient self-averaging process that is provided by random spatial distribution of the noise sources when considering long time series as well as scattering (*Campillo*, 2006; *Larose et al.*,

2006b).

10.3.2 The case of homogeneously distributed white noise sources

The scope of this section is to summarize the different theoretical approaches using mathematical tools that allow a global view of the correlation problem in any propagation medium. We will see that cross-correlation of noise recorded at two distant stations A and B yields the Green's function, assuming that the wavefield is a white noise distributed everywhere in the medium, with no assumption about the medium.

We consider any medium X, that does not need to be homogeneous, where the wave propagation equation is controlled by a damped equation that can be written as :

$$\frac{\partial^2 u}{\partial t^2} + 2\,a\,\frac{\partial u}{\partial t} - L\,u = f \tag{10.1}$$

Here $a > 0$ is a constant that corresponds to the attenuation of the medium, $f(t,\vec{r})$ is the source field (i.e., the noise field in our case) and $u(t,\vec{r})$ denotes the displacement field. If $L = c^2(\vec{r})\,\Delta$, we recognize the usual wave equation. In a more general calculation, L can be any negative self-adjoint elliptic differential operator. In more physical terms, L is an operator which preserves energy.

First of all we will introduce a definition of the Green's function in the frequency domain using the *integral kernel* of the operator L, and show that this definition is equivalent to the usual one. Then, by expressing the displacement field using the Green's function, we will calculate the cross-correlation and find how the derivative of the cross-correlation function is linked to the Green's function.

We introduce the integral kernel of an operator P, denoted by $[\![P]\!](x,y)$ by :

$$\forall u : X \longmapsto \mathbb{R}^3,\ \big(P\,u\big)(x) = \int_X [\![P]\!](x,y)\,u(y)\,dy$$

This is the 'continuous matrix' of the operator P. It has to be linked to the case of a finite space where one can define the matrix (P_{ij}) of P and write the following formula :

$$\forall u : X \longmapsto \mathbb{R}^3,\ \big(P\,u\big)_i = \sum_j P_{ij}\,u_j$$

We first consider a medium without attenuation, i.e., $a = 0$ in Eq. 10.1. Let us define the Green's function of L in the frequency domain, denoted $\hat{G}(\omega + i\,\varepsilon, \vec{r}, \vec{r}_s)$, with ε a small positive value, as the opposite of the integral kernel of $\big((\omega + i\,\varepsilon)^2 + L\big)^{-1}$.

In other words, $\hat{G}$ is the *resolvent* of L evaluated at point $(\omega + i\,\varepsilon)^2$. The $\hat{\cdot}$ denotes a function defined in the Fourier space. ε ensures that $\big((\omega+i\,\varepsilon)^2+L\big)$ is invertible as L has real eigenvalues. We will show that this mathematical definition of $\hat{G}$ is the same as the usual one, which is the causal solution of the wave equation (Eq. 10.1) when the source function f is a Dirac impulse in time and space $\delta(t, \vec{r}-\vec{r}_s)$. The Green's function $\hat{G}(\omega + i\,\varepsilon, \vec{r}, \vec{r}_s)$ admits a limit as $\varepsilon \to 0^+$, denoted $\hat{G}(\omega + i0, \vec{r}, \vec{r}_s)$, as a Schwartz distribution on the real axis. If L has a continuous spectrum, this limit is a smooth function (the 'limiting absorption principle'). $\hat{G}$ can thus be written as :

$$\begin{aligned}
\hat{G}(\omega + i0, \vec{r}, \vec{r}_s) &= -\left[\!\left[\big((\omega + i0)^2 + L\big)^{-1}\right]\!\right](\vec{r}, \vec{r}_s) \\
&= -\int_X \left[\!\left[\big((\omega + i0)^2 + L\big)^{-1}\right]\!\right](\vec{r}, \vec{r}\,') \, \delta(\vec{r}\,' - \vec{r}_s)\, d\vec{r}\,' \\
&= -\big((\omega + i0)^2 + L\big)^{-1} \delta(\vec{r} - \vec{r}_s)
\end{aligned}$$

which yields :

$$-\big((\omega + i0)^2 + L\big)\, \hat{G}(\omega + i0, \vec{r}, \vec{r}_s) = \delta(\vec{r} - \vec{r}_s)$$

The inverse Fourier transform of this equation gives a relation that is the usual definition of G in the case of a medium without attenuation :

$$\frac{\partial^2 G}{\partial t^2}(t, \vec{r}, \vec{r}_s) - L\, G(t, \vec{r}, \vec{r}_s) = \delta(t)\, \delta(\vec{r} - \vec{r}_s)$$

G is thus the solution of Eq. 10.1 in the case of an impulsive source in time and space. One can compute the inverse Fourier transform of $\hat{G}(\omega + i\varepsilon, x, y)$ using residue calculus, and take the limit as ε goes to 0 to get

$$G(t, \vec{r}, \vec{r}_s) = Y(t) \left[\!\!\left[\frac{\sin t\sqrt{-L}}{\sqrt{-L}} \right]\!\!\right](\vec{r}, \vec{r}_s)$$

where Y is the Heaviside-step function, and where we denote $\sqrt{-L}$ the operator which eigenvalues are the images of the eigenvalues of L by the function $x \mapsto \sqrt{-x}$ (idem for the sinus function).

If we consider an attenuating medium, the Green's function $\hat{G}_a(\omega, \vec{r}, \vec{r}_s)$ is defined by the resolvent of L evaluated at point $\omega^2 + 2\,i\,a\,\omega$ instead of $(\omega + i0)^2$. It thus becomes

$$G_a(t, \vec{r}, \vec{r}_s) = Y(t)\, e^{-a\,t} \left[\!\!\left[\frac{\sin t\sqrt{-L - a^2}}{\sqrt{-L - a^2}} \right]\!\!\right](\vec{r}, \vec{r}_s) \tag{10.2}$$

We now define the time domain cross-correlation between the displacement at two points A and B as :

$$C(\tau, \vec{r}_A, \vec{r}_B) = \lim_{T \to +\infty} \frac{1}{T} \int_0^T u(t, \vec{r}_A)\, \overline{u(t+\tau, \vec{r}_B)}\, dt \tag{10.3}$$

where the bar denotes the conjugate. $u(t,\vec{r})$ can be expressed using the Green's function G_a (here attenuation is necessary to ensure convergence of the integral, see *Roux et al.* (2005b)) and the source function f as follows :

$$u(t,\vec{r}) = \int_0^\infty dt' \int_X G_a(t',\vec{r},\vec{r}_s)\, f(t-t',\vec{r}_s)\, d\vec{r}_s$$

We assume that f is a white noise distributed everywhere in the medium X, acting at any time t. In the frequency domain, a white noise contains all the frequencies with a random phase. In the time domain, this is a random wavefield such that the position and the activation time of each source are uncorrelated. In this case, and considering a damping medium, we replace the large T limit in the correlation by an ensemble average. We then get the following explicit expression for the correlation between the wavefields recorded at A and B (see appendix 10.10 for mathematical details) :

$$C(\tau,\vec{r}_A,\vec{r}_B) = \frac{\sigma^2\, e^{-a\,|\tau|}}{4\,a} \left[\!\!\left[\big(-L\big)^{-1} \left(\cos\tau\sqrt{-L-a^2} + a\,\frac{\sin|\tau|\sqrt{-L-a^2}}{\sqrt{-L-a^2}} \right) \right]\!\!\right] (\vec{r}_A,\vec{r}_B) \tag{10.4}$$

where σ is the variance of the noise wavefield.

The time derivative of this equation is expressed in terms of the Green's function using (10.2), giving the more familiar expression :

$$\frac{d}{d\tau}\, C(\tau,\vec{r}_A,\vec{r}_B) = \frac{-\sigma^2}{4\,a} \big(G_a(\tau,\vec{r}_A,\vec{r}_B) - G_a(-\tau,\vec{r}_A,\vec{r}_B) \big) \tag{10.5}$$

This means that for any medium, the time-derivative of the cross-correlation computed between the wavefields recorded at two stations A and B is the Green's function of the medium, provided that the damping coefficient is small enough and that noise sources behave as white noise acting everywhere in the medium. This is the same hypothesis as stated in *Roux et al.* (2005b), *Lobkis and Weaver* (2001b) and others, but L is now an arbitrary negative definite elliptic operator, and so the present result is more general.

10.3.3 The case of a scattering medium

The previous calculation was made using sources randomly located anywhere and randomly active at any time. This is a very strong hypothesis that is not valid in practical cases. Another demonstration of the link between cross-correlations and Green's functions can be made without any assumption about the noise sources location or their activation time. We only assume that there is equipartition at the boundaries of the

region of interest, which means that each eigenmode is excited with the same level of energy.

A simple view of the relation between equipartition and correlation is given by the reconstruction of the Green's function of the homogeneous space using the azimuthal averaging of the correlation of plane waves, which are the eigenfunctions of the problem. *Sánchez-Sesma and Campillo* (2006) consider an isotropic distribution of P and S plane waves in an elastic medium. They found that the azimuthal average of the cross-correlation of motion between two points is proportional to the imaginary part of the exact Green's tensor between these points under the condition that the energy ratio S/P of the incident waves is the one predicted by equipartition. These results clearly show that equipartition is a necessary condition to retrieve the exact Green's function from correlations of the elastic field. In practice, one has to deal with complex media for which the eigenfunctions are unknown and therefore for which equipartition conditions cannot be explicitly specified in terms of local properties of the field.

Sánchez-Sesma et al. (2006a) discussed a particular case. They consider the field in the vicinity of a cylindrical scatterer embedded in an homogeneous space and illuminated isotropically with incident P and S plane waves in the ratio of equipartition of the homogeneous space. Taking into account the scattered waves, they show that the azimuthal average of cross-correlations of motion between two points still yields the imaginary part of the exact Green's tensor of the heterogeneous medium, including the scattered waves, even at close distance from the scatterer. Is such a property still valid for any scattered or type of heterogeneity ? What are the conditions required for the incident field ? *Weaver and Lobkis* (2004) used an integral representation approach to study the problem of an heterogeneous region in an open medium. The essence of this property is expressed in the spectral theory of scattering that shows that the properties obtained in the simplest case of an homogeneous medium are formally valid in presence of heterogeneities. This is discussed in *Colin de Verdière* (2006a,b) as follows.

In a first step we will define the *spectral projector* and exhibit its expression using the cross-correlation function (Eq. 10.7). In a second step, will prove the relation between this projector and the Green's function, the so-called Stone formula (Eq. 10.8).

We denote $e_0(\vec{r},\vec{k}) = e^{i\,\vec{k}\cdot\vec{r}}$ the plane waves that are the eigenmodes of the homogeneous infinite space. In the case of a complex medium, the scattering theory (*Ramm*, 1986; *Reed and Simon*, 1978) tells us that, if the medium is heterogeneous only in a finite region, the eigenmodes in the whole space can be written as :

$$e(\vec{r},\vec{k}) = e_0(\vec{r},\vec{k}) + e_s(\vec{r},\vec{k})$$

where e_s, the scattered waves, satisfies the so-called *Sommerfeld radiation* condition,

which ensures that e_s will vanish when $\vec{r}$ goes to infinity. This decomposition is still valid in the near field of the scatterers (i.e., inside the heterogeneous region).

For $I \subset \mathbb{R}_+$, we define the spectral projector of L on I, denoted P_I, from its integral kernel $[\![P_I]\!]$ at any points $\vec{r}_1$ and $\vec{r}_2$ of X by :

$$[\![P_I]\!](\vec{r}_1, \vec{r}_2) = (2\,\pi)^{-d} \int_{\lambda_k \in I} e(\vec{r}_1, \vec{k})\, \overline{e(\vec{r}_2, \vec{k})}\, |d^d \vec{k}| \tag{10.6}$$

where d is the dimension of the space and λ_k denotes the eigenvalue associated with the eigenfunction $e(\vec{r}, \vec{k})$. This is the projector on the sub-eigenspaces of L which eigenvalues are in I. Again, what P_I represents can be easily understood in the case of a finite number N of eigenvalues $\{\lambda_n\}$, where we can write :

$$[\![P_I]\!](\vec{r}_1, \vec{r}_2) = \sum_{\substack{n \in [1,N] \\ \lambda_n \in I}} e_i(\vec{r}_1)\, \overline{e_n(\vec{r}_2)}$$

In this case, I represents a subset of values of $n \in [1, N]$ that are preserved, all the other being removed by the projector P_I. For example, if $u(\vec{r}) = \sum_{n=1}^{N} u_n\, e_n(\vec{r})$, we have :

$$\big(P_I\, u\big)(\vec{r}) = \sum_{\substack{n \in [1,N] \\ \lambda_n \in I}} u_n\, e_n(\vec{r})$$

We now will demonstrate that the derivative of the spectral projector on an interval around a value $\omega^2 \in \mathbb{R}_+$ is linked to the cross-correlation function at the corresponding pulsation ω. We thus consider an interval $I = [\omega_-^2, \omega_+^2]$ around ω^2. The integral over $\lambda_k = c^2\, |\vec{k}|^2 \in I$ in Eq. 10.6 defines a volume of integration of dimension d that can be decomposed into two integrals, one over a volume of dimension $d-1$ defined by $c^2\, |\vec{k}|^2 = \omega^2$ and the other over $|\vec{k}|$:

$$[\![P_I]\!](\vec{r}_1, \vec{r}_2) = (2\,\pi)^{-d} \int_{c^2 |\vec{k}|^2 \in I} \int_{c^2 |\vec{k}|^2 = \omega^2} e(\vec{r}_1, \vec{k})\, \overline{e(\vec{r}_2, \vec{k})}\, |d^{d-1}\sigma|\, |\vec{k}|^{d-1}\, d|\vec{k}|$$

where $|d^{d-1}\sigma|$ is the usual measure of the unit $(d-1)$–dimensional sphere. In the case $d = 3$, $d^2\sigma$ is the infinitesimal solid angle. Taking the derivative with respect to ω_+ in this equation gives :

$$\frac{d}{d\omega_+} [\![P_I]\!](\vec{r}_1, \vec{r}_2) = \frac{(2\,\pi)^{-d}}{c} \left(\frac{\omega}{c}\right)^{d-1} \int_{c^2 |\vec{k}|^2 = \omega^2} e(\vec{r}_1, \vec{k})\, \overline{e(\vec{r}_2, \vec{k})}\, |d^{d-1}\sigma|$$

In this formula, one can recognize the cross-correlation of random scattered waves of frequency ω recorded at points $\vec{r}_1$ and $\vec{r}_2$ that can be written as :

$$\hat{C}(\omega, \vec{r}_1, r_2) = \frac{1}{\sigma_{d-1}} \int_{c^2 |\vec{k}|^2 = \omega^2} e(\vec{r}_1, \vec{k})\, \overline{e(\vec{r}_2, \vec{k})}\, |d\sigma|$$

where σ_{d-1} denote the total volume of the unit sphere in $\mathbb{R}^{d-1}$: $\sigma_0 = 2$, $\sigma_1 = 2\,\pi$, $\sigma_2 = 4\,\pi$, ...

Using the two previous equation, we find

$$\frac{d}{d\omega}[\![P_I]\!](\vec{r}_1,\vec{r}_2) = \frac{\sigma_{d-1}}{(2\,\pi)^d}\,\frac{1}{c}\,\left(\frac{\omega}{c}\right)^{d-1}\,C_\omega(\vec{r}_1,\vec{r}_2) \tag{10.7}$$

The projector P_I defined previously can also be written using the resolvent of the operator L using the Cauchy formula :

$$P_I = \frac{1}{2\,i\,\pi}\int_{\gamma_I}\big(L+\lambda\big)^{-1}\,d\lambda$$

where a γ_I is a contour in the complex plane which restriction to the real axis is I.

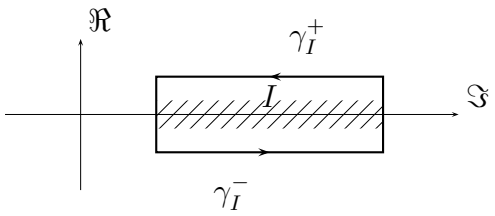

FIG. 10.1: γ_I can be split into two contours γ_I^+ and γ_I^- which are complex conjugate and followed in opposite direction.

This contour can be split into two contours defined by $\gamma_I^+ = \big\{\lambda\in\gamma_I\,|\,\Im(\lambda)\geq 0\big\}$ and $\gamma_I^- = \big\{\lambda\in\gamma_I\,|\,\Im(\lambda)< 0\big\}$ ($\Im$ denotes the imaginary part) as seen in Fig. 10.1. As γ_I^+ and γ_I^- are followed in opposite directions and as they are complex conjugates, we get :

$$\begin{aligned} P_I &= \frac{1}{2\,i\,\pi}\int_{\gamma_I^+}\Big[\big(L+\lambda\big)^{-1}-\big(L+\overline{\lambda}\big)^{-1}\Big]\,d\lambda \\ &= \frac{1}{\pi}\int_{\gamma_I^+}\Im\big(L+\lambda\big)^{-1}\,d\lambda \end{aligned}$$

and then, taking the integral kernel of this expression,

$$\begin{aligned} [\![P_I]\!] &= \frac{1}{\pi}\int_{\gamma_\varepsilon^+}\Im[\![\big(L+\lambda\big)^{-1}]\!]\,d\lambda \\ &= -\frac{1}{\pi}\int_{\omega_-}^{\omega_+}\Im[\![\big(L+(\omega+i0)^2\big)^{-1}]\!]\,2\,\omega\,d\omega \end{aligned}$$

which leads to the Stone formula, using the definition of $\hat{G}$

$$[\![P_I]\!](\vec{r}_1,\vec{r}_2) = -\frac{2}{\pi}\int_{\omega_-}^{\omega_+} \omega\, \Im\hat{G}(\omega,\vec{r}_1,\vec{r}_2)\, d\omega$$

This formula gives, by taking the derivative with respect to ω_+,

$$\frac{d}{d\omega_+}[\![P_I]\!](\vec{r}_1,\vec{r}_2) = -\frac{2\,\omega}{\pi}\,\Im\hat{G}(\omega,\vec{r}_1,\vec{r}_2) \tag{10.8}$$

The combination of Eq. 10.7 and Eq. 10.8 finally gives :

$$\hat{C}(\omega,\vec{r}_1,\vec{r}_2) = -\frac{2^{d+1}\,\pi^{d-1}}{\sigma_{d-1}}\,\frac{c^d}{\omega^{d-2}}\,\Im\hat{G}(\omega,\vec{r}_1,\vec{r}_2) \tag{10.9}$$

This gives a generalization of Eq. 10.5 in the case of observation in a region without local sources, and requires no hypothesis about attenuation. It shows that the equipartition at boundaries of the region of interest if sufficient to obtain the Green's function from cross-correlation, whatever is the wavefield inside the medium. This equation, established in the scalar case, can be extended to the elastic case using the same calculation. The cross-correlation function becomes a tensor, as well as the Green's function. Particular attention needs to be paid to velocities and dispersion relations as they depend on the type of waves.

10.3.4 The rate of convergence towards the Green's function

The question arises as to how much averaging is in principle necessary after which the Green's function is retrieved, and before which the cross-correlation remains dominated by noise. In the case that the field is due to uniformly distributed random sources, or in the case that the field is due to equipartitioned incident waves, it is possible to make theoretical estimates (*Larose et al.*, 2004a; *Snieder*, 2004; *Sabra et al.*, 2005d; *Weaver and Lobkis*, 2005a). All these authors have concluded, not surprisingly, that the convergence proceeds like the square root of the amount of data used in the cross-correlation. Signal-to-Noise Ratio (SNR), i.e., Green's function amplitude over residual fluctuations, is proportional to this square root. Quantitative estimates of the quality of the convergence are more challenging. *Weaver and Lobkis* (2005a) calculated the residual error in a scalar wave cross-correlation, and found it to be proportional to the energy in the diffuse field times the bandwidth times the fourth power of central frequency. A similar calculation for closed systems was confirmed in laboratory measurements (*Weaver and Lobkis*, 2005b). The residual error was compared to the amplitude of a ray arrival expected in the converged cross-correlation. Each ray arrival amplitude A depends on 1) the geometrical spreading of the Green's

function, and 2) the spatial extension of the noise sources that coherently contribute to the Green's function reconstruction. This zone is characterized by a directivity angle $\delta\theta = \sqrt{\frac{c}{r\,\omega}}$, where r is the source-receiver distance. The ray arrival was shown to be apparent in the cross-correlation if $\delta t\,\delta\omega \gg A^{d-1}$, where δt is the amount of data record employed (this is often months in seismic applications), $\delta\omega$ is the bandwidth of interest (often around 1 Hz or less in seismic applications), and $A = r\,\omega\,/\,c$, (the source-receiver distance r times the wavenumber $k = 2\,\pi\,/\,\lambda$). The power is equal to one less than the dimension d of the propagation; thus $d - 1 = 1$ for Rayleigh waves. Propagation between distant source-receiver pairs, and propagation in three dimensions, are especially challenging to resolve, largely due to the weakness of such ray arrivals.

10.4 Surface wave tomography of Europe

Practically, cross-correlation can be used at different scales to image structures from noise. Here, we present an example of seismic noise processing to produce high-resolution Rayleigh and Love waves group velocity maps for a region surrounding the European Alps. We focused on the [5-50 s] period band, where surface waves are mostly sensitive to the crust.

Stehly et al. (2006) have shown that the seismic noise sources in the [5-20 s] period band cover a large surface when integrated over a long time. This allows us to retrieve the Green's function between two stations by correlating background seismic noise records. The emerging signal of the Noise Correlation Function (NCF) is dominated by surface waves, since the background seismic noise mainly consists of surface waves. The reconstructed Green's functions are stable over time and robust enough to measure surface wave propagation times with a precision of a few tenths of a second, independently of the azimuth of the considered station pair path (*Stehly et al.*, 2007).

Passive imaging from seismic noise and Rayleigh wave group velocities has first been used by *Shapiro et al.* (2005) and *Sabra et al.* (2005c) who provided images of the Californian crust. More recently, noise based surface-wave tomography has been applied in Tibet (*Yao et al.*, 2006), New Zealand (*Lin et al.*, 2007), Korea (*Kang and Shin*, 2006), and to produce large-scale Rayleigh wave group velocity maps across Europe (*Yang et al.*, 2007).

We used one year of continuous records from October 2004 to October 2005 from 150 3-components broadband European stations. Our aim is to focus on the Alps, where we have a particularly high density of stations (Fig. 10.2). All the records are processed day per day. First the data are decimated to 1 Hz and corrected for the instrumental response. North and East horizontal components are rotated to get radial

and transverse components with respect to the inter-station azimuth. The records are then band-pass filtered and their spectrum whitened between 5 and 150 s. We correlated signals recorded on the components that correspond to the non-zero terms of the theoretical elastic Green's tensor (ZZ, ZR, RZ, RR, and TT, due to symmetry considerations). Subsequently, correlations of one-day records are stacked. This is approximately equivalent to cross-correlating directly the whole year of records. Rayleigh and Love waves dispersion curves are evaluated from the emerging Green's

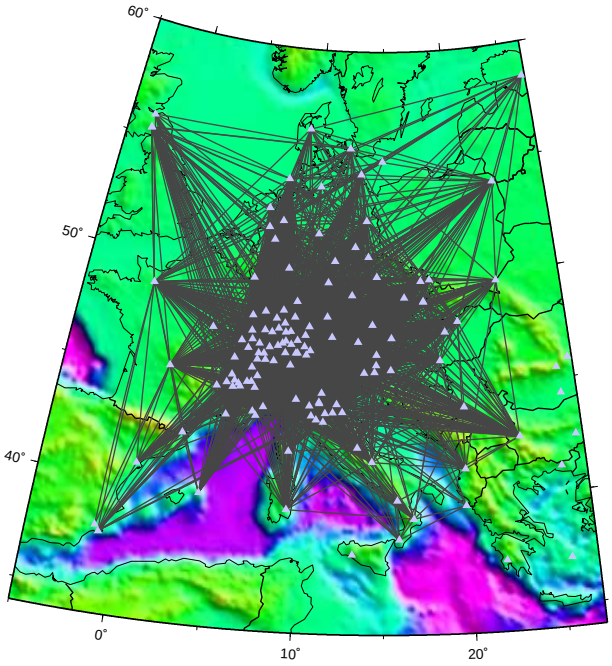

FIG. 10.2: The 3000 selected paths where 16 s Rayleigh wave group velocity measurements were obtained from cross-correlations of ambient seismic noise. White triangles show stations used for this study.

function using frequency-time analysis (*Levshin et al.*, 1989; *Ritzwoller and Levshin*, 1998) for the 17,000 inter-station paths. For each path we get eight evaluations of the Rayleigh-wave dispersion curves by considering four components of the correlation tensor (ZZ, RR, RZ and ZR) and both the positive and the negative part of the NCF. Similarly, we get two estimates of the Love-wave dispersion curves from positive and negative parts of TT correlations.

We reject waveforms 1) with SNR (ratio between Rayleigh wave's amplitude and noise variance after it) lower than seven; 2) with group velocities measured on the positive and negative correlation time differing by more than 5 percent; and 3) with paths shorter than two wavelengths at the selected period for the group velocity map. This results in about 3,500 paths over the initial 11,000 inter-stations paths at 16 s (Fig. 10.2). We then apply a tomographic inversion following *Barmin et al.* (2001) to this data set to obtain group velocity maps on $100 \times 100 = 10{,}000$ cells of

25×25 km across Europe (Fig. 10.3). Several geological features can be seen on those maps. Low velocity anomalies are associated with sedimentary basins, such as the Po basin (Northern Italy), the North Sea basin and the Pannonian basin (Slovakia and Hungary). Both Rayleigh and Love waves exhibit smaller values below the molassic sediments (Southern Germany and Austria) than in the surrounding area. Close to the French-Italian border, one can notice a high-velocity anomaly corresponding to the Ivrea body, an intracrustal high- velocity and high-density zone within the Adriatic plate. The final resolution is good enough to see the contrast in Rayleigh wave velocity between the sedimentary (North-West) and the mountainous (South) part of Switzerland. It is not possible to compare directly these group-velocity maps with

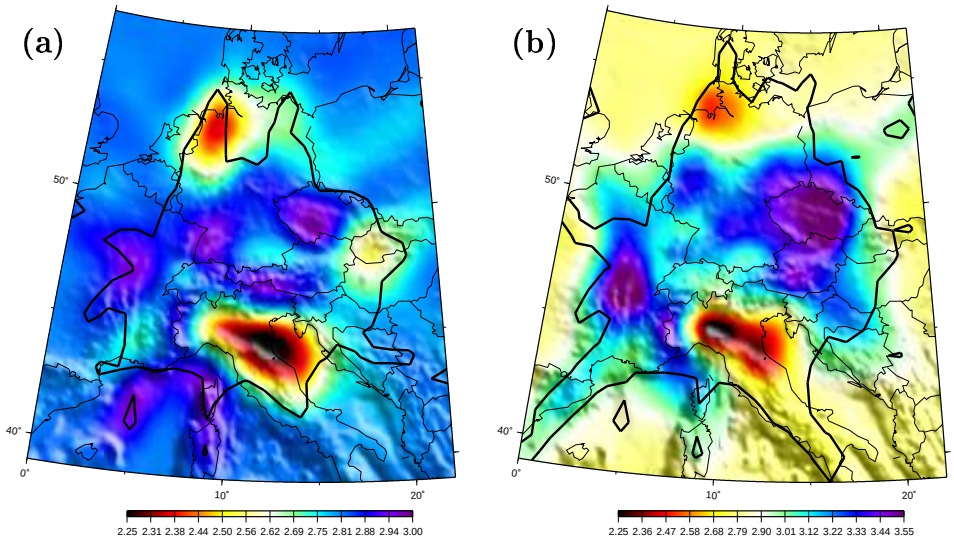

FIG. 10.3: Rayleigh (a) and Love (b) wave group velocity maps at 16 s period constructed from 3,500 and 4,400 inter-station cross-correlations, respectively. Black thick line delimits the area where there are more than 10 paths per 25×25 km cell.

maps obtained with active methods : practically, below 20 s of period, attenuation as well as scattering in the medium are too strong, preventing accurate measurement of surface-wave velocity from earthquakes or any active source. At these periods, the number of usable paths is thus two low to build any group-velocity map.

It is however possible to compare dispersion curves measured from passive and active methods in some other cases. *Shapiro and Campillo* (2004) measured dispersion curves using noise cross-correlation computed between pairs of stations separated by distances ranging from one hundreds to two thousand kilometers. At periods below 60 s, the resulting dispersion curves are in good agreement with those predicted by global group-velocity maps from *Ritzwoller et al.* (2002b). In Southern California, *Shapiro et al.* (2005) compared records of an earthquakes which occurred close to a station and recorded at two other stations, with noise cross-correlation signal computed on the same path. The measured arrival time were identical at period ranging

from 5 to 20 s. These results shows the robustness of measurements performed using noise cross-correlations.

The Alpine region has intensively been studied using controlled source and earthquake tomography. These studies gave precise insight about the crustal and upper mantle structure (*Marchant and Stampfli*, 1996; *Waldhauser et al.*, 1998, 2002; *Bleibinhaus and Gebrande*, 2005, and references therein). However, using seismic noise instead has several advantages. The final resolution depends mostly on the density of stations and is not limited by the available sources. This makes it possible to get high-resolution group velocity maps that cover large regions, whereas controlled sources can only be used for small areas. Surface wave tomography using earthquakes records only provides group velocity maps at periods above 20 s, since all the high- frequency information is lost due to attenuation in the medium.

10.5 3-D S-wave tomography of the Piton de la Fournaise volcano

The same seismic noise cross-correlation technique can be applied to study more complex structures. In this section we present the 3-D velocity model of a volcano obtained using only noise records.

18 months (Jul. 1999 to Dec. 2000) of continuous seismic noise recorded at 21 vertical short period stations were collected by the Observatoire Volcanologique du Piton de la Fournaise (Fig. 10.4a). An example of a noise record at one of the stations (ANR) is shown in Fig. 10.4b. All noise records are first band passed between 1 to 5 s and their spectral amplitudes whitened in order to avoid strong dominant spectral peaks in the background noise. For each available station pair, the one-bit Noise Correlation Function (NCF) is computed day per day. Some of the NCFs are rejected upon a SNR criterion (i.e., if the energy of the Rayleigh arrival is lower than 1.5 times the energy of the noise). The remaining traces are stacked over 18 months. For each path, group velocity dispersion curves are estimated using a Frequency-Time Analysis (FTAN, *Levshin et al.* (1989); *Ritzwoller and Levshin* (1998)). We manually select dispersion curves according to group velocity limits and for station-to-station distances longer than one wavelength. We finally obtain 75 reliable dispersion curves from which group velocities are extracted for periods equal to 2, 2.5, 3, 3.5, 4 and 4.5 s.

2-D Rayleigh wave group velocity maps are obtained from tomographic inversion of the arrival-time measurements at each period using the algorithm described by *Barmin et al.* (2001). Our 2-D models involve $22 \times 28 = 616$ 1×1 km cells. Because of the sparse ray coverage and the low resolution of the data set, we choose to apply a strong smoothing to the tomographic inversion which results in a $\sim$4-km spatial resolution.

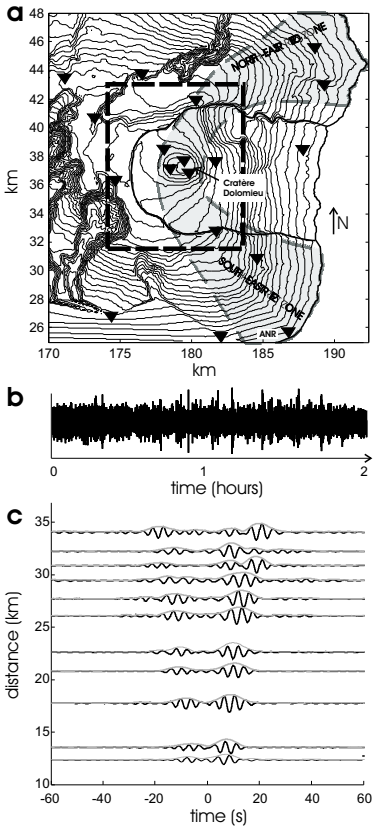

Fig. 10.4: a. Map of the Piton de la Fournaise volcano. Seismic stations are represented as inverted triangles. The gray zone indicates the limits of the rift zone. The thin dashed rectangle corresponds to the limits of the presented tomographic images. Geographic coordinates are Gauss-Laborde kilometric coordinates (Transverse Mercator). Contour lines are spaced every 100 m. **b**. Two hours of ambient seismic noise at station ANR. **c**. Causal and acausal reconstructed Rayleigh waves (positive and negative times, dominant period 4 s) between station RMR (not shown on the map) and the rest of the network. The trace envelopes are represented as thin gray curves.

The inversion results are thus robust and show a moderate variance reduction varying from 38 to 18 % with increasing periods (from 2 to 4.5 s).

Dispersion curves are then extracted from the Rayleigh-wave group-velocity maps for every model cell. We fit these curves by polynomial functions in a least-squares sense and invert them using a Monte-Carlo algorithm (*Shapiro et al.*, 1997), the synthetic dispersion curve being calculated using a method due to *Herrmann* (1987). We thus obtain a S-wave velocity-versus-depth profile for each cell. We present six horizontal slices as well as a 3-D view of the 3-D smoothed model in Fig. 10.5. The results clearly show the presence of a high-velocity anomaly which moves westward with depth (+1.3 to -1.1 km above sea level). This structure is surrounded by a low-velocity ring interpreted as effusive products associated with the construction of the Piton de la Fournaise volcano on the flank of the older Piton des Neiges volcano. This high-velocity anomaly has also been detected by a previous earthquake and active P-wave tomography on the Piton de la Fournaise volcano (*Lankar*, 1997). Recent works also imaged the presence of a high-velocity chimney on different volcanoes (*Laigle et al.*, 2000; *Tanaka et al.*, 2002; *Zollo et al.*, 2002; *Sherburn et al.*, 2006; *Patane et al.*, 2006). We interpret this anomaly as solidified intrusive magma bodies. The high-velocity anomaly is also well correlated with the rift zone at sea level (z = -0.5 km). Imaging these intrusive bodies is of particular interest because the magma paths are usually believed to follow their geometry (*Laigle et al.*, 2000; *Battaglia et al.*, 2005). Furthermore, other studies showed that a few months of seismic noise data will yield similar three-dimensional results to that obtained from 18 months' data (*Brenguier et al.*, 2007a). We also achieved a preliminary study on the temporal variations of the reconstructed Green's functions showing that we could detect relative velocity variations of less than 0.1 % with a temporal resolution of one day.

10.6 P-waves extraction from seismic noise cross-correlation

A main issue in the convergence of the correlation process to the transfer function is the influence of variations in the temporal and spatial distribution of the noise sources. From the temporal point of view, the noise spectrum defines the frequency bandwidth over which the impulse response can be retrieved. When receivers are widely separated, the coherent propagating noise must have sufficient amplitude to be recorded on both receivers despite geometrical spreading and attenuation. This explains why the slowly-attenuated Rayleigh waves have dominated the impulse response obtained so far from correlations of seismic noise.

In this section, we present results from the correlation function of seismic noise recordings among pairs of stations in the dense Parkfield network, California. When performed on many station pairs at short ranges, the noise correlation function (NCF) demonstrates the presence of both a P-wave and a Rayleigh wave in the NCF.

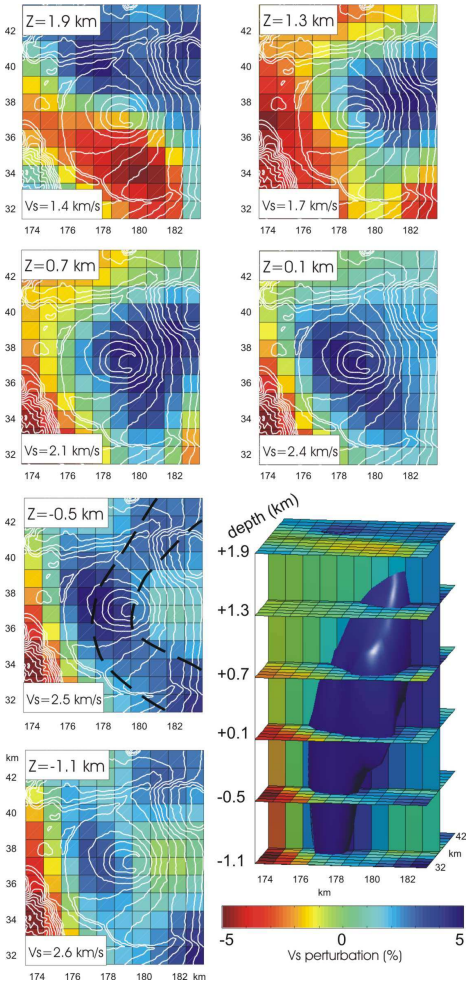

FIG. 10.5: 3-D S-wave velocity model. We show 6 horizontal slices extracted from the 3-D model at different depths. Average S-wave velocity is shown in white boxes on the bottom of corresponding slices. Black dashed line at depth -0.5 km shows the limits of the rift zone. We also plot a 3-D view of the model. The 3-D blue patch delimits the iso-velocity perturbation surface corresponding to a 2.5 % velocity perturbation.

We processed data recorded on the dense temporary seismic network installed in the Parkfield area between July 2001 and October 2002. One month of seismic noise recordings were cross-correlated between each pair of 30 broadband 3-component seismic stations located in an 11-km square (Fig. 10.6, *Thurber et al.* (2004)). We used only the vertical component. This network has xtensively been used to monitor and image the San Andreas Fault (SAF) using both man-made explosions and earthquakes as part of the San Andreas Fault Observatory at Depth (SAFOD) project. Inversion results have confirmed the spatial heterogeneity of P-wave velocity across the Fault up to 6 km in depth (*Ben-Zion and Malin*, 1991; *Catchings et al.*, 2002; *Hole et al.*, 2006). At first, frequency-incoherent beamforming is performed using the N = 30 stations of

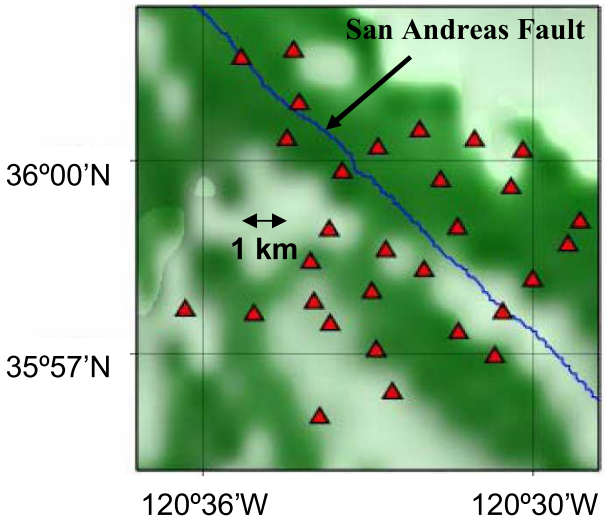

FIG. 10.6: Topographic map of the Parkfield area (an 11-km large square) showing stations (triangles) and SAF (blue).

the network to determine the average velocity c and direction θ of the seismic noise (Fig. 10.7). Beamforming is performed in two frequency bands of interest [0.2-0.5 Hz] and [0.6-1.3 Hz], on data segments of one day of seismic noise, recorded in February 2002, as :

$$B(\theta, c) = \frac{1}{\delta\omega} \int_{\omega_c - \delta\omega/2}^{\omega_c + \delta\omega/2} \sum_{i=1}^{N} \hat{S}_i(\omega) \exp\left(i \frac{\omega}{c} \left(x_i \sin\theta + y_i \cos\theta \right) \right) d\omega$$

where ω_c is the central noise frequency and $\delta\omega$ the frequency bandwidth, $\hat{S}_i(\omega)$ is the complex Fourier component at frequency ω of the noise signal $S_i(t)$ recorded on the ith seismic station ($i \in [1, N]$), and (x_i, y_i) are the longitude/latitude coordinates of station i. Working with a dense seismic network having a small coverage area allows determination of an average apparent incoming velocity for this zone using plane wave beamforming. In both of the frequency bands, the noise field clearly originates from

the Pacific Ocean with an incident direction $\theta_0 = 55°$ on the Parkfield network. On the other hand, the beamformer in the [0.2-0.5Hz] band exhibits an apparent velocity of 2.8 km/s compatible with a Rayleigh wave (Fig. 10.7a), while the beamformer in the [0.6-1.3Hz] band shows an apparent velocity of 5 km/s (Fig. 10.7b). Since Fig. 10.7

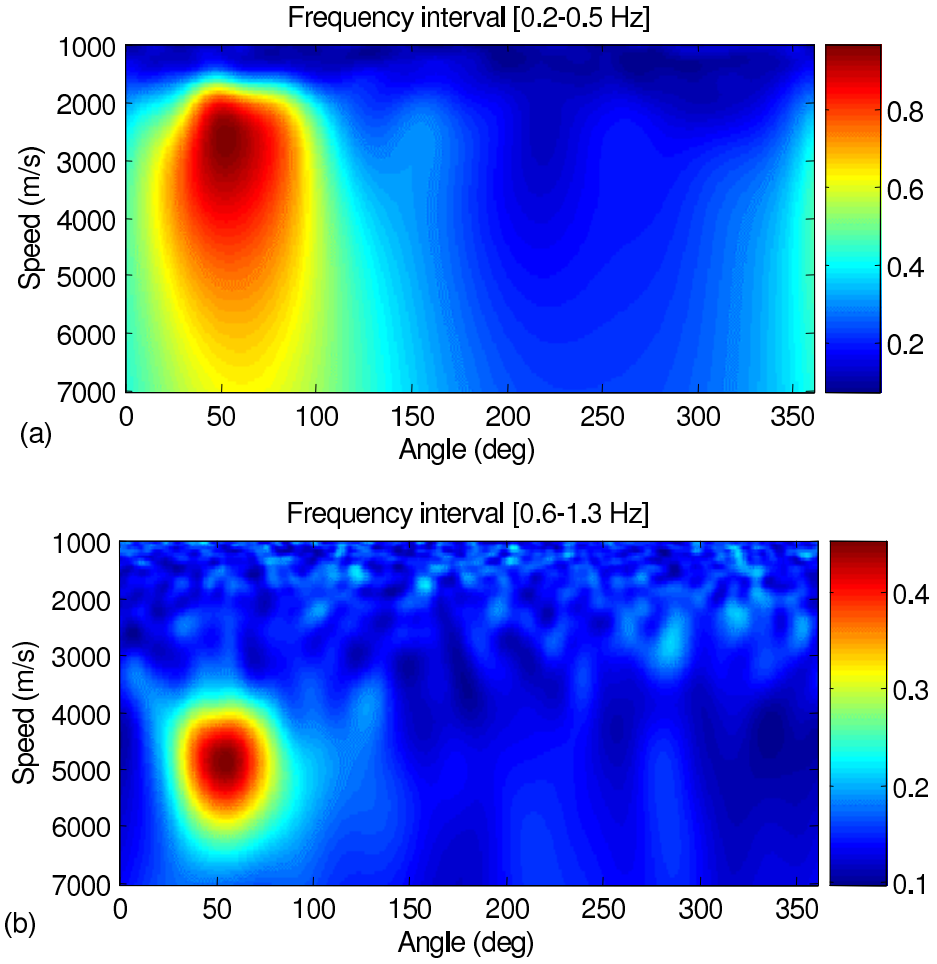

FIG. 10.7: Angular-speed distribution of pre-processed incoming noise on the Parkfield network averaged over one month. Plane wave beamforming is summed incoherently over 100 frequencies from (a) 0.2 to 0.5 Hz and (b) 0.6 to 1.3 Hz. The x-axis corresponds to noise directivity θ , north is 0°.

reveals a strong directivity in the seismic noise, only station pairs aligned with the noise main direction θ_0 are chosen to compute the point-to-point NCF. Restricting the cross-correlations to those pairs ensures that 1) the travel time of the main peak of the NCF is not biased and corresponds to the actual travel time of the Green's function between the stations (*Snieder*, 2004; *Roux et al.*, 2005b) and 2) the SNR of the NCF is maximized. Practically speaking, 145 station pairs are selected in the Parkfield network whose angles θ_{ij} are included in a directivity angle $\delta\theta = |\theta_{ij} - \theta_0| \leqslant \sqrt{\frac{c}{R_{ij}\,\omega_c}}$ dependent on the distance R_{ij} between stations and the frequencies characteristics of

the seismic noise field (*Roux and Kuperman*, 2004).

The NCF is computed for each selected station pair as in Eq. 10.3 of Section 10.3, and averaged over 30 days to further increase the SNR. Fig. 10.8a is a display of the NCFs obtained for the 145 selected pairs sorted by ascending offset R_{ij}. A propagating wavefront clearly appears at high frequency (Fig. 10.8b) which corresponds to a $\sim$ 5 km/s velocity wave. A polarization study between the Z-R and Z-Z components of the correlation tensor confirmed the P-wave nature of this wavefront (*Roux et al.*, 2005a). Going back to Fig. 10.7b, we note that the apparent velocity of the P-wave

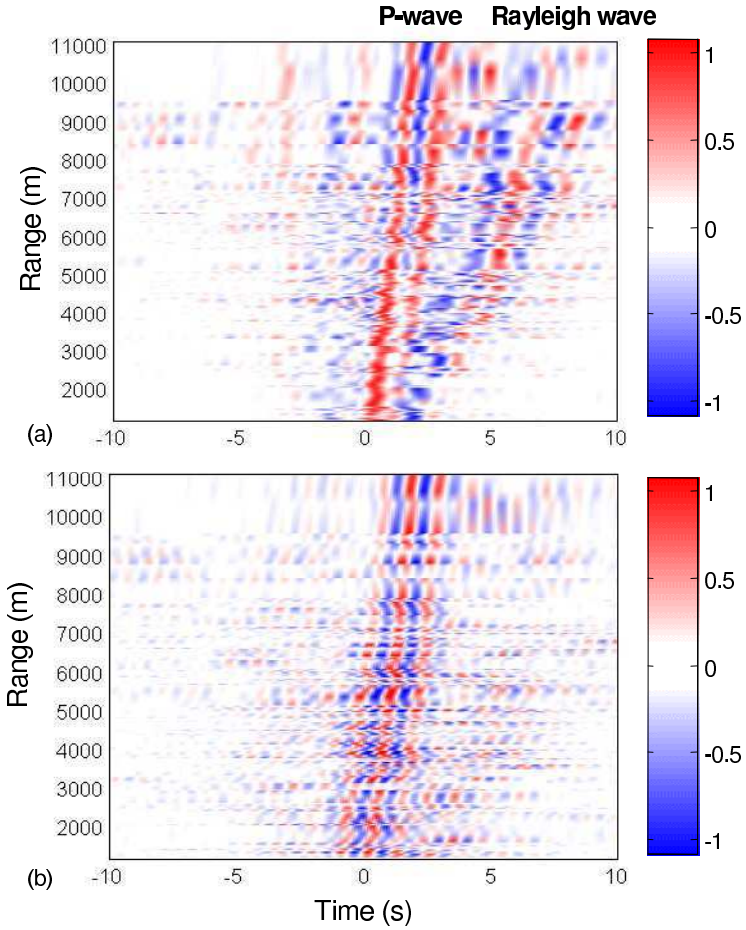

FIG. 10.8: Range-time representation of the Z-Z component of the noise correlation tensor averaged over one month in two frequency bands (a) [0.1-1.3 Hz], and (b) [0.6-1.3 Hz]. Each plot has been normalized by its own maximum.

corresponds to the P-velocity at the turning point. Recent inversions of the P-wave velocity profile reveal a strong velocity gradient at the surface, the 5 km/s speed being reached at no more than 1.5 km in depth on the west side of the SAF. This confirms that the noise sources that excite P-waves are local and can't be confused with deep incident waves that would hit the seismic array with a much higher apparent velocity.

One hypothesis is that P-waves are locally generated by conversion of incident Rayleigh waves coming from the Pacific by local heterogeneities at the Earth's surface or subsurface.

10.7 Small scale geophysics using surface waves extracted from noise cross-correlation.

In this section, we achieve an experimental demonstration of the correlation process of controlled noise sources at the meter scale using a linear array of accelerometers. It is known that the cross-correlation of seismic noise between two receivers converges towards the Green's function when noise is equidistributed in azimuth. The same result can be obtained with directional noise if noise sources are located in the end-fire lobes centered along the array line direction (*Roux and Kuperman*, 2004). When noise is not isotropic and noise sources are not adequately located with respect to the receivers array, 'controlled' noise sources can be used to produce appropriate wavefield satisfying the end-fire lobe criterion. This is particularly useful at small scales and high frequencies where local sources strongly contribute to the noise wavefield.

A 14-meter long line of 8 evenly-spaced vertical accelerometers has been used to record human steps. We walked in the alignment of the accelerometers line, 5 times one minutes on each side, from 0 to about 30 meters away from the accelerometer array. The experimental setup was designed to be versatile : 1) the array configuration may include up to 16 one-component seismic stations; 2) these seismic sensors could be accelerometers or geophones depending on the expected frequency bandwidth; 3) the array length is adjustable to the surface wave wavelength.

The main advantage of this system is to be easy and fast to setup. Our ambition was to achieve a complete deployment, acquisition and processing in approximately 30 minutes. The system design makes it very convenient for local and near surface measurements.

The energy spectrum of the recorded steps spreads up to 150 Hz. Given the frequency response of the accelerometers and the spatial extension of the array, a frequency interval ranging from 10 to 100 Hz was selected for the analysis. Since the frequency spectrum of the steps is not flat in this frequency interval, and as correlating is mathematically equivalent to a spectrum product, only the most energizing frequencies will emerge in the correlation signal. To enlarge the effective frequency bandwidth, the spectrum of the records is equalized in the selected frequency interval [10-100 Hz] before the correlation process.

To check the robustness of the correlation process, 5 one-minute long records were separately correlated for each accelerometer pair. The five time-domain correlations

superimpose in phase, leading to the conclusion that correlation is robust and does not depend on the way we walked. As these correlation signals superimpose, they are stacked to increase the SNR. The advantage of the correlation process is then to perform an ensemble average over the 'controlled' noise sources without the need of synchronization. The superposition of the correlations of one minute long signals is thus just a verification of the repeatability of the steps. Stacking five correlations of one minute long record is equivalent to correlating directly a 5-minute long signal.

To obtain a seismic section from the correlation process, signals are cross-correlated by the accelerometers located at the extremity of the line array. Taking one or the other of the accelerometers as the reference signal does not modify the seismic section. This shows that seismic propagation from left to right is identical to propagation from right to left on the 14-m long seismic array. The medium can then be assumed 1-D in the frequency bandwidth of the recordings. The 1-D argument can be pushed even further. Two receiver pairs separated by the same range are stacked since propagation does not depend on the pair location but only on the offset between receivers.

Fig. 10.9 shows the seismic section obtained after the complete spatial and temporal stacking. After a 10-minutes total recording, SNR is above 30 dB. Both phase dispersion and attenuation during propagation is retrieved. The final seismic section clearly reveals the presence of two surface waves, with mean group velocities of about 90 and 120 m/s. Those low group velocities are good indications of two Rayleigh modes. We

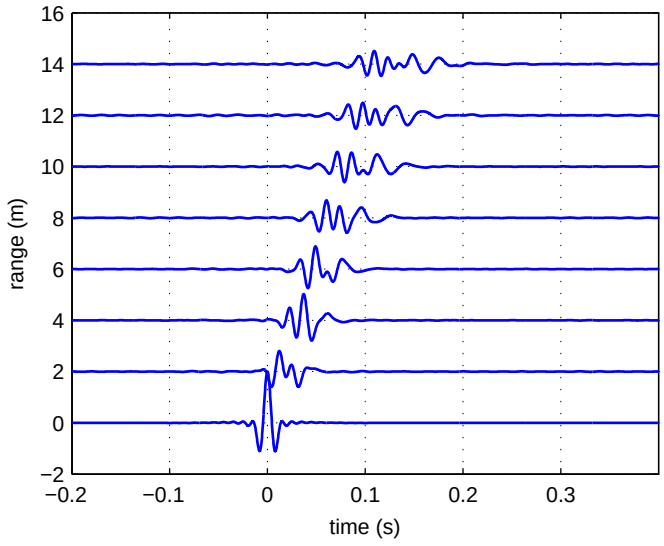

Fig. 10.9: Seismic section obtained from the correlation process after all averaging operations. The signal-to-noise ratio is above 30 dB for each trace. Both phase dispersion and attenuation are observed. The seismic propagation reveals the presence of two surface waves with group velocity of about 90 and 120 m/s.

wish to insist on the fact that this section was obtained from 10 minutes of unsyn-

chronized human steps only, which makes it nearly a passive method. To get the same result with usual active seismic techniques, much more time would have been needed to synchronize numerous sledgehammer blows. The 'passive' method presented here is thus 1) Easy to implement, as there is a large flexibility in the array configuration, 2) Fast, as it takes only about 30 minutes to complete the array deployment and the recording, and 3) Simple, as there is no synchronization task and processing is performed in real time.

A frequency-wavenumber (F-K) transform was applied to the seismic section in Fig. 10.9 to identify each of the surface waves (Fig. 10.10). As the accelerometers are evenly spaced by a distance d = 2 m, the largest wavenumber before aliasing is $2\pi/\mathrm{d} = \pi$. In Fig. 10.10, this value of k correspond to the green line. Higher k's are wrapped, and appear as low wavenumbers. In this simple case, the wavenumber spectrum can be extended by unwrapping the k axis. From the F-K diagram in Fig. 10.10, modes

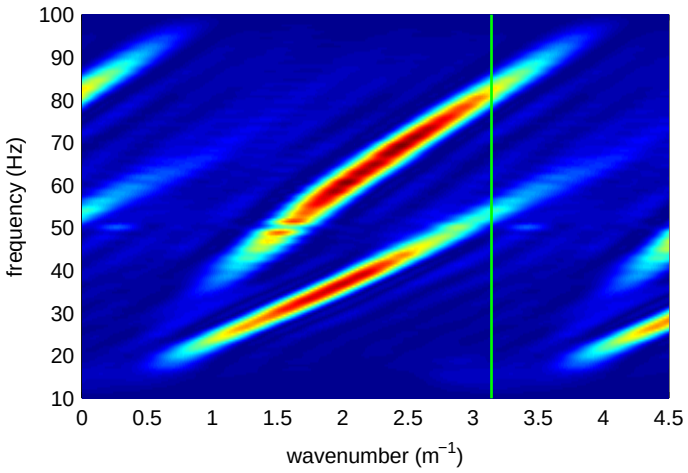

Fig. 10.10: Frequency wavenumber (F-K) transform of the seismic section obtained in Fig. 10.9. The largest measurable wavenumber according to the Shannon criterion is $2\pi/\mathrm{d}$ with d = 2 m (green line). The aliasing in the F-K diagram is resolved by unwrapping the k axis. The shape of the two modes on the F-K diagram reveals dispersive modes.

are separated and their phase velocity dispersion curves are extracted. Those surface-wave dispersion curves are the starting point for a surface wave inversion to retrieve the local velocity versus depth profile of the medium.

10.8 Passive correlation imaging of a buried scatterer

Since now, most of geophysical application of passive imaging with ambient-noise cross-correlation have been used to reconstruct direct arrivals of Rayleigh or P-waves.

Reconstructing other features of the Green's function, like the reflections following direct waves, is harder : the reflections are weaker and the propagation is fully 3-D. Nevertheless, passively imaging a scatterer would form a major application to prospecting and certainly deserves attention. In order to test the feasibility of passively imaging a buried scatterer, we set a controlled ultrasonic experiment in the laboratory. We believe the principles presented here also apply to ambient seismic noise.

To mimic micro-seismic vibrations, we use a highly reverberant body excited by a series of sources (see Fig. 10.11). A 12 mm diameter cylindrical hole was drilled through an aluminium block of dimensions 125 mm×125 mm×90 mm. The hole is 25 mm beneath the surface. To excite elastic waves, we employ a laser mounted on a step motor. For a complete description of the experimental set-up, please refer to *Larose et al.* (2006a). The laser emits mainly shear waves (*Mason and Thurston*, 1988) (see directivity in Fig. 10.11). The resulting wave field is recorded by two pin transducers located at $\vec{r}_1$ and $\vec{r}_2$. The laser triggers the waveform acquisition. For each position of the source $\vec{r}_s^{\,i}$ and receiver k, the record is noted $S_{ik}(t) = G(t, \vec{r}_k, \vec{r}_s^{\,i}) \otimes R_k(t)$ where G is the elastic Green's function, $\otimes$ is convolution and $R_k(t)$ is the transfer function of the receiver k. Each record is filtered in the [0.05-0.9 MHz] frequency band, where the absorption time of the block is about 30 ms. Diffuse field decay is therefore slow enough to permit record lengths greater than 100 ms, which represent thousands of reverberations within the cavity. After each acquisition, the laser is moved to another position. 1 mm steps are used to mimic a linear array of 60 points. By reciprocity, the sources and receivers can be interchanged. Our experimental set-up is therefore analogous to a conventional seismic experiment where a linear array of 60 geophones would sense the seismic diffuse wavefield generated by two distant sources. The Green's function between any couple of points $(\vec{r}_s^{\,i}, \vec{r}_s^{\,j})$ of the array is recovered by processing the following time-correlation :

$$\begin{aligned} C_{ij}^k(\tau) &= \int S_{ik}(t)\, S_{jk}(t+\tau)\, dt \\ &= G(t, \vec{r}_k, \vec{r}_s^{\,i}) \times G(t, \vec{r}_k, \vec{r}_s^{\,j}) \otimes R_k(t) \otimes R_k(-t) \end{aligned}$$

To remove the receiver functions R_k, we deconvolve the cross-correlations by the averaged auto-correlations $\left\langle C_{ii}^k(\tau) \right\rangle_i \approx R_k(t) \otimes R_k(-t)$. This procedure has the additional virtue of removing contaminations $G(t, \vec{r}_k, \vec{r}_k)$ or *ghosts*, which *Derode et al.* (2003b); *Weaver and Lobkis* (2006) related to the environment of the receivers R. Then these correlations are averaged over the available distant sources $\vec{r}_{k=1,2}$ to get $C_{ij}(\tau)$. As noted by several authors (*Lobkis and Weaver*, 2001b; *Weaver and Lobkis*, 2001; *Derode et al.*, 2003b; *van Tiggelen*, 2003; *Snieder*, 2004; *Sabra et al.*, 2005e; *Weaver*, 2005; *Weaver and Lobkis*, 2006), this correlation is essentially the Green's function $G(\tau, \vec{r}_s^{\,i}, \vec{r}_s^{\,j})$ and therefore should contain the deterministic signature of the isolated scatterer.

In Fig. 10.12 we display the time-distance wavefield obtained for all the available

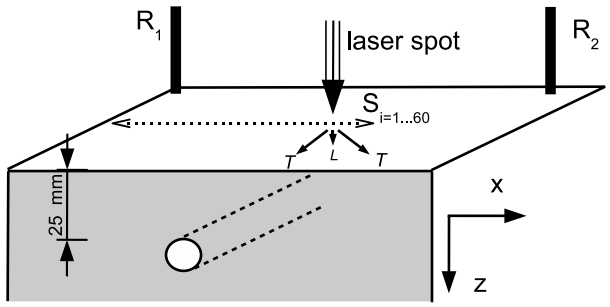

FIG. 10.11: Set-up of the ultrasonic experiment. The source scans the surface with 1 mm steps along a line of 60 mm. The directivity (*Mason and Thurston*, 1988) of one laser shot is shown for shear (transverse T) waves, and weaker compressional (longitudinal L) waves.

autocorrelations $C_{ii}(\tau)$. This auto-correlation is the field sensed in i if i were both source and receiver. Position 0 marks the center of the array. The hyperbolic feature is the signature of the buried scatterer : the wave labeled (a) is the wave reflected by the top of the cylindrical hole placed at z = 25 mm and x = 4 mm. The arrival times along the array correspond to a shear (transverse) wave (v_T = 3.1 mm/μs). (c) is a compressional-to-Rayleigh reflected by the lateral edge of the cavity, and (d) is a Rayleigh-to-Rayleigh reflected by the same edge. The shear wave directivity of the laser generation is clearly visible in the null at (b). Because longitudinal wave generation is much weaker than that of shear waves (*Mason and Thurston*, 1988), its reflection (e) is hardly visible. Noteworthily, the passive reconstruction of any

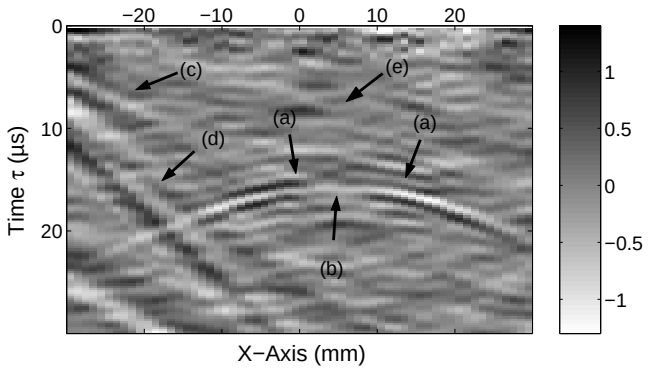

FIG. 10.12: Time-distance wavefield (linear scale, arbitrary unit). Each autocorrelation $C_{ii}(\tau)$ is plotted for different position i along the X-axis, and time τ. Position 0 marks the center of the array ; (a-e) are different reflections (see the text).

$G(\tau, \vec{r}_s^{\,i}, \vec{r}_s^{\,i})$ remains imperfect. The averaging used to construct the correlation is finite, leaving visible fluctuations in Fig. 10.12. To improve the quality of this image, one could increase the record length, or employ additional receivers $\vec{r}_k$ (*Weaver and Lobkis*, 2005b). Alternatively, we could perform beamforming in order to take advantage of all the $C_{i\neq j}$ cross-correlations. Beamforming is a standard procedure to

obtain medical or seismic (migrated) image. The new point is that here the impulse responses $C_{i\neq j}$ are obtained *passively*.

The image we now process is a 2-D image of the reflectivity of the medium. The first step is to apply beamforming to the forward propagation to focus the wave on any point (x,y) in the medium. This is achieved by summing the time-delayed impulse responses $C_{ij}(\tau)$. The same beamforming technique is then applied to the wave back-propagation (from the focal point to the receivers), the reflectivity ϕ of the medium is then :

$$\phi(x,y) = \left[\sum_{ij} C_{ij}\left(\tau_i + \tau_j\right)\right]^2$$

where $\tau_i = \frac{1}{v_T}\sqrt{(x-x_i)^2 + z^2}$ and v_T is the shear wave velocity. The 2-D reflectivity map of the medium is displayed in Fig. 10.13. The top of the reflector is clearly visible. Because of the finite size of the linear array, the sides and bottom of the cylindrical hole cannot be imaged. The shear wave directivity of the laser spot induces a preferential reflection for oblique incidences ; additionally, the images in Fig. 10.12 and 10.13 show a null at apex. Speckle fluctuations are noticeable making these figures a little more noisy than the ones obtained with Rayleigh waves. This is expected since the field at the free surface is dominated by Rayleigh waves. To conclude this part, we have here

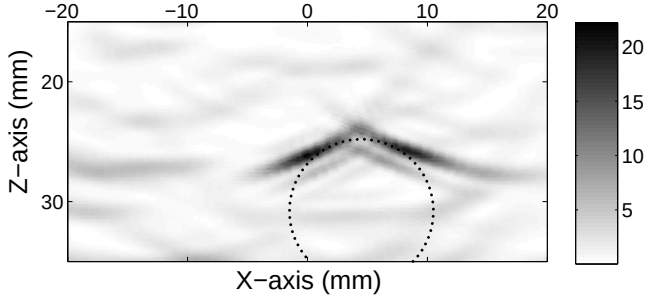

FIG. 10.13: Reflectivity (linear scale, arbitrary unit) of the aluminium block as probed by bulk shear waves. The array of 60 laser sources is at z = 0. Black indicates a high reflectivity. The top of the hole is clearly visible. The actual position of the cylinder is displayed in the dotted line.

shown the feasibility of imaging small details of the medium (like a buried isolated scatterer) by means of the passive time-correlation technique. By reciprocity this experimental set-up is analogous to an array of seismic geophones sensing the diffuse wavefield originating from distant sources. We therefore believe this technique could be transposed and applied to geophysical prospecting, as well as to medical imaging. The use of fully developed diffuse field in a closed cavity is not a rigorous requirement for this imaging technique. It could in principle be replaced by any other diffuse field, like diffuse waves in an open medium, or ambient noise.

10.9 Conclusion

In this paper, we theoretically reviewed how and under which assumptions cross-correlation of noise recorded at two sensors yields the Green's function between them. This property is based on equipartition of the wavefield that can be provided either by an appropriate sources distribution or by wave scattering in the medium. Any diffuse field, like diffuse waves in an open medium, or ambient noise may be used to reconstruct the Green's function between two points.

We experimentally showed the feasibility of passive imaging using noise cross-correlation. This technique bypasses the usual shortcomings encountered in active imaging, especially concerning the requirements about sources (strength, location, occurrence, etc). Application to ambient seismic noise is particularly promising for improving images of the Earth as the number of usable ray paths for tomography is directly linked to the number of recording stations. In more complex structures like volcanoes, this technique was validated as the S-wave velocity model obtained presents the same anomalies as in active measurements. Nevertheless, in a context where standard active methods are hampered by irregular sources distribution, the possibility of using noise records is particularly interesting. Those results demonstrate the possibility to achieve surface-wave tomography from noise cross-correlation. Results from the Parkfield area show that P-waves are present in the correlation on small-scale seismic networks, and could be used for body wave tomography.

At smaller scales, cross-correlation imaging techniques brings a new way to achieve seismic experiments that is faster and easier to implement than usual active methods. The recorded wavefield can be produced by active sources adequately located or using scattering to produce a diffuse wavefield. We showed that late arrivals, like reflections produced by buried objects, can be retrieved. This passive imaging of scatterers would be a major application of noise cross-correlation in geophysical prospecting. This technique is also promising for geophysical surveys, as seismic noise is a reproducible, stationary in time, natural source, that could also be used to give new insights into 4-D seismic exploration.

10.10 Detailed calculation of the cross-correlation function (Eq. 10.4)

We start from the definition of the cross-correlation function between two points A and B (Eq. 10.3) in which we express the wavefield u using the Green's function G :

$$\begin{aligned} C(\tau,\vec{r}_A,\vec{r}_B) &= \lim_{T\to+\infty}\frac{1}{T}\int_0^T u(t,\vec{r}_A)\,\overline{u(t+\tau,\vec{r}_B)}\,dt \\ &= \lim_{T\to+\infty}\frac{1}{T}\int_0^T dt\int_0^\infty ds\int_X d\vec{r}_s\,G_a(s,\vec{r}_A,\vec{r}_s)\,f(t-s,\vec{r}_s) \\ &\quad\times\int_0^\infty ds'\int_X d\vec{r}_s{}'\,\overline{G_a(s',\vec{r}_B,\vec{r}_s{}')\,f(t+\tau-s',\vec{r}_s{}')} \end{aligned}$$

The large T limit can be replaced by an ensemble average, that gives the mathematical expectation denoted $\mathbb{E}$. As f is a white noise, we have :

$$\mathbb{E}\big[f(t-s,\vec{r}_s)\,f(t+\tau-s',\vec{r}_s{}')\big] = \sigma^2\,\delta(\tau+s-s')\,\delta(\vec{r}_s-\vec{r}_s{}')$$

$$\begin{aligned} \lim_{T\to+\infty}\frac{1}{T}\int_0^T f(t-s,\vec{r}_s)\,f(t+\tau-s',\vec{r}_s{}')\,dt &= \mathbb{E}\big[f(t-s,\vec{r}_s)\,f(t+\tau-s',\vec{r}_s{}')\big] \\ &= \sigma^2\,\delta(\tau+s-s')\,\delta(\vec{r}_s-\vec{r}_s{}') \end{aligned}$$

where σ is the variance of the white noise. This property simplifies the previous equation, and we get :

$$C(\tau,\vec{r}_A,\vec{r}_B) = \sigma^2\int_0^\infty ds\int_X d\vec{r}_s\,G_a(s,\vec{r}_A,\vec{r}_s)\,\overline{G_a(s+\tau,\vec{r}_B,\vec{r}_s)}$$

Using the expression of the Green's function (Eq. 10.2) :

$$\begin{aligned} C(\tau,\vec{r}_A,\vec{r}_B) &= \sigma^2\int_0^\infty ds\int_X d\vec{r}_s\,Y(s)\,Y(s+\tau)\,e^{-a\,s}\,e^{-a\,(s+\tau)} \\ &\quad\left[\!\!\left[\frac{\sin s\sqrt{-L-a^2}}{\sqrt{-L-a^2}}\right]\!\!\right](\vec{r}_A,\vec{r}_s)\,\overline{\left[\!\!\left[\frac{\sin(s+\tau)\sqrt{-L-a^2}}{\sqrt{-L-a^2}}\right]\!\!\right](\vec{r}_B,\vec{r}_s)} \end{aligned}$$

We use two properties of the integral kernel :

$$\begin{aligned} \overline{[\![P]\!](x,y)} &= [\![\overline{P}]\!](x,y) = [\![P]\!](y,x) \\ \int_X [\![P_1]\!](x,z)\;[\![P_2]\!](z,y)\,dz &= [\![P_1\cdot P_2]\!](x,y) \end{aligned}$$

to get a new formula for the cross-correlation function :

$$C(\tau,\vec{r}_A,\vec{r}_B) \;=\; \sigma^2 \int_0^\infty ds\, Y(s+\tau)\; e^{-a\,(2\,s+\tau)} \left[\!\!\left[\frac{\sin s\sqrt{-L-a^2}}{\sqrt{-L-a^2}}\; \frac{\sin\,(s+\tau)\sqrt{-L-a^2}}{\sqrt{-L-a^2}} \right]\!\!\right](\vec{r}_A,\vec{r}_B)$$

Using $\sin\alpha\;\sin\beta = 1/2\,\big(\cos(\alpha-\beta)-\cos(\alpha+\beta)\big)$ and computing the integral over ds, we get Eq. 10.4 :

$$C(\tau,\vec{r}_A,\vec{r}_B) = \frac{\sigma^2\, e^{-a\,|\tau|}}{4\,a} \left[\!\!\left[(-L)^{-1}\; \left(\cos\tau\sqrt{-L-a^2} + a\,\frac{\sin|\tau|\sqrt{-L-a^2}}{\sqrt{-L-a^2}} \right) \right]\!\!\right](\vec{r}_A,\vec{r}_B)$$

Bibliographie

Abubakirov, I., and A. Gusev (1990), Estimation of scattering properties of lithosphere of kamchatka based on monte-carlo simulations of record envelope of a near earthquake, *Phys. Earth Planet. Inter.*, *64*, 52–67.

Aki, K. (1957), Space and time spectra of stationary stochastic waves with special reference to microtremors, *Bulletin of the Earthquake Research Institute*, *35*, 415–456.

Aki, K., and B. Chouet (1975), Origin of coda waves : Source, attenuation, and scattering effects, *Journal of Geophysical Research*, *80*, 3322–3342.

Aki, K., and P. G. Richards (1980), *Quantitative seismology : theory and practice*, 487-498 pp., W. H. Freeman & Co.

Barmin, M. P., M. H. Ritzwoller, and A. L. Levshin (2001), A fast and reliable method for surface wave tomography, *Pure and Applied Geophysics*, *158*, 1351–1375.

Battaglia, J., V. Ferrazzini, T. Staudacher, K. Aki, and J.-L. Cheminée (2005), Pre-eruptive migration of earthquakes at the Piton de la Fournaise volcano (Réunion Island), *Geophysical Journal International*, *161*, 449âĂŞ 458.

Ben-Zion, Y., and P. Malin (1991), San Andreas fault zone head waves near Parkfield, California, *Science*, *251*, 1592–1594.

Beucler, E., and J.-P. Montagner (2006), Computation of Large Anisotropic Seismic Heterogeneities (CLASH), *Geophysical Journal International*, *165*(2), 447–468, doi :10.1111/j.1365-246X.2005.02813.x.

Bleibinhaus, F., and H. Gebrande (2005), Crustal structure of the Eastern Alps along the TRANSALP profile from wide-angle seismic tomography, *Tectonophysics*, *414*, 51–69.

Brenguier, F., N. M. Shapiro, M. Campillo, Z. Ferrazzini, Z. Duputel, O. Coutant, and A. Nercessian (2007a), Toward forecasting volcanic eruptions using seismic noise, submitted.

Brenguier, F., N. M. Shapiro, M. Campillo, A. Nercessian, and V. Ferrazzini (2007b), 3-D surface wave tomography of the Piton de la Fournaise volcano using seismic noise correlation, *Geophysical Research Letters*, *34*, L02,305, doi : 10.1029/2006GL028586.

Campillo, M. (2006), Phase and correlation in 'random' seismic fields and the reconstruction of the Green function, *Pure and Applied Geophysics*, *163*, 475–502, doi :10.1007/s00024-005-0032-8.

Campillo, M., and A. Paul (2003), Long-range correlations in the diffuse seismic coda, *Science*, *299*, 547–549.

Catchings, R. D., M. J. Rymer, M. R. Goldman, J. A. Hole, R. Huggins, and C. Lippus (2002), High-resolution seismic velocities and shallow structure of the San Andreas fault zone at Middle Mountain, Parkfield, California, *Bulletin of the Seismological Society of America*, *92*, 2493–2503, doi :10.1785/0120010263.

Claerbout, J. F. (1968), Synthesis of a layered medium from its acoustics transmission response, *Geophysics*, *33*, 264–269.

Colin de Verdière, Y. (2006a), Mathematical models for passive imaging I : general background.

Colin de Verdière, Y. (2006b), Mathematical models for passive imaging II : effective hamiltonians associated to surface waves.

Derode, A., A. Tourin, and M. Fink (1999), Ultrasonic pulse compression with one-bit time reversal through multiple scattering, *Journal of Applied Physics*, *89*(9), 6343–6352.

Derode, A., E. Larose, M. Campillo, and M. Fink (2003a), How to estimate the Green's function of a heterogeneous medium between two passive sensors ? Application to acoustic waves, *Applied Physics Letters*, *83*(15), 3054–3056.

Derode, A., E. Larose, M. Tanter, J. de Rosny, A. Tourin, M. Campillo, and M. Fink (2003b), Recovering the Green's function from field-field correlations in an open scattering medium (L), *The Journal of the Acoustical Society of America*, *113*, 2973–2976.

Dèzes, P., and P. Ziegler (2001), European map of the mohorovicic discontinuity., *2nd EUCOR-URGENT Workshop (Upper Rhine Graben Evolution and Neotectonics)*.

Dolenc, D., B. Romanowicz, D. Stakes, P. McGill, and D. Neuhauser (2005), Observation of infragravity waves at the Monterey ocean bottom broadband station (MOBB), en preparation.

Duvall, T. L., S. M. Jefferies, J. W. Harvey, and M. A. Pomerantz (1993), Time distance helioseismology, *Nature*, *362*, 430–432.

Dziewonski, A. M., and D. L. Anderson (1981), Preliminary Reference Earth Model, *Phys. Earth Planet. Inter.*, *25*, 297–356.

Einstein, A. (1905), *A. Ann. Phys.*, *17*.

Ekström, G. (2001), Time domain analysis of Earth's long-period background seismic radiation, *Journal of Geophysical Research*, *106*, 26,483–26,494, doi : 10.1029/2000JB000086.

Ekström, G., J. Tromp, and E. Larson (1997), Measurements and global models of surface wave propagation, *Journal of Geophysical Research*, *102*(8137-8157).

Friedrich, A., F. Krüger, and K. Klinge (1998), Ocean generated microseismic noise located with the Gräfenberg array, *J. of Seismology*, *2*, 47–64.

Gilles, P. M., T. L. Duvall, P. H. Scherrer, and R. S. bogart (1997), Subsurface flow of material from the Sun equator's to its poles, *Nature*, *390*, 63–64.

Godin, O. A. (2007), Emergence of the acoustic Green's function from thermal noise, *The Journal of the Acoustical Society of America*, *121*, EL96–EL102, doi : 10.1121/1.2430764.

Gouédard, P., P. Roux, and M. Campillo (2006), Small scale geophysics inversion using surface waves extracted from noise cross-correlation, in *3rd Internationnal Symposium on the Effects of Surface Geology on Seismic Motion.*

Gouédard, P., et al. (2007), Cross-correlation of random fields : Mathematical approach and applications, *Geophys. Prosp.*, *submitted.*

Gutenberg, B. (1951), Observation and theory of microseisms, *American Meteorological Society*, pp. 1303–1311.

Hennino, R., N. Tégourès, N. Shapiro, L. Margerin, M. Campilo, B. van Tiggelen, and R. Weaver (2001), Observation of equipartition of seismic waves, *Physical Review Letter*, *85*(15), 3447–3450.

Herrmann, R. B. (1987), Computer programs in seismology.

Hole, J., T. Ryberg, G. Fuis, F. Bleibinhaus, and A. Sharma (2006), Structure of the San Andreas fault zone at SAFOD from a seismic refraction survey, *Geophysical Research Letters*, *33*, L07,312.

Hoshiba, M. (1991), Simulation of multiple-scattering coda wave excitation based on the energy conservation law, *Phys. Earth Planet. Inter.*, *67*, 123–136.

Jones, C., H. Kanamori, and S. Roecker (1994), *Journal of Geophysical Research*, *99*, 4567–4601.

Kang, T.-S., and J. S. Shin (2006), Surface-wave tomography from ambient seismic noise of accelerograph networks in southern Korea, *Geophysical Research Letters*, *33*, L17,303, doi :10.1029/2006GL027044.

Kobayashi, N., and K. Nishida (1998), Continuous excitation of planetary free oscillations by atmospheric disturbances, *Nature*, *395*, 357–360.

Kos, S., and P. Littlewood (2004), *Nature*, *431*(29).

Kubo, R. (1966), The fluctuation-dissipation theorem, *Reports on Progress in Physics*, *29*, 255–284.

Laigle, M., A. Hirn, M. Sapin, J. Lépine, J. Diaz, J. Gallart, and R. Nicolich (2000), Mount Etna dense array local earthquake P and S tomography and implications for volcanic plumbing, *Journal of Geophysical Research*, *105*, 21.633–21.646.

Lankar, V. (1997), Approches par tomographie sismique du Piton de la Fournaise, La Réunion, Ph.D. thesis, Institut de Physique du Globe de Paris, France.

Larmat, C., J.-P. Montagner, M. Fink, Y. Capdeville, A. Tourin, and E. Clévédé (2006), Time-reversal imaging of seismic sources and application to the great sumatra earthquake, *Geophysical Research Letters*, *33*, doi :doi :10.1029/2006GL026336.

Larose, E., A. Derode, M. Campillo, and M. Fink (2004a), Imaging from one-bit correlation of wide-band diffuse wavefield, *Journal of Applied Physics*, *95*, 8393–8399, doi :10.1063/1.1739529.

Larose, E., A. Derode, M. Campillo, and M. Fink (2004b), Imaging from one-bit correlation of wide-band diffuse wavefield, *Journal of Applied Physics*, *95*, 8393–8399, doi :10.1063/1.1739529.

Larose, E., A. Khan, Y. Nakamura, and M. Campillo (2005), Lunar subsurface investigated from correlation of seismic noise, *Geophysical Research Letters*, *32*, L16,201, doi :10.1029/2005GL023518.

Larose, E., O. I. Lobkis, and R. L. Weaver (2006a), Passive correlation imaging of a buried scatterer, *The Journal of the Acoustical Society of America*, *119*, 3549–3552, doi :10.1121/1.2200049.

Larose, E., L. Margerin, A. Derode, B. V. Tiggelen, M. Campillo, N. M. Shapiro, A. Paul, L. Stehly, and M. Tanter (2006b), Correlation of random wavefields : an interdisciplinary review, *Geophysics*, *71*(4), SI11–SI21.

Levshin, A., T. B. Yanocskaya, A. V. Lander, B. G. Bukchin, M. P. Barmin, L. I. Ratnikova, and E. N. Its (1989), *Seismic surface waves in a laterally inhomogeneous Earth*, Kluwer Academic Publishers.

Lin, F., M. H. Ritzwoller, J. Townend, M. Savage, and S. Bannister (2007), Ambiant noise Rayleigh wave tomography of New Zealand, *Geophysical Journal International, in press.*

Lobkis, O. I., and R. L. Weaver (2001a), On the emergence of the Green's function in the correlations of a diffuse field, *The Journal of the Acoustical Society of America, 110*, 3011–3017.

Lobkis, O. I., and R. L. Weaver (2001b), On the emergence of the Green's function in the correlations of a diffuse field, *The Journal of the Acoustical Society of America, 110*, 3011–3017.

Longuet-Higgings, M., and R. Stewart (1964), Radiation stresses in water waves ; a physical discussion with applications, *Deep-Sea Research, 11*, 529–562.

Longuet-Higgins, M. (1950), A theory of the origin of microseisms, *Phil. Trans. R. Soc. Lond., 243*, 137–171.

Lévëque, J., L. Rivera, and G. Wittlinger (1993), On the use of the checker-board test to assess the resolution of tomographic inversions, *Geophysical Journal International, 115* (1), 313–318.

Malcolm, A., J. Scales, and B. van Tiggelen (2004), *Physical Review E*, doi : doi :10.1103/PhysRevE.70.015601.

Marchant, R., and G. Stampfli (1996), Subduction of continental crust in the Western Alps, *Tectonophysics, 269*, 217–235.

Margerin, L., M. Campillo, and B. van Tiggelen (1998), Radiative transfer and diffusion of waves in a layered medium : new insight on coda q, *gji, 134*, 596–612.

Margerin, L., M. Campillo, N. Shapiro, and B. van Tiggelen (1999), Residence time of diffuse waves in the crust as a physical interpretation of coda q : application to seismograms recorded in mexico,, *Geophysical Journal International, 138*, 343–352.

Marone, F., M. van der Meijde, S. van der Lee, and D. Giardini (2003), Joint inversion of local, regional and teleseismic data for crustal thickness in the eurasia-africa plate boundary region, *Geophysical Journal International, 154* (2), 499–514, doi :doi : 10.1046/j.1365-246X.2003.01973.x.

Marone, F., S. van der Lee, and D. Giardini (2004), Three-dimensional upper-mantle s-velocity model for the eurasia-africa plate boundary region, *Geophysical Journal International, 158* (1), 109–130.

Mason, W. P., and R. N. Thurston (1988), *Physical Acoustics*, vol. 18, Academic Press.

Nawa, K., N. Suda, Y. Fukao, T. Sato, Y. Aoyama, and K. Shibuya (1998), Incessant excitation of the Earth's free oscillations, *Earth Planets Space*, *50*, 3–8.

Nishida, K. (2002), Origin of earth's ground noise from 2 to 20 mhz, *Geophysical Research Letters*, *29*, 4pp.

Nishida, K., N. Kobayashi, and Y. Fukao (2000), Resonant oscillations between the solid Earth and the atmosphere, *Science*, *287*, 2244–2246.

Nolet, G., and F. Dahlen (2000), *Journal of Geophysical Research*, *105*(19).

Owens, T., H. Crotwell, A. Nyblade, R. Brazier, and C. Langston (1997), Passcal data report 97-005, *IRIS Data Management Center*.

Patane, D., G. Barberi, O. Cocina, P. D. Gori, and C. Chiarabba (2006), Time-resolved seismic tomography detects magma intrusions at Mount Etna, *Science*, *313*, 821–823.

Paul, A., M. Cattaneo, F. Thouvenot, D. Spallarossa, N. Béthoux, and J. Fréchet (2001), A three dimensional crustal velocity model of the south-western alps from local earthquake tomography, *Journal of Geophysical Research*, *106*(19), 367–390.

Paul, A., M. Campillo, L. Margerin, E. Larose, and A. Derode (2005), Empirical synthesis of time-asymmetrical Green functions from the correlation of coda waves, *Journal of Geophysical Research (Solid Earth)*, *110*(b9), 8302–+, doi : 10.1029/2004JB003521.

Pedersen, H., F. Krüger, and the SVEKALAPKO Seismic Tomography Working Group (2006), Influence of the seismic noise characteristics on noise correlations in the Baltic Shield, submitted.

Poupinet, G., W. Ellsworth, and J. Frechet (1984), Monitoring velocity variations in the crust using earthquake doublets : an application to the Calaveras Fault, California, *Journal of Geophysical Research*, *89*, 5719–5731.

Ramm, A. G. (1986), *Scattering by obstacles*, Kluwer Academic Publisher.

Reed, M., and B. Simon (1978), *Methods of modern mathematical physics I, II, III, IV*, Academic Press.

Rhie, J., and B. Romanowicz (2004), Excitation of Earth's continuous free oscillations by atmosphere-ocean-seafloor couplinng, *Nature*, *431*, 552–554.

Rhie, J., and B. Romanowicz (2006), A study of the relation between ocean storms and the earth's hum, *Geochemistry, Geophysics, Geosystems*, *7*(10), doi : doi :10.1029/2006GC001274.

Ritsema, J., L. Rivera, D. Komatitsch, J. Tromp, and H.-J. van Heijst (2002), Effects of crust and mantle heterogeneity on PP/P and SS/S amplitude ratios, *Geophysical Research Letters*, *29*(10), doi :10.1029/2001GL013831.

Ritzwoller, M., and A. L. Levshin (1998), Eurasian surface wave tomography : group velocities, *Journal of Geophysical Research*, *103*(4839-4878), 4839.

Ritzwoller, M., N. Shapiro, M. Barmin, and A. Levshin (2002a), *Journal of Geophysical Research.*

Ritzwoller, M. H., N. M. Shapiro, M. P. Barmin, and A. L. Levshin (2002b), Global surface wave diffraction tomography, *Journal of Geophysical Research*, *107*(B12), 2335, doi :10.1029/2002JB001777.

Roult, G., and W. Crawford (2000), Analysis of 'backgrounds' oscillations and how to improve resolution by subtracting the atmospheric pressure signal, *Phys. Earth Planet. Inter.*, *121*, 325–338.

Roux, P., and W. A. Kuperman (2004), Extracting coherent wavefronts from acoustic ambient noise in the ocean, *The Journal of the Acoustical Society of America*, *116*(4), 1995–2003, doi :10.1121/1.1797754.

Roux, P., K. G. Sabra, P. Gerstoft, and W. A. Kuperman (2005a), P-waves from cross-correlation of seismic noise, *Geophysical Research Letters*, *32*, L19,303, doi : 10.1029/2005GL023803.

Roux, P., K. G. Sabra, W. A. Kuperman, and A. Roux (2005b), Ambient noise cross correlation in free space : theoretical approach, *The Journal of the Acoustical Society of America*, *117*(1), 79–84, doi :10.1121/1.1830673.

Sabra, K., P. Gerstoft, P. Roux, W. A. Kuperman, and M. C. Fehler (2005a), Extracting time-domain Green's function estimates from ambient seismic noise, *Geophysical Research Letters*, *32*, L14,311, doi :10.1029/2005GL023155.

Sabra, K., P. Roux, A. Thode, G. D'Spain, W. Hodgkiss, and W. Kuperman (2005b), Using ocean ambient noise for array self-localization and self-synchronization, *J. of Seismology*, *30*(2), 338–347, doi :10.1109/JOE.2005.850908.

Sabra, K. G., P. Gerstoft, P. Roux, and W. A. Kuperman (2005c), Surface wave tomography from microseisms in southern California, *Geophysical Research Letters*, *32*, L14,311, doi :10.1029/2005GL023155.

Sabra, K. G., P. Roux, and W. A. Kuperman (2005d), Emergence rate of the time-domain Green's function from the ambient noise noise cross-correlation, *The Journal of the Acoustical Society of America*, *118*(6), 3524–3531, doi : 10.1121/1.2109059.

Sabra, K. G., P. Roux, and W. A. Kuperman (2005e), Arrival-time structure of the time-averaged ambient noise cross-correlation function in an oceanic waveguide., *The Journal of the Acoustical Society of America*, *117*(1), 164–174, doi : 10.1121/1.1835507.

Sánchez-Sesma, F. J., and M. Campillo (2006), Retrieval of the Green function from cross correlation : the canonical elastic problem, *Bulletin of the Seismological Society of America in press*, *85*, 269–284.

Sánchez-Sesma, F. J., J. Pérez-Ruiz, M. Campillo, and F. Luzòn (2006a), Elastodynamic 2-D Green function retrieval from cross-correlation : canonical inclusion problem, *Geophysical Research Letters*, *33*, L13,305, doi :10.1029/2006GL026454.

Sánchez-Sesma, F. J., J. Pérez-Ruiz, F. Luzòn, M. Campillo, and A. Rodriguez-Castellano (2006b), Diffuse fields in dynamic elasticity, in press Wave Motion.

Sato, H., and M. C. Fehler (1998), *Seismic wave propagation and scattering in the heterogeneous Earth*, vol. AIP Series in Modern Acoustics and Signal Processing, 308 pp. pp., Springer Verlag, New York.

Schulte-Pelkum, V., P. S. Earle, and F. L. Vernon (2004), Strong directivity of ocean-generated seismic noise, *Geochemistry, Geophysics, Geosystems*, *5*, 3004–+, doi : 10.1029/2003GC000520.

Shapiro, N. M., and M. Campillo (2004), Emergence of broadband Rayleigh waves from correlations of the ambient seismic noise, *Geophysical Research Letters*, *31*, L07,614, doi :10.1029/2004GL019491.

Shapiro, N. M., and S. K. Singh (1999), A systematic error in estimating surface-wave group-velocity dispersion curves and a procedure for its correction, *Bulletin of the Seismological Society of America*, *4*(89), 1138–1142.

Shapiro, N. M., M. Campillo, A. Paul, S. K. Singh, D. Jongmans, and F. J. Sànchez-Sesma (1997), Surface-wave propagation across the Mexican Volcanic Belt and the origin of the long-period seismic-wave amplification in the Valley of Mexico, *Geophysical Journal International*, *128*, 151–166.

Shapiro, N. M., M. Campillo, L. Stehly, and M. H. Ritzwoller (2005), High-resolution surface wave tomography from ambient seismic noise, *Science*, *307*, 1615–1618.

Sherburn, S., R. S. White, and M. Chadwick (2006), Three-dimensional tomographic imaging of the Taranaki volcanoes, New Zealand, *Geophysical Journal International*, *166*, 957–969.

Snieder, R. (2004), Extracting the Green's function from the correlation of coda waves : a derivation based on stationary phase., *Physical Review E*, *69*(4 Pt 2), 046,610.

Snieder, R. (2006), The theory of coda wave interferometry, *Pure and Applied Geophysics*, *163*, 455–473.

Spetzler, J., J. Trampert, and R. Snieder (2002), *Geophysical Journal International*, *149*.

Stehly, L., M. Campillo, and N. Shapiro (2006), A study of the seismic noise from its long range correlation properties, *Journal of Geophysical Research*, *111*, B10,306, doi :10.1029/2005JB004237.

Stehly, L., M. Campillo, and N. M. Shapiro (2007), Travel time measurements from noise correlation : stability and detection of instrumental error, geophysical Journal International, in press.

Suda, N., K. Nawa, and Y. Fukao (1998), Earth's background free oscillations, *Science*, *279*, 2089–2091.

Tanaka, S., et al. (2002), Three-dimensional P-wave velocity structure of Iwate volcano, Japan from active seismic survey, *Geophysical Research Letters*, *29*, 59–62.

Tanimoto, T. (2005), The oceanic excitation hypothesis for the continuous oscillations of the Earth, *Geophysical Journal International*, *160*, 276–288.

Tanimoto, T., and J. Um (1999), Cause of continuous oscillations of the Earth, *Journal of Geophysical Research*, *104*(B12), 723–739.

Tanimoto, T., J. Um, K. Nishida, and N. Kobayashi (1998), Earth's continuous oscillations observed seismically quiet days, *Geophysical Research Letters*, *25*, 1553–1556.

Thouvenot, F., A. Paul, J. Fréchet, N. Béthoux, L. Jenatton, and R. Guiguet (2002), Are there superposed mohos in the south-western alps ? new seismic data from fan-profiling reflections, *gji in press*.

Thurber, C., S. Roecker, H. Zhang, S. Baher, W. Ellsworth, and T. Tanimoto (2004), Fine-scale structure of the San Andreas Fault Zone and location of the SAFOD target earthquakes (2004), *Geophysical Research Letters*, *31*, L12S02.

Trampert, J., and J. Woodhouse (1995), Global phase velocity maps of love and rayleigh waves between 40 and 150 seconds., *Geophysical Journal International*, *122*, 675–690.

van Tiggelen, B. A. (2003), Green function retrieval and time reversal in a disordered world., *Physical Review Letter*, *91*(24), 243,904.

van Tiggelen, B. A. (2003), Green function retrieval and time reversal in a disordered world, *Physical Review Letter*, *91*(24), 243,904, doi : 10.1103/PhysRevLett.91.243904.

Waldhauser, F., E. Kissling, J. Ansorge, and S. Mueller (1998), Three-dimensional interface modelling with two-dimensional seismic data : the Alpine crust mantle boundary, *Geophysical Journal International*, *135*, 264–278.

Waldhauser, F., R. Lippitsch, E. Kissling, and J. Ansorge (2002), High-resolution teleseismic tomography of upper-mantle structure using an a priori three-dimensional crustal model, *Geophysical Journal International*, *150*, 403–414.

Wapenaar, K. (2004), Retrieving the elastodynamic Green's Function of an arbitrary inhomogeneous medium by cross-correlation, *Physical Review Letter*, *93*, 254,301.

Wapenaar, K. (2006), Nonreciprocal Green's function retrieval by cross correlation, *The Journal of the Acoustical Society of America*, *120*(1), EL7–E13, doi : 10.1121/1.2208153.

Wapenaar, K., E. Slob, and R. Snieder (2006), Unified Green's function retrieval by cross correlation, *Physical Review Letter*, *97*(23), 234,301, doi : 10.1103/PhysRevLett.97.234301.

Watada, S., A. Kobayashi, and E. Fujita (2001), Seasonal variations of atmospheric and ocean-bottom pressure data in millihertz band in "OHP/ION Joint Symposium 'Long-Term Observations in the Oceans'", *Earthquake Research Institute, University of Tokyo*, pp. 35–37.

Weaver, R. L. (2005), Information from seismic noise, *Science*, *307*(5715), 1568–1569, doi :10.1126/science.1109834.

Weaver, R. L., and O. I. Lobkis (2001), Ultrasonics without a source : thermal fluctuation correlations at MHz frequencies., *Physical Review Letter*, *87*(13), 134,301.

Weaver, R. L., and O. I. Lobkis (2003), Elastic wave thermal fluctuations, ultrasonic waveforms by correlation of thermal phonons, *The Journal of the Acoustical Society of America*, *113*, 2611–2621, doi :10.1121/1.1564017.

Weaver, R. L., and O. I. Lobkis (2004), Diffuse fields in open systems and the emergence of the Green's function, *The Journal of the Acoustical Society of America*, *116*(5), 2731–2734, doi :10.1121/1.1810232.

Weaver, R. L., and O. I. Lobkis (2005a), Fluctuations in diffuse field-field correlations and the emergence of the Green's function in open systems, *The Journal of the Acoustical Society of America*, *117*, 3432–3439, doi :10.1121/1.1898683.

Weaver, R. L., and O. I. Lobkis (2005b), The mean and variance of diffuse field correlations in finite bodies, *The Journal of the Acoustical Society of America*, *118*, 3447–3456, doi :10.1121/1.2109307.

Weaver, R. L., and O. I. Lobkis (2006), Diffuse fields in ultrasonics and seismology, *Geophysics*, *71*, SI5–SI9.

Webb, S., X. Zhang, and W. Crawford (1991), Infragravity waves in the deep ocean, *Journal of Geophysical Research*, *96*, 2723–2736.

Wegler, U., and C. Sens-Schonfelder (2007), Fault zone monitoring with passive image interferometry, *Geophysical Journal International*, *168*(3), 1029–1033.

Wilson, A., G. Garven, and J. Boles (1999), *GSA Bulletin*, *111*.

Yang, Y., M. H. Ritzwoller, A. L. Levshin, and N. M. Shapiro (2007), Ambient noise Rayleigh wave tomography across Europe, *Geophysical Journal International*, *168*, 259–274, doi :10.1111/j.1365-246X.2006.03203.x.

Yao, H., R. D. van der Hilst, and M. V. de Hoop (2006), Surface-wave array tomography in SE Tibet from ambiant seismic noise and two-station analysis – I. Phase velocity maps, *Geophysical Journal International*, *166*, 732–744, doi :10.1111/j.1365-246X.2006.03028.x.

Zollo, A., L. D'Auria, R. D. Matteis, A. Herrero, J. Virieux, and P. Gasparini (2002), Bayesian estimation of 2-D P-velocity models from active seismic arrival time data : imaging of the shallow structure of Mt Vesuvius, *Geophysical Journal International*, *151*, 566–582.